

Development of Optics Measurement Methods for Circular Accelerators

Dissertation

zur Erlangung des Doktorgrads

an der Fakultät für Mathematik, Informatik und Naturwissenschaften

Fachbereich Physik

der Universität Hamburg

vorgelegt von
Andreas Wegscheider

Hamburg
2022

Gutachter der Dissertation:	Prof. Dr Wolfgang Hillert Dr Andrea Franchi
Mitglieder der Prüfungskommission:	Prof. Dr Wolfgang Hillert Dr Andrea Franchi Prof. Dr Daniela Pfannkuche Dr Frank Zimmermann Prof. Dr Giuliano Franchetti
Vorsitzender der Prüfungskommission:	Prof. Dr Daniela Pfannkuche
Datum der Disputation:	01.07.2022
Vorsitzender Fach-Promotionsausschuss PHYSIK:	Prof. Dr Wolfgang J. Parak
Leiter des Fachbereichs PHYSIK:	Prof. Dr Günter H. W. Sigl
Dekan der Fakultät MIN:	Prof. Dr Heinrich Graener

Persistent Identifier: [urn:nbn:de:gbv:18-ediss-105570](https://nbn-resolving.org/urn:nbn:de:gbv:18-ediss-105570)

Dieses Dokument wurde mit LuaLaTeX und dem KOMA-Script gesetzt.
Hauptschriftart: STIX Two

ABSTRACT

Linear optics corrections in circular particle accelerators have achieved remarkable performance in the last years pushing the precision and accuracy of the measurement and correction of machine parameters further. But development of accelerator technology is not resting either and the introduction of next generation light sources and the design and construction of new colliders and future projects constantly demand more advanced and precise measurement methods.

This work presents the development and enhancement of three distinct optics measurement methods. The first one is a more precise, more accurate and faster measurement method of the β function, an optics parameter that presents a direct observable for the focusing at any given point in the machine. Constraints on the tolerances of focusing errors are given for machine performance and protection reasons. This work builds on an improvement presented in a previous work and further increases precision, accuracy and speed. The second method is a novel local observable for linear lattice imperfections, which can be used to detect strong error sources in the machine, guiding dedicated corrections and being independent of the optics configuration. The last method provides a new way to describe the impact of forced particle motion on the measurement of transverse coupling.

The developments in the domain of linear optics measurements presented in this thesis already positively impact LHC operation and machine development and are part of the preparation for future operation of the LHC and other accelerators.

ZUSAMMENFASSUNG

Im Gebiet der Korrektur linearer Optik in Ringbeschleunigern wurde in den letzten Jahren beachtenswerter Fortschritt gemacht. Die Genauigkeit und Richtigkeit der Messung und Korrektur von Maschinenparametern wurde immer weiter verbessert. Die Entwicklung von Beschleunigertechnologie hält jedoch nicht still und die Einführung von Lichtquellen der nächsten Generation und Design und Bau von neuartigen Beschleunigern und Zukunftsprojekten erfordern neue, fortschrittliche Messmethoden.

Diese Arbeit stellt die Weiterentwicklung und Verbesserung von drei unterschiedlichen Optikkessmethoden vor. Die erste Methode ist eine genauere und schnellere Messung der β -Funktion, einem Optikparameter, der eine direkte Messgröße für die Fokussiereigenschaften an einem beliebigen Punkt im Beschleuniger darstellt. Aus Gründen des Schutzes und der Leistungsfähigkeit der Maschine sind gewisse Anforderungen an die Fokussierung gegeben. Die hier vorgestellte Messmethode baut auf einer vorangehenden Verbesserung der klassischen Methode zur Messung der β -Funktion auf und liefert eine bessere Genauigkeit und kürzere Berechnungszeiten. Die zweite Methode ist eine neue lokale Observable für lineare Maschinenfehler, die dazu benutzt werden kann, starke Fehlerquellen zu erkennen, wodurch eine dedizierte Korrektur gezielt durchgeführt werden kann. Außerdem ist sie unabhängig von der genauen Maschinenkonfiguration, wodurch die Notwendigkeit der Messung jeder einzelnen Zwischenkonfiguration entfällt. Die letzte Methode bietet eine neue Beschreibung des Effekts der getriebenen Schwingung der Teilchen auf die Messung der linearen transversalen Kopplung.

Die Weiterentwicklungen im Bereich der linearen Strahloptikmessung, die in dieser Arbeit vorgestellt werden, erleichtern bereits den Betrieb des LHC und Maschinenentwicklungsstudien und sind Teil der Vorbereitungen für den zukünftigen Betrieb des LHCs und anderer Beschleuniger.

Eidesstattliche Versicherung / Declaration on oath

Hiermit versichere ich an Eides statt, die vorliegende Dissertationsschrift selbst verfasst und keine anderen als die angegebenen Hilfsmittel und Quellen benutzt zu haben.

Die eingereichte schriftliche Fassung entspricht der auf dem elektronischen Speichermedium.

Die Dissertation wurde in der vorgelegten oder einer ähnlichen Form nicht schon einmal in einem früheren Promotionsverfahren angenommen oder als ungenügend beurteilt.

Genf, den 02.03.2022

Unterschrift des Doktoranden

Acknowledgments

It is not possible to arrive at this stage – finishing a PhD project – without the help and influence of a considerable amount of people and chances are high that I will have forgotten to mention some of them. This section will present my gratitude towards all the countless people who have been important to me on my way to where I am now in a perceived chronological order.

Firstly I have to thank my fellow undergraduate students, especially *Peter Freiwang*, *Daniel Reiser* and *Alexis Kassiteridis* for treading the path with me and for showing me what is important – albeit by giving a negative example in one particular case. Another person who must be mentioned is Prof. Dr *Harald Lesch* who not only awoke my interest in physics when I was young but also turned out to be an inspiring professor, not only of Astrophysics but especially in Philosophy.

Special thanks for arousing my interest in accelerator physics go to Prof. *Lenny Rivkin* and *Adrian Oeftiger*.

I would like to acknowledge the assistance I received from the following people: My supervisors Prof. Dr *Wolfgang Hillert* and Dr *Rogelio Tomás* for their knowledge, mentoring and guidance and for never discarding far fetched ideas, my colleagues *Ewen Maclean* and *Tobias Persson* for many fruitful discussions and answering countless questions, and to *Andrea Franchi* for showing me the path into the realm of RDTs and the normal form approach. Additional thanks go to Prof. Dr *Bernard Parisse* for acting as counterweight against the many premature ideas that I and my colleagues have and for grounding my opinions on our research methods.

I want to thank my colleagues and friends here at CERN for the memorable time, both in the office and in our free time, be it in person or virtual: *Marco D’Andrea*, *Sondre Vik Furuset*, *Alexander Krainer*, *Elena Fol*, *Joschua Dilly*, *Felix Carlier*, *Leon van Riesen-Haupt* and *Felix Soubelet*.

Some deserve a special mention:

Michael Hofer for being at the same time an invaluable helpful and incredibly annoying office mate, for his view of the bigger picture, his bad jokes and the tea and cookie times. *Jaime Coello de Portugal* (and I skip the rest of his name) for an enthusiastic introduction to programming, our discussions about computer games and for pulling me into some fun hobby projects like soldering my own keyboard.

And *Marian Lückhof* for the many, many discussions and for preferring early lunch.

And last but not least I want to express my deep gratitude towards my family: My parents, *Martin* and *Sigrid* who raised me to become the person I am now, for believing in me and supporting me. And of course to *Lorène* for being in my life, the adventures we share and for supporting me during these long years of the PhD project.

This work is sponsored by the Wolfgang Gentner Program of the German Federal Ministry of Education and Research (05E15CHA).

CONTENTS

1	Introduction	1
1.1	Objectives of this work	2
1.2	The Large Hadron Collider	3
1.3	Optics measurements and corrections	5
1.3.1	Measurement tools and techniques	5
1.4	Outline of the thesis	7
2	Theoretical Foundations	9
2.1	Beam Optics	9
2.1.1	Linear Beam Dynamics	9
2.1.2	Courant-Snyder coordinates	14
2.2	Hamiltonian description and Lie maps	16
2.3	The normal form approach	18
2.4	Resonance driving terms	21
2.4.1	Influence of linear lattice imperfections on betatron phases	22
2.4.2	Coupling RDTs	25
2.5	Calculation of optics functions	26
2.5.1	β function measurement	26
2.5.2	Coupling measurement	27
2.6	Forced motion	31
2.6.1	Linear motion with AC dipole	31
2.6.2	Compensation of linear parameters	35
3	The Analytical N-BPM method	39
3.1	β function measurement from turn-by-turn data	39
3.1.1	Three BPM method	39

3.1.2	Original N-BPM method	40
3.2	Generalised least squares	41
3.2.1	Error Propagation	42
3.2.2	The generalised least-squares estimator	44
3.2.3	Error matrix for N-BPM method	45
3.2.4	Extension of the N-BPM method	46
3.3	Corrected β from phase formula	46
3.3.1	Effect of transverse sextupole misalignments	48
3.3.2	Effect of longitudinal quadrupole misalignments	48
3.3.3	Effect of BPM misalignments	49
3.3.4	Derivation of a corrected β from phase formula	49
3.4	Calculation of the correlation matrix	51
3.5	Removal of bad BPM combinations	51
3.6	HL-LHC	55
3.7	Conclusion	56
4	A local observable for linear lattice imperfections	57
4.1	Introduction	57
4.2	Local observable	59
4.2.1	The general case – phase advances different from $n\pi$	60
4.2.2	Exact multiples of π	63
4.2.3	Exploring the second order	64
4.3	Simulating Errors and Noise	65
4.3.1	General simulation setup	65
4.3.2	LHC with known field errors	67
4.3.3	Phase noise	67
4.3.4	Single strong error source	69
4.3.5	Feed-down from sextupoles	69
4.4	Experimental verification	72
4.5	Conclusion and Outlook	72
5	Forced Coupling Resonance Driving Terms	77
5.1	Driven coupled motion	77
5.1.1	AC-dipole as skew quadrupole	78
5.1.2	Derivation of the coupled driven motion	79
5.1.3	Rescaling and Formula methods	84
5.2	Comparison of the methods for typical LHC machine configurations	85
5.2.1	HL-LHC and stronger coupling	87
5.3	Conclusion	87

6 Conclusion and Outlook

CHAPTER 1

INTRODUCTION

The goal of this PhD project is the development of linear optics measurement methods for circular accelerators. The term *optics* is used because the manipulation of a charged particle beam in an accelerator shares many characteristics with the bending and focusing of light through lenses and other optical devices and *linear* refers to lattice elements with linear magnetic field.

Linear optics corrections have achieved remarkable performance in the last years [1, 2, 3, 4, 5, 6, 7], pushing the precision and accuracy of machine parameters further. But development of accelerator technology is not resting either and the introduction of next generation light sources and the design and construction of new colliders and future projects constantly demand more advanced and precise measurement methods.

Data acquisition and processing, as well as the final analysis and correction procedures, is performed on electronic devices and computers. Therefore the term *method* used in this work to describe a measurement or correction procedure, usually encompasses also the implementation of a dedicated computer algorithm.

For the largest machines – containing thousands of lattice elements – many classical measurement and correction methods suffer from long execution times as the computational complexity of the measurement and correction algorithms grows with the number of parameters, often exponentially. Therefore, the speed of the used techniques is also getting more and more crucial for a smooth operation. Moreover, often the full potential of the analysis can only be harvested *offline* in the days and weeks following the actual measurement.

1.1 Objectives of this work

In this work three distinct optics measurement methods are treated. All of these methods take as input the Fourier analysis of turn-by-turn data of the beam centroid position, picked up at certain measurement devices called *Beam Position Monitors* (BPMs). In order to get a sufficiently strong signal, the particle beam is excited. If the excitation method induces a forced oscillation, optics functions are changed and this effect has to be compensated. The remainder of this chapter introduces the data acquisition and its surrounding devices, as well as CERN and its accelerator facilities.

The first method is a more precise and faster measurement of the β function, an optics parameter that presents a direct observable for the focusing at any given point in the machine. Constraints on the tolerances of focusing errors are given for machine performance and protection reasons. An improvement of the classical β function measurement was presented in a previous work. This thesis builds upon this improvement and enhances it in terms of speed and precision.

The second method is a new local observable for linear lattice imperfections. In the LHC precise optics correction methods consider a local region of the accelerator as transfer line. Measured optics functions at the start of the segment are used as initial condition for a simulation using the best knowledge model of the accelerator. Then a fitting on the magnetic field strengths is used to match the expected optics to the measured one. Currently this correction method is used at certain important points in the accelerator where particularly strict tolerances on errors are given or errors have a high impact on the optics. Local observables facilitate detecting strong local sources and permit to apply dedicated correction steps. This work introduces for the first time a local observable for linear lattice errors.

The third topic is the revision and further development of existing methods to describe the impact of forced particle motion on the measurement of transverse coupling. Certain lattice elements interlink vertical and horizontal particle motion, an effect called transverse coupling which has negative impact on the beam stability in the LHC. The driving device, used to create the signal for turn-by-turn measurements influences the measurements of certain quantities, including coupling, and this influence has to be compensated. The current methods neglect a small local effect of this, which became apparent recently. A new description of the modeling of the driven motion is presented in a previous work and this thesis applies this description to the measurement of transverse coupling, showing the local effect for the first time in theoretical considerations.

1.2 The Large Hadron Collider

The present work has been carried out mainly at the *European Organization for Nuclear Research* (CERN) during commissioning and machine development studies of the *Large Hadron Collider* (LHC). Therefore, this introduction would not be complete without a brief presentation of the used facilities.

The LHC is the world's largest particle accelerator with a circumference of 27 km. It is situated at the french-swiss border near Geneva as part of CERN. The initial purpose of the LHC was to discover the Higgs Boson and to study rare high energy events with a centre of mass energy up to 14 GeV.

The number of collision events is proportional to the *luminosity*

$$\mathcal{L} = \frac{N^2 n_b f}{4\pi\sigma_x\sigma_y} \quad (1.1)$$

where N is the number of particles per bunch, n_b the number of bunches, f is the revolution frequency and σ_z is the beam size in direction z .

Equation (1.1) assumes that the bunches collide head-on and no deteriorating effects are present. A more realistic form of the luminosity is [8]

$$\mathcal{L} = \frac{N^2 n_b f}{4\pi\sigma_x\sigma_y} F \quad (1.2)$$

where F is a reduction factor, depending on the exact conditions of the beam and the interaction region such as crossing angle, offset of the beams w.r.t. each other or the optical axis, hourglass effect, non-Gaussian beam profiles etc. In the LHC, F is expected to be around 0.8.

The discovery of the Higgs Boson was officially confirmed in 2012 [9, 10] and since then the purpose of the LHC lies in providing luminosity for more precise measurements of Higgs channels and other high energy particle events.

Particles that enter the LHC are accelerated in several pre-accelerators, forming the so called *injector chain*[11] which is illustrated in Fig. 1.1. Protons start their journey as H^- ions in LINAC2 (LINAC4 in the future) where they are accelerated to 50 MeV. They are further accelerated in the PS Booster to 1.4 GeV, in the Proton Synchrotron (PS) to 25 GeV and finally to 450 GeV in the Super Proton Synchrotron before they are injected into the LHC. Heavy ions start in the LINAC3 and are then accelerated in the Low Energy Ion Ring (LEIR) before they are injected into the PS from where they continue as described for protons.

The LHC consists of eight identical arcs for bending of the beams and eight straight sec-

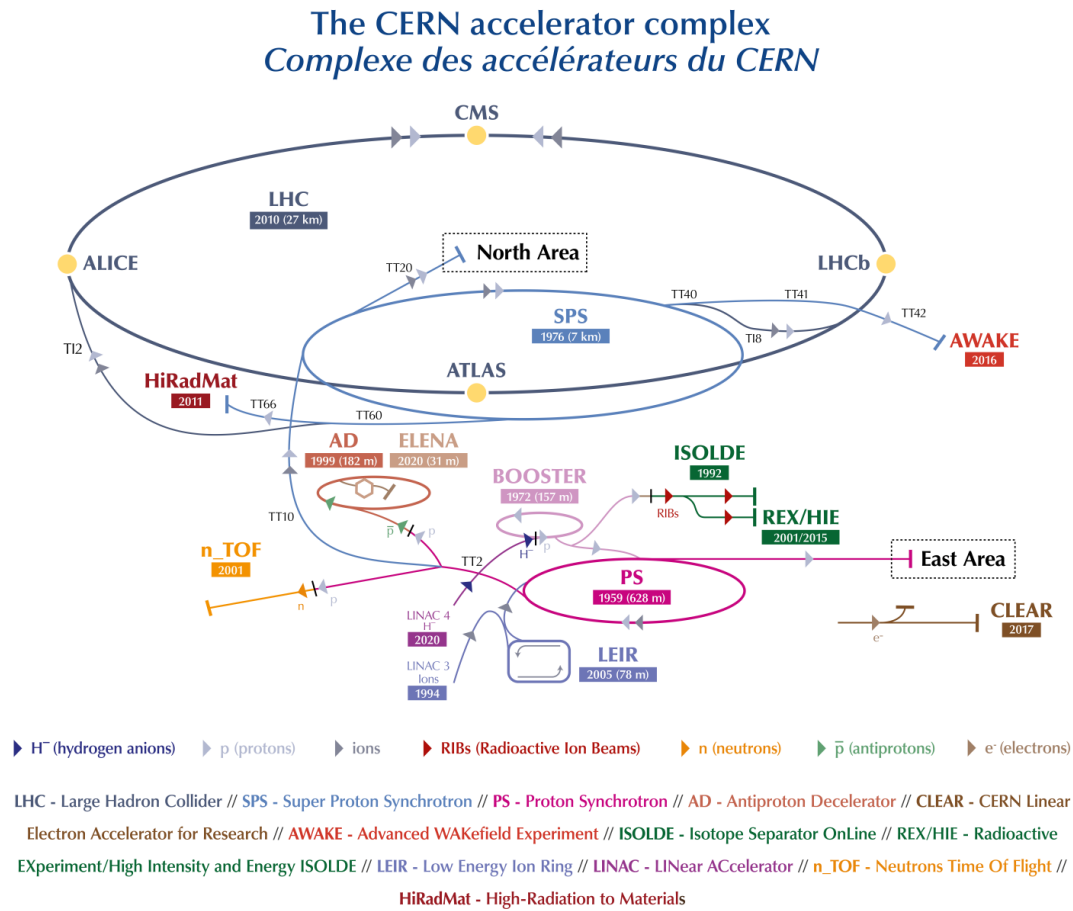


Figure 1.1: CERN has various accelerators and decelerators. H^- ions are pre-accelerated in LINAC2 (LINAC4 in the future) and passed to PSBooster, PS, SPS and finally injected into the LHC. Image credit: [12]

tions between the arcs which contain the experiments, injection and extraction region and accelerating structures.

An arc consists of 23 so called *FODO* cells containing two bending sections interleaved with a focusing and a defocusing quadrupole¹. To correct for magnet imperfections, corrector magnets are also installed in the cell. Figure 1.2 shows a schematic of an LHC FODO cell. During long shutdown 2, from 2019 until 2021, the CERN accelerator complex undergoes

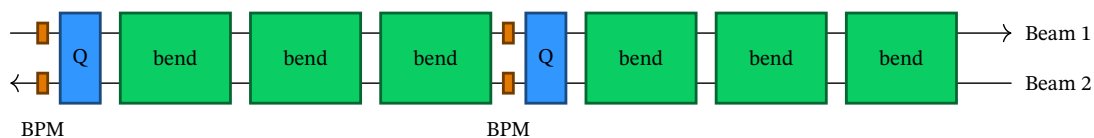


Figure 1.2: Schematic of an LHC FODO cell. Two bending sections, consisting of 3 bending dipoles each are interleaved by one focusing and one defocusing quadrupole, respectively.

¹The acronym FBDB for focusing-bending-defocusing-bending would be more precise but this work will follow the common denomination.

an extensive upgrade process preparing it already partly for the high luminosity upgrade of LHC. In addition, the injector chain is upgraded in a separate project called *LHC Injector Upgrade* (LIU) [13, 14].

1.3 Optics measurements and corrections

There are two areas for which the continued measurement and correction of optics parameters is of importance. The first is machine protection. If the nominal LHC beam hits the wall of the beam pipe it can deal severe damage to the elements ranging from heating up superconducting elements and inducing a magnet quench to physically destroying machine parts by melting (or even evaporating) the material.

The second area for which optics control is highly important is the machine performance. The delivered luminosity can be reduced by optics errors. The two main LHC experiments, ATLAS and CMS demand a luminosity imbalance below 5%. To achieve this an optics correction up to the percent level is needed. High quality optics also improve operational efficiency.

1.3.1 Measurement tools and techniques

The most important technique for beam based optics measurements that is applied in the LHC is the excitation of the particle beam. If the bunch is excited it performs a betatron oscillation about the closed orbit with a measurable amplitude. The position of the beam is recorded at certain positions in the accelerator at each revolution. The obtained turn-by-turn data is then analysed as described later.

To obtain said excitation there are two methods that will be introduced in this section: a free kick which provokes a free oscillation of the bunch and an AC-dipole which drives a forced oscillation of the beam.

Free Kick

If the beam experiences a kick it will perform a damped free oscillation. The particle's position at the same location turn after turn is illustrated in Fig. 1.3. Light particles like electrons suffer from a strong damping because of their high synchrotron radiation but heavier particles like the protons accelerated in the LHC are damped much slower. Nevertheless the oscillation amplitude decreases fast and not many turns are available for high precision measurements of the turn-by-turn signal. In order to still have as much signal as possible the kick strength has to be as high as feasible without kicking the beam strongly enough

to damage elements or even kick it out of the accelerator.

Furthermore the excitation by a single kick carries the risk of filamenting the phase space and blowing up the beam emittance.

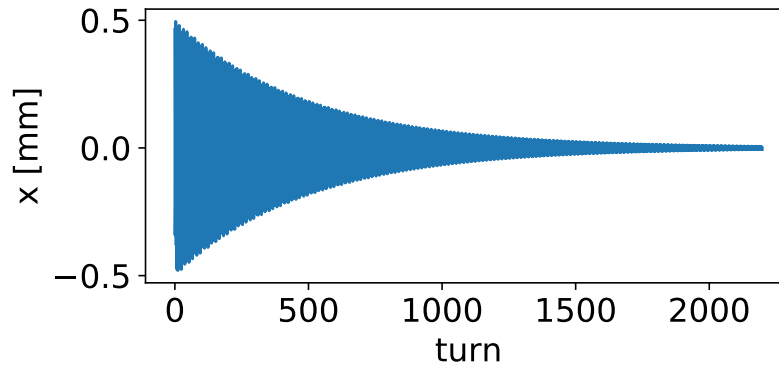


Figure 1.3: The particle's turn-by-turn position for an excitation by a single kick.

AC-dipole

The other method to excite the beam that is used in LHC is a dipole connected to an alternating current power amplifier. This creates a driven oscillation of the beam [15] which can be measured in BPMs [16, 17]. The excitation amplitude is slowly ramped up for 2000 turns in order to stay in an adiabatic regime [18] held constant for 6600 turns and then again adiabatically ramped down. The particle's turn-by-turn position is illustrated in Fig. 1.4.

The adiabatic ramp up and down prevent a blow up of the beam emittance and since the oscillation amplitude can be held constant, a smaller maximum amplitude is needed. Since the driven excitation creates a forced oscillation as opposed to a free one as in the case of a single kick, the turn-by-turn motion of the particle does not reflect the pure betatron oscillation and this effect has to be compensated. For this compensation a good theoretical knowledge of the driven motion is needed.

Beam Position Monitors

To record the turn-by-turn position of the beam, the LHC possesses more than 500 dual-plane Beam Position Monitors (BPMs) [19] which are installed approximately regularly around the ring.

As the beam passes through the monitor, it induces an electric signal which is then processed to calculate the beam position.

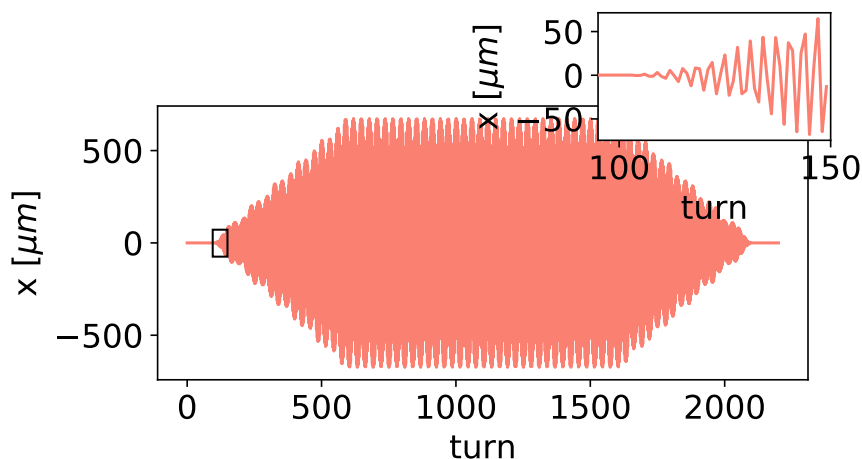


Figure 1.4: The turn-by-turn position of an AC-dipole excitation. The driving force is ramped up, held at flat-top and ramped down again. The small plot shows a magnified view of the start of the ramp up.

The BPM resolution in the LHC is approximately 0.1 mm [20, 21] with a pilot bunch of 10^{10} protons, that we use to measure the optics.

1.4 Outline of the thesis

Chapter 2 gives an introduction of the necessary theory. Starting with linear beam dynamics it introduces the most important terminology before passing to the more mathematically involved regime of normalised coordinates, adding up to the introduction of resonance driving terms which are used to study beam optics throughout this work. This formalism is then used to express the quantities needed in later chapters in a useful form. Finally, the actual methods used to measure some machine parameters are described in detail giving the reader an insight into where the newly developed methods will act. No new discovery is presented in this chapter and it is a mere summary of the theoretical foundations. Only subsection 2.6.1 bears a minor amount of original work re-deriving the final form of the forced coordinates in the used formalism, generalising it to an arbitrary position in the ring.

Chapter 3 presents the improved β function measurement. Previous methods are presented as well as theoretical foundations of generalised least squares minimisation. Original studies are presented in the form of a derivation of the analytical error propagation as well as simulation studies to assess the speed, accuracy and precision of the new method and experimental measurements carried out at the LHC.

In chapter 4 a new local observable is derived, use cases and limitations are worked out

and simulations as well as experimental verification are presented. This chapter consists in its entirety of original work.

The final topic is presented in chapter 5. The original work consists of the derivation of forced coupling resonance driving terms and the comparing studies. For completeness, methods currently used to model the effect of driven oscillation on the coupling terms are reviewed. This revision does not represent original work.

Since this thesis treats very distinct topics, each chapter begins with a brief descriptive block to guide the reader into the respective topic. A brief summary of the chapter's structure is given as well as an outline of the original work presented in the chapter.

Finally, chapter 6 represents a conclusion of the thesis, summarising the treated topics and highlighting their merit as well as an outlook of further development possibilities.

CHAPTER 2

THEORETICAL FOUNDATIONS

This chapter presents the basic theoretical foundations needed to develop the methods and algorithms presented in the main part of this thesis. Therefore we need a sound understanding of linear beam optics, optics parameters like β function and phase and, finally, linear transverse coupling. Only a brief summary of the vast field of accelerator physics can be given in the scope of this thesis. The interested reader may consult some of the great introductory works of the field, e.g. [22, 23, 24].

Also the normal form approach shall be introduced here as it is needed to calculate optics parameters from Hamiltonian terms later on. Since this is a mathematically heavy subject, the author tried to find the optimum between brevity and rigor.

No new discoveries are presented in this chapter. It is a mere summary of the necessary theory.

2.1 Beam Optics

Very much like light beams, charged particle beams in an accelerator can be bent¹, focused, defocused and can be subject to effects like dispersion and chromaticity. Therefore the term *optics* is generally used to describe the movement and behaviour of particle beams around the accelerator.

This work focuses on single particle dynamics, effects between the particles of a beam will be neglected.

2.1.1 Linear Beam Dynamics

Linear beam dynamics studies the effect of linear electromagnetic fields on the particles. This includes primarily only drift spaces, bending magnets and (de)focusing magnets. Under the presence of electromagnetic fields \vec{E} and \vec{B} , the Lorentz force acts on the particles

¹the *bending* of light is, of course, technically difficult to achieve

with charge q and velocity \vec{v} .

$$\vec{F} = q(\vec{E} + \vec{v} \times \vec{B}) \quad . \quad (2.1)$$

A dipole with a constant magnetic field B_y bends a particle's trajectory into an arc of radius ρ

$$\rho = \frac{p}{qB_y} \quad . \quad (2.2)$$

It is useful to describe the motion in a circular accelerator in a co-moving reference frame as depicted in Fig. 2.1 where the cartesian coordinates $\{x', y', z'\}$ are transformed into a system $\{x, y, s\}$ with the properties:

$$\begin{aligned} \Delta s &\parallel \text{reference orbit} \\ \hat{y} &= \hat{y}' \\ \hat{x} &= \hat{y} \times \Delta s \end{aligned} \quad (2.3)$$

and a longitudinal coordinate s along the reference orbit. The optical axis of the elements

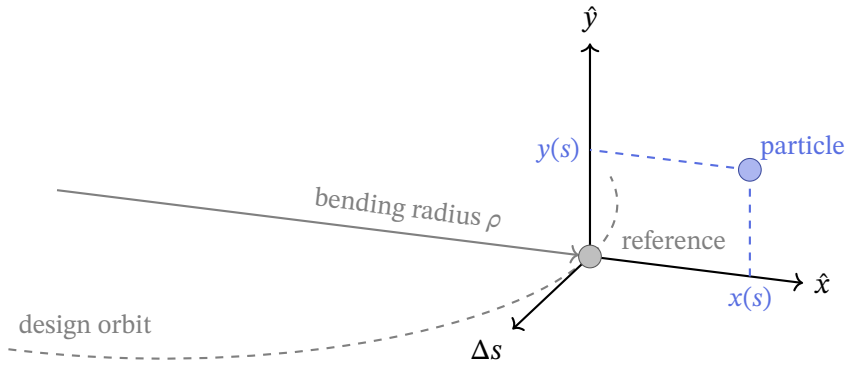


Figure 2.1: The Frenet-Serret coordinate system which is moving along the design orbit of particles in the accelerator.

is usually used as reference orbit. If there is no transverse offset of the elements, this coincides with the closed orbit.

In this coordinate system the motion of a particle in a circular accelerator is described by Hill's differential equation:

$$\frac{d^2 z}{ds^2} + k(s)z = 0 \quad (2.4)$$

where $z \in \{x, y\}$ is the transverse coordinate and $k(s)$ is the linear magnet strength at position s .

A solution that satisfies Eq. (2.4) in two dimensions is

$$z(s) = A_z(s) \cos(\varphi_z(s) + \varphi_{z,0}) \quad (2.5)$$

where the s -dependent amplitude of the oscillation can be split:

$$A_z(s) = \sqrt{2J_z\beta_z(s)} \quad . \quad (2.6)$$

$\beta_z(s)$ is the s -dependent part of the amplitude, called β function. J_z is the action invariant of the particle's motion. $\beta(s)$ is periodic with the circumference of the ring C .

Of special interest for a collider is the value of the β function at the interaction point, because it defines the beam size and has a high impact on the luminosity, as follows from Eq. (1.1). At the LHC, the β function at the interaction point is denoted as $\beta^* \equiv \beta(s_{\text{IP}})$ whereas the *smallest* β function is called β_{waist} .

$\varphi(s)$ is called the *betatron phase* and satisfies the following property:

$$\varphi(s_1) - \varphi(s_0) = \int_{s_0}^{s_1} \frac{1}{\beta(s)} ds \quad . \quad (2.7)$$

The trajectories of particles with an action J are limited by an envelope function $\sqrt{2J\beta}$ as illustrated in Fig. 2.2. Actual β functions are shown in Fig. 2.3.

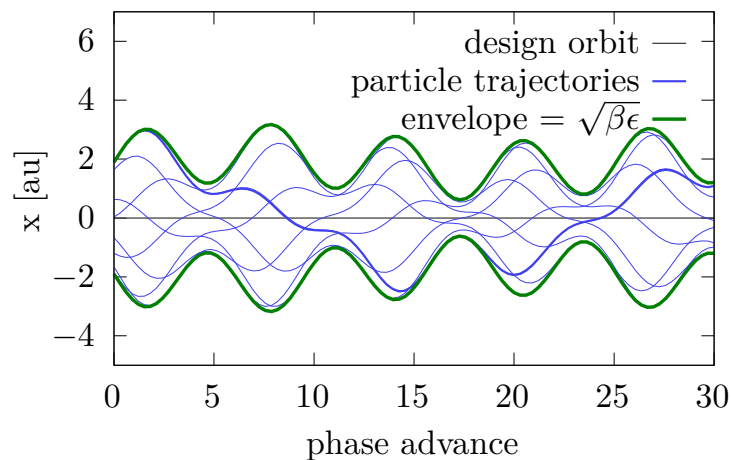


Figure 2.2: The trajectories of particles with action J are shown.

Solutions of Eq. (2.4) can be expressed in matrix form

$$\begin{pmatrix} z \\ p_z \end{pmatrix}_b = \begin{pmatrix} m_{11} & m_{12} \\ m_{21} & m_{22} \end{pmatrix} \begin{pmatrix} z \\ p_z \end{pmatrix}_a \quad . \quad (2.8)$$

Throughout this work, the following definition of momentum is used:

$$p_z \equiv \frac{dz}{ds} \quad . \quad (2.9)$$

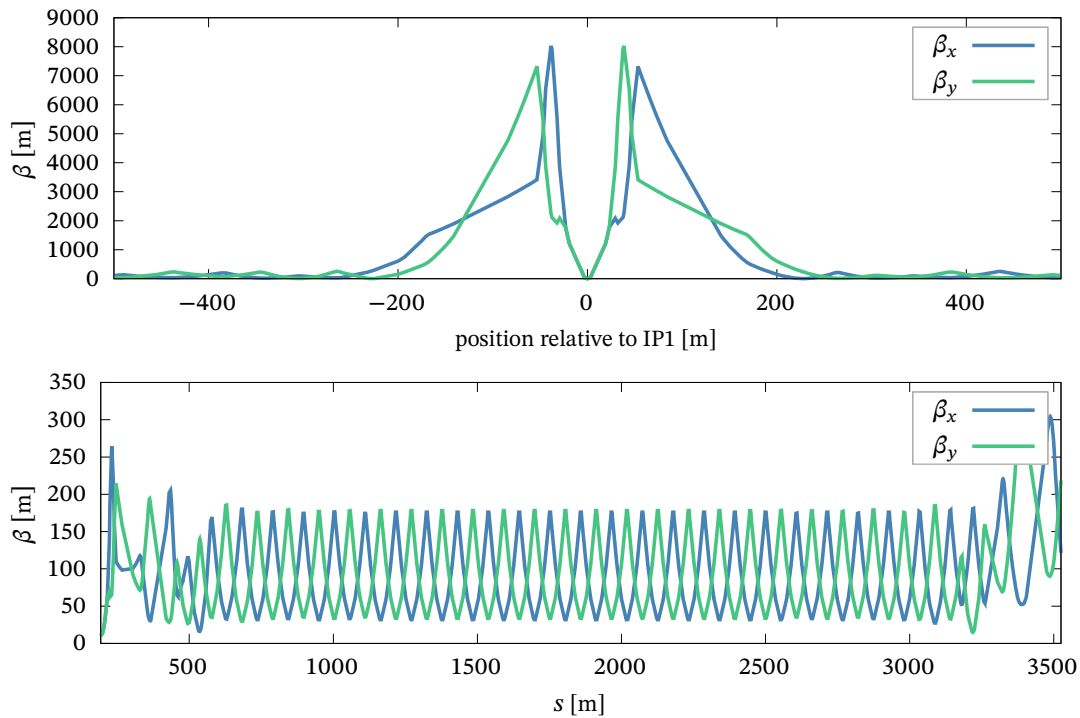


Figure 2.3: TOP: The β function around IP1. BOTTOM: The β functions in an LHC arc, the plot ranges from IR2 to IR3, avoiding high β regions (IR1 and IR5) shown in the top plot. Both plots show the LHC collision optics at $\beta^* = 30$ cm.

The reference frame spanned by z , p_z is called *phase space*².

The matrix

$$\mathbf{M} = \begin{pmatrix} m_{11} & m_{12} \\ m_{21} & m_{22} \end{pmatrix} \quad (2.10)$$

is called the *transfer matrix*. It describes the transformation of phase space when going from one position s_a in the lattice to another s_b .

At this point in an introductory text of, e.g. a thesis or a textbook on accelerator physics it is customary to give a simple example, a basic linear lattice element like a drift space or a quadrupole for illustration. The author chooses to present a quadrupole magnet, since the effect of quadrupolar imperfections is dealt with in later chapters. This example is revisited in the more complex frameworks of Hamiltonian mechanics and Lie maps to guide the reader.

For s inside the quadrupole $k(s) = k_1$. The solution of Hill's equation is

$$z(s) = \cos \left[\sqrt{k}(s - s_0) \right] z_0 + \frac{1}{\sqrt{k}} \sin \left[\sqrt{k}(s - s_0) \right] p_{z,0} \quad (2.11)$$

²Sometimes the name phase space is reserved for the reference frame spanned by $\left(z, \frac{dz}{dt} \right)$ whereas the one spanned by $\left(z, \frac{dz}{ds} \right)$ is called *trace space*. This work will, however, follow the convention stated in the main text.

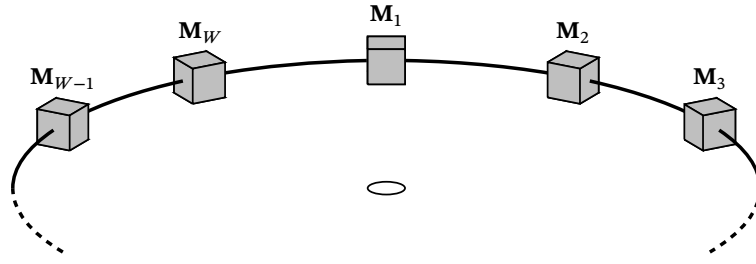


Figure 2.4: This schematic represents the accelerator lattice, consisting of consecutive maps $\mathbf{M}_1 \dots \mathbf{M}_W$.

The transfer matrix of a focusing quadrupole reads

$$\mathbf{M}_{QF} = \begin{pmatrix} \cos \sqrt{K} & \frac{1}{\sqrt{k}} \sin \sqrt{K} \\ -\sqrt{K} \sin \sqrt{K} & \cos \sqrt{K} \end{pmatrix} \quad (2.12)$$

where K is the integrated magnet strength

$$\sqrt{K} = \int_{s_i}^{s_i+L} \sqrt{k(s)} ds \quad (2.13)$$

for a quadrupole at position s_i with length L .

A purely linear accelerator can then be constructed by the composition of the transfer matrices of all its elements. This composition yields a special example of the transfer matrix, the one that transforms the phase space coordinates of a particle at a given position to the same position in the next turn:

$$\mathbf{M}_{OT} = \prod_{w=1}^W \mathbf{M}_i \quad (2.14)$$

where \mathbf{M}_w is the transfer matrix of the w th element, W is the number of elements in the accelerator and the product denotes the repeated matrix multiplication from the left. Figure 2.4 illustrates this setup. The phase advance of one turn

$$Q_z \equiv \frac{1}{2\pi} \int_{s_0}^{s_0+C} \frac{ds}{\beta_z(s)}, \quad (2.15)$$

normalised by 2π , is called the *betatron tune*.

A general form of Eq. (2.10) is

$$\begin{pmatrix} \sqrt{\frac{\beta_b}{\beta_a}} (\cos \varphi_{ab} + \alpha_a \sin \varphi_{ab}) & \sqrt{\beta_a \beta_b} \sin \varphi_{ab} \\ \frac{\alpha_a - \alpha_b}{\sqrt{\beta_a \beta_b}} \cos \varphi_{ab} - \frac{\beta + \alpha_a \alpha_b}{\sqrt{\beta_a \beta_b}} \sin \varphi_{ab} & \sqrt{\frac{\beta_a}{\beta_b}} (\cos \varphi_{ab} - \alpha_b \sin \varphi_{ab}) \end{pmatrix} \quad (2.16)$$

where the quantity

$$\alpha(s) = -\frac{1}{2} \frac{d\beta(s)}{ds} \quad (2.17)$$

is called α function. α , β function and a third quantity

$$\gamma(s) = \frac{1 + \alpha^2(s)}{\beta(s)} \quad (2.18)$$

are called *Twiss parameters*.

For convenience and later usage we introduce the following short-hand notation:

$$\varphi_{z,ab} = \varphi_z(s_b) - \varphi_z(s_a) + 2\pi Q_z \Theta(s_a, s_b) \quad (2.19)$$

which is the *phase advance* between position s_a and s_b , taking into account the relative position of s_a to s_b . If element b lies upstream from element a , the interval *wraps around* the end of the lattice definition and the tune has to be added to the phase advance. For this the following definition is used:

$$\Theta(s_a, s_b) = \begin{cases} 1 & \text{if } s_a > s_b \\ 0 & \text{else} \end{cases} . \quad (2.20)$$

The particles motion in phase space follows a tilted ellipse which is described by

$$\gamma(s)z^2(s) + 2\alpha(s)z(s)p_z(s) + \beta(s)p_z^2(s) = 2J_z \quad (2.21)$$

where J_z is called the *action*³. The area of the ellipse is $2J_z\pi$.

The one turn map in this form can be retrieved by setting $\beta_a = \beta_b$, $\alpha_a = \alpha_b$ and $\varphi_{ab} = 2\pi Q$:

$$M_{OT} = \begin{pmatrix} \cos(2\pi Q_z) + \alpha_a \sin(2\pi Q_z) & \beta_a \sin(2\pi Q_z) \\ -\gamma \sin(2\pi Q_z) & \cos(2\pi Q_z) - \alpha_a \sin(2\pi Q_z) \end{pmatrix} . \quad (2.22)$$

2.1.2 Courant-Snyder coordinates

If one plots the phase space of a particle at a certain position s_a over many turns, it draws an ellipse with area $2J_z\pi$ where J_z is called *action*. Particle motion is easier expressed in Courant-Snyder coordinates [25, 26]

$$\begin{pmatrix} \hat{z} \\ \hat{p}_z \end{pmatrix} = \begin{pmatrix} \frac{1}{\sqrt{\beta_z}} & 0 \\ \frac{\alpha_z}{\sqrt{\beta_z}} & \sqrt{\beta_z} \end{pmatrix} \begin{pmatrix} z \\ p_z \end{pmatrix} \quad (2.23)$$

³Often a quantity $\epsilon_z^{\text{part}} = 2J_z$ is defined, called the single particle emittance. It must not be confused with the *beam emittance* $\epsilon_z = \frac{1}{2} \langle \epsilon_z^{\text{part}} \rangle$.

which transforms the phase space ellipse into a circle with radius $\sqrt{2J_z}$. The transformation

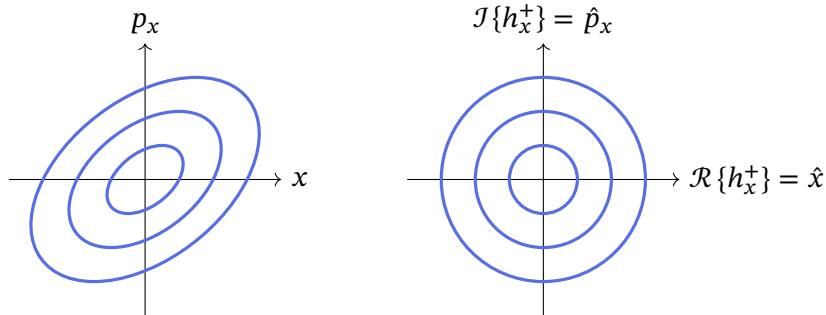


Figure 2.5: In physical coordinates the turn-by-turn movement of the particle draws an ellipse. Transformation to Courant-Snyder coordinates turns this ellipse into a circle.

is illustrated in Figure 2.6. In the following Courant-Snyder coordinates will frequently be abbreviated by *CS coordinates*.

The transformation matrix in Eq. (2.23) is called \mathbf{T} for the rest of this chapter. Applying \mathbf{T} to the one turn map, one can see that the one-turn evolution of the particle is now a rotation of $2\pi Q_z$:

$$\mathbf{T} \mathbf{M}_{\text{OT}} \mathbf{T}^{-1} = \begin{pmatrix} \cos(2\pi Q_z) & -\sin(2\pi Q_z) \\ \sin(2\pi Q_z) & \cos(2\pi Q_z) \end{pmatrix} . \quad (2.24)$$

It is often convenient to express the Courant-Snyder coordinates in their complex form:

$$h_z^\pm \equiv \hat{z} \mp i \hat{p}_z \quad (2.25)$$

and the one turn map simplifies further to a rotation about $2\pi Q_z$,

$$\mathbf{M}_{\text{OT}} h_z^\pm = e^{\mp 2\pi i Q_z} h_z^\pm . \quad (2.26)$$

In a linear lattice, the particle motion in complex Courant-Snyder coordinates at turn $N + 1$ and position s in the ring reads

$$h_z^\pm(s, N) = \sqrt{2J_z} e^{\mp i[2N\pi Q_z + \varphi_z(s) + \varphi_{z,0}]} \quad (2.27)$$

with $\varphi_{z,0}$ being a phase offset given by initial conditions.

The formulae above assume no coupling between the transverse planes. Before we continue to dive into the depths of general normalised coordinates for non-linear optics, we

introduce more general coordinates and maps, mixing the two planes:

$$\begin{pmatrix} x \\ p_x \\ y \\ p_y \end{pmatrix}_b = \mathbf{M} \begin{pmatrix} x \\ p_x \\ y \\ p_y \end{pmatrix}_a \quad (2.28)$$

where the transfer map \mathbf{M} now is a 4×4 matrix. For convenience, the vector containing the 4D coordinates will be called \vec{z} .

2.2 Hamiltonian description and Lie maps

Some preliminaries are needed to describe the particle motion using the Hamiltonian description and Lie transformations. A thorough repetition of the topic of Lie groups and Lie algebras can not be given in the scope of this thesis, the reader may consult [27].

The general Hamiltonian of a charged particle in a circular accelerator is [24, 28]

$$\hat{H} = \frac{\delta}{\beta_0} - (1+hx) \sqrt{\left(\delta + \frac{1}{\beta_0} - \frac{q\varphi}{cP_0} \right)^2 - (p_x - a_x)^2 - (p_y - a_y)^2} - \frac{1}{\beta_0^2 \gamma_0^2} - (1+hx)a_s \quad (2.29)$$

with the following definitions:

P_0	reference momentum,
$\delta = \frac{p_z}{P_0}$	relative longitudinal momentum deviation,
$h = \frac{1}{\rho}$	local curvature with ρ being the local curvature radius,
β_0, γ_0	relativistic factors,
q	the particle's charge,
φ	the electric field,
$a_x = \frac{q}{P_0} A_x, a_y = \frac{q}{P_0} A_y$	the normalised transverse components of the vector potential (A_x, A_y),
$a_s = \frac{q}{P_0} A_s$	the normalised longitudinal component of the vector potential

The Hamiltonian equations of motion [29] read

$$\frac{dz}{ds} = \frac{\partial \hat{H}}{\partial p_z} \quad \text{and} \quad \frac{dp_z}{ds} = -\frac{\partial \hat{H}}{\partial z} \quad (2.30)$$

for canonical variables z and p_z . The previous example of a quadrupole is again used to demonstrate this approach. The Hamiltonian for a particle moving through a single

quadrupole is obtained from putting the corresponding vector potential

$$a_s = -\frac{k_1}{2}(x^2 - y^2) \quad (2.31)$$

$$a_x = a_y = \varphi = 0 \quad (2.32)$$

and 0 curvature ($h = 0$):

$$\hat{H} = \frac{\delta}{\beta_0} - \sqrt{\left(\delta + \frac{1}{\beta_0}\right)^2 - p_x^2 - p_y^2 - \frac{1}{\beta_0^2 \gamma_0^2}} + \frac{k_1}{2}(x^2 - y^2) \quad (2.33)$$

$$\hat{H} = \frac{p_x^2 + p_y^2}{2} + \left(\frac{\delta}{2\beta_0\gamma_0}\right)^2 + \frac{k_1}{2}(x^2 - y^2) + O(2nd) \quad (2.34)$$

In the simple example at hand, only one on-momentum particle is considered:

$$\hat{H} = \frac{k_1}{2}(x^2 - y^2) + \frac{p_x^2 + p_y^2}{2} \quad (2.35)$$

Plugging this consecutively into the Hamiltonian equations of motion, yields

$$\frac{dx}{ds} = \frac{\partial \hat{H}}{\partial p_x} = p_x \quad (2.36)$$

$$\Rightarrow \frac{d^2x}{ds^2} = \frac{dp_x}{ds} = -k_1 x \quad (2.37)$$

which coincides with Hill's equation, Eq. (2.4).

Poisson brackets,

$$[f, g] = \sum_{z \in \{x, y\}} \left(\frac{\partial f}{\partial z} \frac{\partial g}{\partial p_z} - \frac{\partial f}{\partial p_z} \frac{\partial g}{\partial z} \right) \quad (2.38)$$

can be used to rewrite the Hamiltonian equations:

$$[z, \hat{H}] = \frac{\partial \hat{H}}{\partial p_z} \quad \text{and} \quad [p_z, \hat{H}] = -\frac{\partial \hat{H}}{\partial z} \quad (2.39)$$

The Poisson brackets form a *Lie algebra* and therefore some properties can be utilised. First, we define a *Lie operator* acting on g

$$:f: g = [f, g] \quad (2.40)$$

Then we can use the exponential parameterisation of Lie groups to move away from the origin [27] and describe the particle motion going through an element w in the lattice using the *kick Hamiltonian* of this element, which is constructed by multiplying the thin lens Hamiltonian by the length of the element, $H = \hat{H}L$

$$x(s_b) = e^{:H:} x(s_a) \quad (2.41)$$

with L being the length of the element. To illustrate this, once again the quadrupole is used. Some helpful identities, for convenience:

$$\begin{aligned} :g:^2 &= :g: \circ :g: \\ :x^2: f(x, p_x) &= 2x \frac{\partial f(x, p_x)}{\partial p_x} \\ :p^2: f(x, p_x) &= -2p_x \frac{\partial f(x, p_x)}{\partial x} \quad . \end{aligned} \quad (2.42)$$

Now it is possible to show

$$\begin{aligned} x(s_b) = e^{:H:} x(s_a) &= x(s_a) - L p_x(s_a) - \frac{1}{2} L^2 k_1 x(s_a) + \frac{1}{6} L^3 k_1 p_x(s_a) \\ &\quad + \frac{1}{24} k_1^2 x(s_a) - \frac{1}{120} k_1^2 p_x(s_a) + \dots \\ &= x(s_a) \cos(L\sqrt{k_1}) - \frac{p(s_a)}{L\sqrt{k_1}} \sin(L\sqrt{k_1}) \end{aligned} \quad (2.43)$$

which agrees with the propagation through a quadrupole given in Eq. (2.11), noting that the Hamiltonian, and therefore k , is constant inside the (ideal) quadrupole described by the Hamiltonian Eq. (2.35). Usually, non-linear terms are collected into a non-linear map $e^{:H:}$, generated by the non-linear Hamiltonian and a linear transfer map (rotation in CS-coordinates) \mathbf{M} :

$$\mathcal{M}_w = e^{:H_w:} \mathbf{M}_w \quad , \quad (2.44)$$

where the subscript w denotes the map of element w in the lattice and the particle motion is propagated through the element by

$$\vec{z}(s_w + L) = e^{:H_w:} \mathbf{M}_w \vec{z}(s_w) \quad (2.45)$$

for element w with length L .

2.3 The normal form approach

In order to derive optics parameters from Hamiltonian terms the normal form approach – usually encountered in treatments of non-linear optics – is useful. It is described in its full mathematical detail in [30, 26] and more illustrative in [31, 32, 28].

In the formalism of complex CS-coordinates, a transfer map can be written as

$$\begin{pmatrix} h_x^+ \\ h_x^- \\ h_y^+ \\ h_y^- \end{pmatrix}_b = \mathbf{M} \begin{pmatrix} h_x^+ \\ h_x^- \\ h_y^+ \\ h_y^- \end{pmatrix}_a \quad (2.46)$$

where

$$\mathbf{M} = \begin{pmatrix} m_{1000}^1 & m_{0100}^1 & m_{0010}^1 & m_{0001}^1 \\ m_{1000}^2 & m_{0100}^2 & m_{0010}^2 & m_{0001}^2 \\ m_{1000}^3 & m_{0100}^3 & m_{0010}^3 & m_{0001}^3 \\ m_{1000}^4 & m_{0100}^4 & m_{0010}^4 & m_{0001}^4 \end{pmatrix}. \quad (2.47)$$

The significance of the multi-index m_{jklm}^i will become clear in a moment. It shall be noted that some symmetry relation applies:

$$m_{jklm} = m_{kjml}^* \quad (2.48)$$

The map of a non-linear lattice element i cannot be described by a matrix \mathbf{M}_i only. A higher order map is necessary. Here the multi-index comes into play. Higher order maps \mathcal{M} are composed of higher order polynomials:

$$h_x^+(s_b) = \sum_{n=1}^{\infty} \sum_{j+k+l+m=n} m_{jklm}^1 (h_x^+(s_a))^j (h_x^-(s_a))^k (h_y^+(s_a))^l (h_y^-(s_a))^m. \quad (2.49)$$

The transformation to Courant-Snyder coordinates flattens the phase space of linear optics to a circle. For non-linear optics where the phase space motion is far more complicated the normal form approach can be used to transform to a new set of coordinates, the *normal form coordinates* (their exact form will be defined at the end of this section), in which the the phase space motion is flattened to a circle. Figure 2.6 illustrates how particle trajectories inside a non-linear machine evolve in phase space, CS-space and normal form space. The irregular shape of in phase space is tilted to a more "upright" form in CS-space but only a transformation to normal form space flattens the trajectory to a circle.

This map is generated by the non-linear Hamiltonian of the element. The Hamiltonian of element w evaluated at position s in multipolar expansion, reads

$$H_w = -\mathcal{R}e \left\{ \sum_{n \geq 2} (K_{n-1} + iJ_{n-1}) \frac{(x + iy)^n}{n!} \right\}_w \quad (2.50)$$

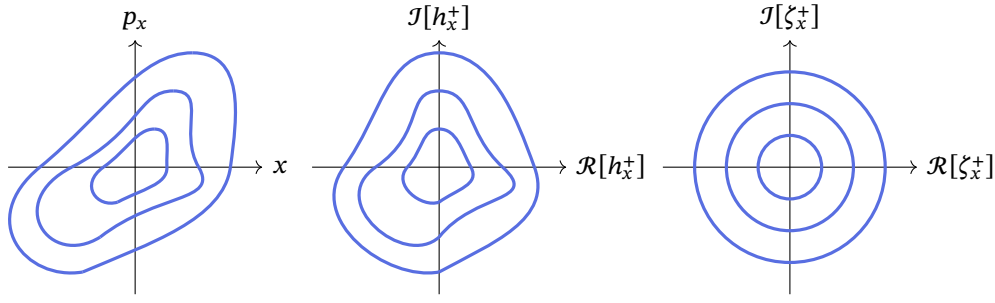


Figure 2.6: If non-linearities are present in the lattice, the phase space motion of the particles is deformed and does not show the form of an ellipse any more. Transformation to Courant-Snyder coordinates tilts the phase space but does not remove irregular deformations. Only a transformation into normal form coordinates restores a perfect circle.

where K_{n-1} and J_{n-1} are normal and skew integrated multipolar field strengths,

$$K_n = \frac{1}{n!} \frac{\partial^n B_y}{\partial x^n} \quad (2.51)$$

$$J_n = \frac{1}{n!} \frac{\partial^n B_x}{\partial x^n} \quad (2.52)$$

i.e. a pure dipole has only K_0 , a pure quadrupole only K_1 etc.

In complex Courant-Snyder coordinates, the Hamiltonian Eq. (2.50), evaluated at position s_i , can be written in the form

$$H_w(s_i) = \sum_{n \geq 2} \sum_{j+k+l+m=n} h_{w,jklm} e^{i[(j-k)\varphi_{x,wi} + (l-m)\varphi_{y,wi}]} (h_x^+)^j (h_x^-)^k (h_y^+)^l (h_y^-)^m \quad , \quad (2.53)$$

where the Hamiltonian term $h_{w,jklm}$ is defined as

$$h_{w,jklm} = \frac{\Omega(l+m)K_{w,n-1} + i[1 - \Omega(l+m)]J_{w,n-1}}{j! k! l! m! 2^{j+k+l+m}} i^{l+m} (\beta_{x,w})^{\frac{j+k}{2}} (\beta_{y,w})^{\frac{l+m}{2}} \quad . \quad (2.54)$$

The Hamiltonian of the whole lattice is denoted by

$$H(s_i) = \sum_w^W H_w(s_i) \quad . \quad (2.55)$$

In Eq. (2.54) $\beta_{z,w}$ is the β function of the corresponding plane at position w and

$$\Omega(a) = \begin{cases} 1 & \text{if } a \text{ is even} \\ 0 & \text{if } a \text{ is odd} \end{cases} \quad . \quad (2.56)$$

The one-turn map of an accelerator now reads

$$\mathcal{M}_{OT} = \prod_{i=0}^W e^{H_i} \mathbf{M}_i \quad . \quad (2.57)$$

It shall be noted that Lie maps do not, in general, commute and, in order to construct a one-turn equivalent of the Hamiltonian, the Baker-Campbell-Hausdorff formula has to be applied:

$$e^{:H_1}:} e^{:H_2}:} = e^{:H_1+H_2+\frac{1}{2}[H_1,H_2]+\frac{1}{12}[H_1,[H_1,H_2]]+\dots:} , \quad (2.58)$$

as opposed to Eq. (2.55) which is only a simple summation of Hamiltonian coefficients to build one single Hamiltonian operator.

The transformation from complex Courant-Snyder coordinates to normal form coordinates and back is performed using a generating function F :

$$\zeta_z^\pm = e^{-:F:} h_z^\pm \quad (2.59)$$

$$h_z^\pm = e^{:F:} \zeta_z^\pm . \quad (2.60)$$

The *normal form coordinates* ζ_z^\pm can be expressed in terms of the normal form phase ψ and normal form invariant I_z :

$$\zeta_z^\pm(s_i) = \sqrt{2I_z} e^{i[\mp\psi_z(s_i)+\psi_{z,0}]} . \quad (2.61)$$

Since ψ and I_z are canonical variables, the Poisson bracket between any of the normal form coordinates can be calculated easily:

$$[(\zeta_x^+)^n, (\zeta_x^-)^m] = -2i nm (\zeta_x^+)^{n-1} (\zeta_x^-)^{m-1} , \quad (2.62)$$

and all other combinations are zero.

2.4 Resonance driving terms

The following commutative diagram shows the transformation from the Courant-Snyder one turn map to the normal form one turn map:

$$\begin{array}{ccc} \vec{\zeta}(N) & \xrightarrow{\mathcal{M}_{\text{OT}}=e^{: \langle H \rangle_\varphi :} R} & \vec{\zeta}(N+1) \\ \uparrow e^{-:F:} & & \uparrow e^{-:F:} \\ \vec{h}(N) & \xrightarrow{\mathcal{M}_{\text{OT}}} & \vec{h}(N+1) \end{array} \quad (2.63)$$

The motion in normal form coordinates \mathcal{M}_{OT} consists of a pure rotation about the phase φ and the action of the phase-independent Hamiltonian $\langle H \rangle_\varphi$. The one turn rotation advances the phases by $2\pi Q_z$:

$$R_z \psi = \psi + 2\pi Q_z \quad (2.64)$$

and an arbitrary rotation may be defined as

$$R(\alpha)\psi = \psi + \alpha \quad . \quad (2.65)$$

The normal form coordinate of the particle at position s and turn N reads

$$\zeta_Z^\pm(s, N) = \sqrt{2I_Z} e^{\mp i[\psi_{z,0} + NQ_z + \psi(s)]} \quad . \quad (2.66)$$

Since the diagram is commutative one can propagate the complex Courant-Snyder coordinates from one position in the lattice to another by using the normal form approach:

$$h_Z^\pm(s_1) = e^{iF} \mathcal{M}_{OT} e^{-iF} h_Z^\pm(s_0) \quad . \quad (2.67)$$

From that one can derive the relation between the Hamiltonian and the generating function F :

$$F = \frac{H^\ddagger}{1-R} \quad (2.68)$$

where H^\ddagger denotes the phase-dependent part of H :

$$H^\ddagger = H - \langle H \rangle_\varphi \quad , \quad (2.69)$$

and the fraction $\frac{1}{1-R}$ denotes, in accordance with convention and abusing notation, the matrix inverse of $1-R$. The generating function F can be expressed in polynomial form

$$F(s_i) = \sum_{jklm} f_{jklm}(s_i) (\zeta_x^+)^j (\zeta_x^-)^k (\zeta_y^+)^l (\zeta_y^-)^m \quad (2.70)$$

and Eq. (2.68) has to hold for each polynomial order separately. Thus one can relate

$$f_{jklm}(s_i) = \frac{\sum_w h_{w,jklm} e^{i[(j-k)\varphi_{x,wi} + (l-m)\varphi_{y,wi}]} }{1 - e^{2\pi i[(j-k)Q_x + (l-m)Q_y]}} \quad . \quad (2.71)$$

The enumerator of f_{jklm} is referred to as *resonance driving term*⁴.

2.4.1 Influence of linear lattice imperfections on betatron phases

This section revises the derivation of phase advance beating and β beating from quadrupolar field errors by reproducing the steps of [33] and [34]. Only normal quadrupolar field errors are considered. In this case the generating function F reads

$$F(s_j) = f_{2000,j} (\zeta_{x,s_j}^+)^2 + f_{0200,j} (\zeta_{x,s_j}^-)^2 + f_{0020,j} (\zeta_{y,s_j}^+)^2 + f_{0002,j} (\zeta_{y,s_j}^-)^2 \quad ,$$

⁴Sometimes the whole expression f_{jklm} is called resonance driving term.

with

$$f_{2000,j} = \frac{\sum^W \delta K_{w,1} \beta_{x,w} e^{2i\varphi_{x,wj}}}{8(1 - e^{4i\pi Q_x})} . \quad (2.72)$$

The complex Courant-Snyder coordinates can be calculated from the normal form coordinates by Eq. (2.60)

$$h_x^+ = \zeta_x^+ + :F: \zeta_x^+ + \frac{1}{2} :F:^2 \zeta_x^+ + O(f^3) . \quad (2.73)$$

Using the Poisson bracket identity Eq. (2.62) one can calculate

$$\begin{aligned} :F: \zeta_x^+ &= [f_{0200} (\zeta_x^-)^2, \zeta_x^+] = 4i f_{0200} \zeta_x^- , \\ :F:^2 \zeta_x^+ &= [f_{2000} (\zeta_x^+)^2, 4i f_{0200} \zeta_x^-] = -|4f_{2000}|^2 \zeta_x^+ . \end{aligned}$$

This can be used to calculate the C-S coordinate at position s_j and turn N :

$$\begin{aligned} h_x^+(s_j, N) &= e^{:F:} \zeta_x^+(s_j, N) \\ &= \zeta_x^+(s_j, N) + 4i f_{2000,j}^* \zeta_x^-(s_j, N) + \frac{1}{2} |4f_{2000,j}|^2 \zeta_x^+(s_j, N) + O(f^3) \end{aligned} \quad (2.74)$$

which made use of the fact that $f_{2000}^* = f_{0200}$ to simplify the expression. The $O(f^3)$ term collects all third order contributions of $\mathcal{R}e\{f_{2000,j}\}$, $\mathcal{I}m\{f_{2000,j}\}$ and $|f_{2000,j}|$.

The phase of the real signal $\hat{x}_j = \mathcal{R}e\{h_x^+(s_j)\}$ reads, up to first order,

$$\hat{x}_j = \mathcal{R}e\left\{\left(1 + 4i f_{2000,j}^*\right) \sqrt{2J_x} e^{-i[NQ_x + \psi_{x,0j}]}\right\} . \quad (2.75)$$

The effect of the RDTs $f_{jklm,i}$ on the phase of the main tune line is the argument of the term in parenthesis in Eq. (2.75):

$$\begin{aligned} \arg(1 + 4i f_{2000,j}^*) &= \text{atan}\left(\frac{-4\mathcal{R}e\{f_{2000,i}\}}{1 + 4\mathcal{I}m\{f_{2000,j} + |4f_{2000,j}|^2\}}\right) \\ &\approx -4\mathcal{R}e\{f_{2000,i}\} - 16\mathcal{R}e\{f_{2000,i}\}\mathcal{I}m\{f_{2000,i}\} . \end{aligned} \quad (2.76)$$

To get the β function under the effect of focusing errors, one can compare the amplitude $\sqrt{\beta_z J_z}$ of the coordinate by considering the change in J_z negligible:

$$\begin{aligned} \sqrt{2\beta_x J_x} &= \sqrt{2\beta_x^m J_x} \mathcal{R}e\{1 + 4i f_{2000,i}\} \\ \beta_x &= \beta_x^m (1 + 8\mathcal{I}m\{f_{2000,i}\}) + O(f^2) . \end{aligned} \quad (2.77)$$

Since only f_{2000} appears in the phase beating the indices 2000 will be suppressed from now on. A detuning ΔQ_z is generated by the phase independent Hamiltonian terms $h_{w,ii jj}$. The only quadrupolar contribution comes from the term h_{1100} . The tune in Eq. (2.75) consists

of

$$Q_x = Q_x^m + \Delta Q_x \quad (2.78)$$

where Q_x^m is the model horizontal tune and

$$2\pi\Delta Q_x = -\frac{\partial\langle H \rangle_\varphi}{\partial J_x} = -\frac{\partial 2J_x h_{1100}}{\partial J_x} = -2h_{1100} + O(J_x) \quad (2.79)$$

The Hamiltonian of the whole accelerator reads

$$H(s_a) = \sum_w^W H_w(s_a) \quad (2.80)$$

with $H_w(s_a)$ being the Hamiltonian term from Eq. (2.55). The sum over w in Eq. (2.80) runs over each element w in the accelerator. The accumulated phase shift due to the detuning between elements i and j reads:

$$h_{1100,ij} \equiv -\frac{\text{sgn}(j-i)}{4} \sum_I \beta_{w,x}^m \delta K_{w,1} + O(\delta K_1^2) \quad (2.81)$$

I is the interval $[\min(i, j), \max(i, j)]$ and $\text{sgn}(x)$ denotes the sign function:

$$\text{sgn}(x) = \begin{cases} -1 & \text{if } x < 0 \\ 0 & \text{if } x = 0 \\ 1 & \text{if } x > 0 \end{cases} \quad (2.82)$$

The total phase advance beating is then the sum of the accumulated detuning from Hamiltonian terms and the phase beating from the RDTs:

$$\Delta\varphi_{x,ij} = -2h_{1100,ij} - 4\mathcal{R}e\{f_j - f_i\} + O(f^2) \quad (2.83)$$

With the following identity [31, 35]:

$$f_j = \text{sgn}(j-i) \frac{1}{8} \sum_{w \in I} \beta_w^m \delta K_{w,1} e^{2i\varphi_{wj}^m} + f_i e^{2i\varphi_{ij}^m}, \quad (2.84)$$

we can eliminate f_j from Eq. (2.83). Here and in the following we consider only the horizontal plane and thus we omit the index x in the optical functions φ_{ab} , β_a and the quadrupole field $K_{a,1}$, for arbitrary indices a and b . For compactness we rename the first part of f_j to

$$A_{ij} = \text{sgn}(j-i) \frac{1}{8} \sum_{w \in I} \beta_w^m \delta K_{w,1} e^{2i\varphi_{wj}^m} \quad (2.85)$$

We can simplify the last term of Eq. (2.83) [33]:

$$\begin{aligned}
\mathcal{R}e\{f_j - f_i\} &= -\mathcal{R}e\{A_{ij}\} + \mathcal{R}e\{e^{2i\varphi_{ij}^m}\} \mathcal{I}m\{f_i\} + \mathcal{I}m\{e^{2i\varphi_{ij}^m}\} \mathcal{R}e\{f_i\} - \mathcal{R}e\{f_i\} \\
&= -\mathcal{R}e\{A_{ij}\} + (1 - 2\sin^2\varphi_{ij}^m) \mathcal{R}e\{f_i\} - 2\sin\varphi_{ij}^m \cos\varphi_{ij}^m \mathcal{I}m\{f_i\} - \mathcal{R}e\{f_i\} \\
&= -\mathcal{R}e\{A_{ij}\} + \mathcal{R}e\{f_i\}(-2\sin^2\varphi_{ij}^m) - \mathcal{I}[f_i] 2\sin\varphi_{ij}^m \cos\varphi_{ij}^m \quad (2.86)
\end{aligned}$$

Equation (2.83) now reads

$$\begin{aligned}
\Delta\varphi_{ij} &= -2h_{1100,ij} - 4\mathcal{R}e\{A_{ij}\} - 8\sin^2\varphi_{ij}^m \mathcal{R}e\{f_i\} - 8\sin\varphi_{ij}^m \cos\varphi_{ij}^m \mathcal{I}m\{f_i\} + O(f^2) \\
&= \bar{h}_{ij} - 8\sin^2\varphi_{ij}^m \mathcal{R}e\{f_i\} - 8\sin\varphi_{ij}^m \cos\varphi_{ij}^m \mathcal{I}m\{f_i\} + O(f^2) \quad (2.87)
\end{aligned}$$

We simplified the equation with the definition

$$\bar{h}_{ij} \equiv -2h_{1100,ij} - 4\mathcal{R}e\{A_{ij}\} = \sum_{w \in I} \beta_w^m \delta K_{w,1} \sin^2\varphi_{wj}^m \quad (2.88)$$

Equation (2.87) will be used in chapter 3 to calculate a more precise β function and in chapter 4 to construct a local observable.

2.4.2 Coupling RDTs

Linear transverse coupling is the effect that the linear optics of one plane influences the optics parameters of the other plane. This can have undesired impact on beam size and luminosity as well as on Landau damping⁵.

The generating function with only skew quadrupoles reads

$$F = f_{1010} \zeta_x^+ \zeta_y^+ + f_{1001} \zeta_x^+ \zeta_x^- + f_{0101} \zeta_x^- \zeta_y^- + f_{0110} \zeta_x^- \zeta_y^+ \quad (2.89)$$

Following the same steps as in the previous section one gets the coupled motion:

$$h_x(s_j, N) = \zeta_x^+(s_j, N) + 2if_{0101}(s_j) \zeta_y^-(s_j, N) + 2if_{0110}(s_j) \zeta_y^+(s_j, N) \quad (2.90)$$

with

$$\begin{aligned}
f_{0101}(s_j) &= \frac{\sum_w J_{1,w} \sqrt{\beta_{x,w} \beta_{y,w}} e^{i[\varphi_{wj,x} + \varphi_{wj,y}]} }{4(1 - e^{2\pi i(Qx + Qy)})} \quad , \\
f_{0110}(s_j) &= \frac{\sum_w J_{1,w} \sqrt{\beta_{x,w} \beta_{y,w}} e^{i[\varphi_{wj,x} - \varphi_{wj,y}]} }{4(1 - e^{2\pi i(Qx - Qy)})} \quad . \quad (2.91)
\end{aligned}$$

⁵Landau damping is a mechanism, first discovered in plasma physics[36, 37], by which larger tune spread leads to a more stable beam.

using equations (2.54) and (2.71). The value of the coupling resonance driving terms f_{1010} and f_{1001} and their complex conjugates determines the strength of the coupling between the planes. If both are zero there is no coupled motion.

2.5 Calculation of optics functions

2.5.1 β function measurement

To calculate the β function at a location s in the machine, two methods are routinely used in the LHC: the first calculates the β function from the amplitude ($\propto \sqrt{2I\beta}$) and the second one uses the phase advance. In this work only the second one is considered and the task of chapter 3 is the improvement of this method.

In order to get the real β function from phase, one can start with the transfer matrix \mathbf{M}_{ij} between elements i and j in Eq. (2.16). The quotient of the first row elements reads

$$\frac{(m_{ij})_{11}}{(m_{ij})_{12}} = \frac{1}{\beta_i} (\cot \varphi_{ij} + \alpha_i) \quad . \quad (2.92)$$

Subtracting the quotient of the first row elements of the transfer matrix between elements i and k , $\frac{(m_{ik})_{11}}{(m_{ik})_{12}}$, yields

$$\frac{(m_{ij})_{11}}{(m_{ij})_{12}} - \frac{(m_{ik})_{11}}{(m_{ik})_{12}} = \frac{1}{\beta_i} (\cot \varphi_{ij} - \cot \varphi_{ik}) \quad . \quad (2.93)$$

If the region between the three BPMs i , j and k is free of imperfections the model transfer matrix equals the measured one $\mathbf{M}_{ij} = \mathbf{M}_{ij}^m$ and, consequently,

$$\begin{aligned} \frac{1}{\beta_i^m} (\cot \varphi_{ij}^m - \cot \varphi_{ik}^m) &= \frac{1}{\beta_i} (\cot \varphi_{ij} - \cot \varphi_{ik}) \\ \Rightarrow \beta_i &= \frac{\cot \varphi_{ij} - \cot \varphi_{ik}}{\cot \varphi_{ij}^m - \cot \varphi_{ik}^m} \beta_i^m \quad . \end{aligned} \quad (2.94)$$

Equation (2.94) was developed in [38] and used for LEP and in run I of LHC.

For optimal operation of the machine a precise control of the β function is needed. Firstly, the particles must stay within the boundaries of the physical aperture and at the interaction point the beam size has to be as small as possible to increase luminosity. And secondly, a too large deviation from the optical axis inside a higher order magnet may lead to an undesirable feed-down of the orbit offset.

The deviation of the β function from its design value is called *beta beating* and defined as

$$\frac{\Delta\beta}{\beta^m} = \frac{\beta - \beta^m}{\beta^m} . \quad (2.95)$$

The β beating is often expressed in percent. As stated in the introduction, the goal is to limit β beating for machine protection reasons and to optimise the luminosity. The effect of β beating is particularly problematic in strong magnetic fields where only small deviations from the design orbit create large perturbations the particle dynamics.

2.5.2 Coupling measurement

One possible method to calculate coupling used for LHC – which is independent of BPM calibration errors – makes use of two nearby BPMs in order to cancel out calibration factors. It is therefore called the *two BPM method*. This method is described in this section.

Repeating the calculations of section 2.4.2 for all transverse C-S coordinates yields

$$\begin{aligned} h_x^+ &= \zeta_x^+ + 2if_{1010}^*\zeta_y^- + 2if_{1001}^*\zeta_y^+ \\ h_y^+ &= \zeta_y^+ + 2if_{1010}^*\zeta_x^- + 2if_{1001}^*\zeta_x^+ \\ h_x^- &= \zeta_x^- - 2if_{1010}\zeta_y^+ - 2if_{1001}\zeta_y^- \\ h_y^- &= \zeta_y^- - 2if_{1010}\zeta_x^+ - 2if_{1001}^*\zeta_x^- . \end{aligned} \quad (2.96)$$

The Fourier transform of the coordinates reads

$$\mathcal{F}\{h_z^\pm\}(\omega) = \sqrt{2I_z}e^{i\varphi_{z,0}}\delta(Q_z \pm \omega) , \quad (2.97)$$

where $\delta(x)$ denotes the Dirac delta function. Figure 2.7 shows the spectrum of h_x^+ and h_y^+ excited by an AC-dipole and with coupling. The driven fractional tunes are $Q_x^d = 0.270$ and $Q_y^d = 0.322$. The respective main lines are well dominating the spectrum and the secondary lines induced by coupling are clearly visible at the position of the respective other plane's tune. For the following it is convenient to introduce a shorthand notation for the spectral lines $\mathcal{F}\{h_z^\pm\}(n_x Q_x + n_y Q_y)$:

$$\begin{aligned} H^\pm(n_x, n_y) &= \mathcal{F}\{h_x^\pm\}(n_x Q_x + n_y Q_y) \\ V^\pm(n_x, n_y) &= \mathcal{F}\{h_y^\pm\}(n_x Q_x + n_y Q_y) . \end{aligned} \quad (2.98)$$

If the BPM calibration is not perfect the measured H and V lines are not proportional w.r.t.

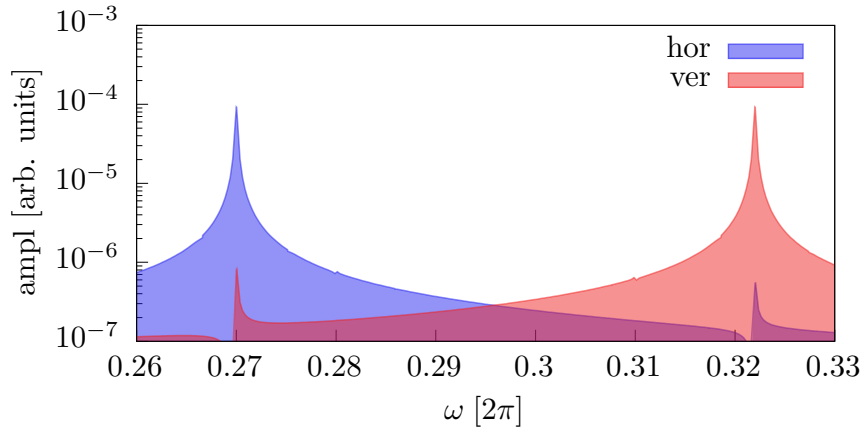


Figure 2.7: This example plot shows the Fourier transform of horizontal and vertical particle motion from simulations with an AC-dipole and coupling sources. The vertical and horizontal fractional driven tunes are $Q_x^d = 0.270$ and $Q_y^d = 0.322$.

each other:

$$\begin{aligned} x^{\text{meas}} &= C_x x \\ y^{\text{meas}} &= C_y y \quad . \end{aligned} \quad (2.99)$$

The calibration factors $C_{x/y}$ cancel out if one divides the spectral line by the amplitude of the main line:

$$\begin{aligned} A_{0,n_y}^+ &= \frac{H^+(0, n_y)}{|H^+(1, 0)|} \\ B_{n_x, 0}^+ &= \frac{V^+(n_x, 0)}{|V^+(0, 1)|} \quad . \end{aligned} \quad (2.100)$$

Important for the coupling calculation are the following normalised spectral lines:

$$A_{0,1}^+ = \frac{H^+(0, 1)}{|H^+(1, 0)|} = 2i \sqrt{\frac{J_y}{J_x}} f_{1001}^* e^{-i\varphi_y} \quad (2.101)$$

$$B_{1,0}^+ = \frac{V^+(1, 0)}{|V^+(0, 1)|} = 2i \sqrt{\frac{J_x}{J_y}} f_{1001} e^{-i\varphi_x} \quad (2.102)$$

which contain f_{1001} and

$$A_{0,-1}^+ = \frac{H^+(0, -1)}{|H^+(1, 0)|} = 2i \sqrt{\frac{J_y}{J_x}} f_{1010}^* e^{i\varphi_y} \quad (2.103)$$

$$B_{-1,0}^+ = \frac{V^+(-1, 0)}{|V^+(0, 1)|} = 2i \sqrt{\frac{J_x}{J_y}} f_{1010} e^{i\varphi_x} \quad (2.104)$$

which contain f_{1010} .

The coupling RDTs f_{1010} and f_{1001} can then be calculated by combining Eqs (2.101) with (2.102) and Eqs (2.103) with (2.104), respectively:

$$\begin{aligned} |f_{1001}| &= \frac{1}{2} \sqrt{|A_{0,1}^+ B_{1,0}^+|} \\ |f_{1010}| &= \frac{1}{2} \sqrt{|A_{0,-1}^+ B_{-1,0}^+|} \quad . \end{aligned} \quad (2.105)$$

The normalised spectral lines A_{0,n_y} and $B_{n_x,0}$ are the Fourier components of the complex coordinates. But only the projections onto the real axis can be measured. The next step is to calculate the complex coordinates from the measured ones.

Since $h_z^\pm = z \pm ip_z$ the complex coordinate can be obtained from position and momentum. BPMs can only measure position but using the position data from a second BPM one can reconstruct the momentum. The propagation of complex C-S coordinates through a region that is empty of non-linearities reads

$$\begin{pmatrix} \hat{z} \\ \hat{p}_z \end{pmatrix}_b = \mathbf{R}_{ab} \begin{pmatrix} \hat{z} \\ \hat{p}_z \end{pmatrix}_a \quad (2.106)$$

where the transfer matrix \mathbf{R}_{ab} is a simple rotation matrix as discussed in section 2.1.2. From this one can reconstruct the momentum:

$$\hat{p}_{z,a} = \frac{\hat{z}_b}{\cos \varphi_{ab}} + \hat{z}_a \tan \varphi_{ab} \quad (2.107)$$

where φ_{ab} is the phase advance between the two positions s_a and s_b . Therefore:

$$h_z^\pm(s_a) = \hat{z}_a - i \left(\frac{\hat{z}_b}{\cos \varphi_{ab}} + \hat{z}_a \tan \varphi_{ab} \right) = \hat{z}_a (1 - i \tan \varphi_{ab}) - i \frac{\hat{z}_b}{\cos \varphi_{ab}} \quad . \quad (2.108)$$

Since the Fourier transform is linear, this identity can be propagated to the spectral lines:

$$H^+(n_x, n_y)_a = (1 - i \tan \varphi_{ab}) H(n_x, n_y)_a - \frac{i}{\cos \varphi_{ab}} H(n_x, n_y)_b \quad (2.109)$$

where $H(n_x, n_y)$ is the measured spectral line which is just the real projection of the complex line. Under the assumption that the region between s_a and s_b is free from non-linearities and coupling the action J_z does not change between the two positions and

$$\begin{aligned} |H(1, 0)_a| &= |H(1, 0)_b| = \sqrt{2J_x} \\ |V(0, 1)_a| &= |V(0, 1)_b| = \sqrt{2J_y} \quad . \end{aligned} \quad (2.110)$$

This allows to express the real normalised spectral lines as

$$\begin{aligned} A(0, n_y)_a &= \frac{H(0, n_y)_a}{|H(1, 0)_a|} = \frac{H(0, n_y)_a}{|H(1, 0)_b|} \\ B(n_x, 0)_a &= \frac{V(n_x, 0)_a}{|V(0, 1)_a|} = \frac{V(n_x, 0)_a}{|V(0, 1)_b|} . \end{aligned} \quad (2.111)$$

This can be plugged into the reconstruction formula Eq. (2.109)

$$\frac{H^+(n_x, n_y)_a}{H(1, 0)_a} = (1 - i \tan \varphi_{ab})A(n_x, n_y)_a - \frac{i}{\cos \varphi_{ab}}A(n_x, n_y)_b \quad (2.112)$$

Together with the identity

$$H(1, 0) = \frac{1}{2}(H^+(1, 0) + H^-(1, 0)) = \frac{1}{2}H^+(1, 0) \quad (2.113)$$

because $H^-(1, 0) = 0$, one can express $A^+(0, n_y)$ and $B^+(n_x, 0)$ in terms of normalised real spectral lines

$$\begin{aligned} 2A^+(n_x, n_y)_a &= (1 - i \tan \varphi_{ab})A(n_x, n_y)_a - \frac{i}{\cos \varphi_{ab}}A(n_x, n_y)_b \\ 2B^+(n_x, n_y)_a &= (1 - i \tan \varphi_{ab})B(n_x, n_y)_a - \frac{i}{\cos \varphi_{ab}}B(n_x, n_y)_b \end{aligned} \quad (2.114)$$

Which can now be plugged in Eq (2.105) to calculate the amplitude of the coupling RDTs f_{1001} and f_{1010} . To get the phase the starting point is, again, Eqs (2.101) – (2.104). The phases of $A_{0,1}$, $B_{1,0}$, $A_{0,-1}$, $B_{-1,0}$ contain the phases of the RDTs:

$$\arg(A_{0,1}) = -q_{1001} - \varphi_y + \frac{\pi}{2} \quad (2.115)$$

$$\arg(B_{1,0}) = q_{1001} - \varphi_x + \frac{\pi}{2} \quad (2.116)$$

$$\arg(A_{0,-1}) = -q_{1010} + \varphi_y + \frac{\pi}{2} \quad (2.117)$$

$$\arg(B_{-1,0}) = -q_{1010} + \varphi_x + \frac{\pi}{2} \quad (2.118)$$

where the phase $\frac{\pi}{2}$ comes from the factor i and the phases of the RDTs are defined as

$$q_{1001} \equiv \arg(f_{1001}) \quad (2.119)$$

$$q_{1010} \equiv \arg(f_{1010}) . \quad (2.120)$$

From Eq. (2.118) one gets two expressions for each RDT phase:

$$\begin{aligned} q_{1001} &= -\arg A_{0,1} - \varphi_y + \frac{\pi}{2} = \arg B_{1,0} + \varphi_x - \frac{\pi}{2} \\ q_{1010} &= -\arg A_{0,-1} + \varphi_y + \frac{\pi}{2} = -\arg B_{-1,0} + \varphi_x + \frac{\pi}{2} \end{aligned} \quad (2.121)$$

which can finally be used to calculate the RDTs using Eq. (2.105).

2.6 Forced motion

This section will introduce the process of optics measurements with an AC-dipole. As stated above, the effect of the driving of the beam motion has to be compensated and the foundation for this compensation will be explained in the following subsections.

2.6.1 Linear motion with AC dipole

In this section the C-S coordinates of the driven linear motion will be derived [17, 15]. These forced coordinates can be used to calculate the effect of the AC dipole on linear optics parameters like betatron phase, β function and linear transverse coupling.

At each turn an AC dipole located at position s_d inflicts a kick to the beam. This kick can be described in Courant-Snyder coordinates as

$$\Delta h_z^\pm(N) = iA_\theta\beta(s_d)\cos(2\pi Q_z^d N) \quad (2.122)$$

depending on the AC dipole frequency Q_z^d , the kick strength A_θ and the turn number N . Figure 2.8 shows a schematic of the beam deflection for several turns. At a small distance

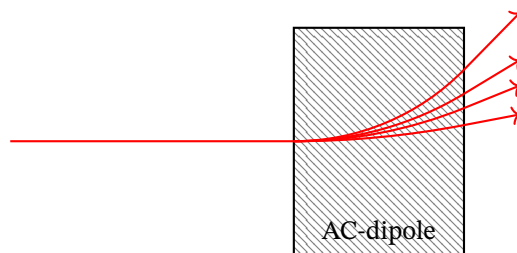


Figure 2.8: Schematic of an AC-dipole kick. The deflection $\Delta p_z = A_\theta\beta(s_d)\cos(2\pi iQ_z N)$ changes with turn number N .

ϵ after the AC-dipole the C-S coordinates of the beam read

$$h_z^\pm(s_d + \epsilon, N = 0) = h_z^\pm(s_d - \epsilon) + \Delta h_z^\pm(N = 0) \quad (2.123)$$

in the first turn where the AC dipole is active. This turn will be denoted with $N = 0$.

Under the assumption that the kick strength of the AC-dipole is ramped up slowly enough, this is an adiabatic process and the effect of the kicks can be added repeatedly for each turn. The coordinates can be propagated to an arbitrary position s in the ring to get the following

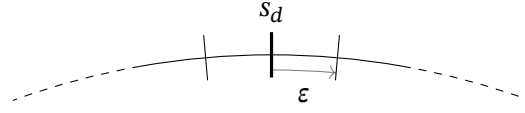


Figure 2.9: Schematic showing the positions and length occurring in Eq. (2.123). The AC-dipole is located at position s_d . The beam gets a kick when passing from $s_d - \varepsilon$ to $s_d + \varepsilon$.

expressions:

$$\begin{aligned} h_z^+(s < s_d, N) &= R_{s-s_d} \left[R^N h_z^+(s_d) + R^N \Delta h_z^+(0) + \dots + R \Delta h_z^+(N-1) \right] \\ h_z^+(s > s_d, N) &= R_{s-s_d} \left[R^N h_z^+(s_d) + R^N \Delta h_z^+(0) + \dots + R \Delta h_z^+(N-1) + \Delta h_z^+(N) \right] \quad , \end{aligned} \quad (2.124)$$

$$\begin{aligned} h_z^+(s < s_d, N) &= R_{s-s_d} \left[R^N h_z^+(s_d) + \sum_{T=1}^N R^T \Delta h_z^+(N-T) \right] \\ h_z^+(s > s_d, N) &= R_{s-s_d} \left[R^N h_z^+(s_d) + \sum_{T=0}^N R^T \Delta h_z^+(N-T) \right] \quad , \end{aligned} \quad (2.125)$$

with R being the rotation map of the linear motion. For simplicity, the following definition has been used:

$$R_{s-s_d} \equiv R(\varphi(s) - \varphi(s_d)) \quad (2.126)$$

$$\Rightarrow R_{s-s_d} h_x = h_x e^{-i\varphi_{s_d} s} \quad . \quad (2.127)$$

The cosine in Eq. (2.122) can be expressed in complex form

$$\begin{aligned} \Delta h_z^+(N) &= \frac{iA_\theta \beta(s_d)}{2} \left(e^{2\pi i Q_z^d N} + e^{-2\pi i Q_z^d N} \right) \\ &= \frac{iA_\theta \beta(s_d)}{2} (\delta_+^N + \delta_-^N) \quad , \end{aligned} \quad (2.128)$$

where δ_\pm is defined as

$$\delta_\pm = e^{\pm 2\pi i Q_z^d} \quad . \quad (2.129)$$

Using the complex form of the cosine, the kick in Eq. (2.125) can be split into left and right moving parts:

$$\begin{aligned} h_z^+(s > s_d, N) &= \\ R_{s-s_d} \left[R^N h_z^+(s_d) + \frac{iA_\theta \beta(s_d)}{2} \left\{ \sum_{T=0}^N R^T \delta_+^{N-T} + \sum_{T=0}^N R^T \delta_-^{N-T} \right\} \right] \quad . \end{aligned} \quad (2.130)$$

For the next simplification it shall be noted that

$$\sum_{i=0}^n x^i = \sum_{i=n}^0 x^i = \sum_{j=0}^n x^{n-j} \quad . \quad (2.131)$$

The first transformation is a simple exchange in summation limits. The second one arises from the change $i \rightarrow j = N - i$ and, thus, $j_0 = N - i_0 = 0$ and $j_1 = N - i_1 = 0$. Using this, the sums can be brought into the form of a geometric series

$$\begin{aligned} \sum_{T=0}^N R^T \delta_{\pm}^{N-T} &= \sum_{T=0}^N R^{N-T} \delta_{\pm}^T \\ &= R^N \sum_{T=0}^N (R^{-1} \delta_{\pm})^T \\ &= R^N \frac{1 - (R^{-1} \delta_{\pm})^{N+1}}{1 - R^{-1} \delta_{\pm}} \quad , \end{aligned} \quad (2.132)$$

and

$$\sum_{T=1}^N R^T \delta_{\pm}^{N-T} = R^N \frac{1 - (R^{-1} \delta_{\pm})^N}{1 - R^{-1} \delta_{\pm}} \quad . \quad (2.133)$$

The two cases of Eq. (2.125) differ only in one additional exponent of $R^{-1} \delta_{\pm}$ and it can be written compactly as

$$\begin{aligned} h_z^{\pm}(s, N) &= R_{s-s_d} R^N \left[h_z^{\pm}(s_d) \right. \\ &\quad + \frac{iA_{\theta} \beta(s_d)}{2} \frac{1 - (R^{-1} \delta_{+})^{N+\Theta(s, s_d)}}{1 - R^{-1} \delta_{+}} \\ &\quad \left. + \frac{iA_{\theta} \beta(s_d)}{2} \frac{1 - (R^{-1} \delta_{-})^{N+\Theta(s, s_d)}}{1 - R^{-1} \delta_{-}} \right] \quad . \end{aligned} \quad (2.134)$$

Furthermore, the terms $R \delta_{\pm}$ can be written out:

$$R^{-1} \delta_{\pm} = e^{2\pi i(Q_z \pm Q_z^d)} = e^{\pm 2\pi i Q_z^{\pm}} \quad , \quad (2.135)$$

and

$$1 - e^{2i\alpha} = -e^{i\alpha} 2i \sin \alpha \quad . \quad (2.136)$$

Those identities can be used to simplify the exponentials

$$\begin{aligned} h_z^{\pm}(s, N) &= R_{s-s_d} R^N \left[h_z^{\pm}(s_d) \right. \\ &\quad + \frac{A_{\theta} \beta(s_d)}{4} \frac{1 - e^{2\pi i Q_z^{\pm}(N+\Theta(s, s_d))}}{e^{i\pi Q_z^{\pm}} \sin(\pi Q_z^{\pm})} \\ &\quad \left. - \frac{A_{\theta} \beta(s_d)}{4} \frac{1 - e^{-2\pi i Q_z^{\mp}(N+\Theta(s, s_d))}}{e^{i\pi Q_z^{\mp}} \sin(\pi Q_z^{\mp})} \right] \quad . \end{aligned} \quad (2.137)$$

The term h_z^+ in Eq. (2.137) can be put into

$$\tilde{h}_z^+(s_d) \equiv h_z^+(s_d) + \left(\frac{A_\theta \beta(s_d)}{4 \sin(\pi Q_z^-)} \lambda_z e^{i\pi Q_z^-} - \frac{A_\theta \beta(s_d)}{4 \sin(\pi Q_z^+)} e^{-i\pi Q_z^+} \right) . \quad (2.138)$$

Now, the driven motion is separated off:

$$h_z^+(s, N) = R_{s-s_d} R^N \left[\tilde{h}_z(s_d) + \frac{A_\theta \beta(s_d)}{4 \sin(\pi Q_z^-)} e^{-\pi i Q_z^- (2N + 2\Theta(s, s_d) - 1)} - \frac{A_\theta \beta(s_d)}{4 \sin(\pi Q_z^+)} e^{\pi i Q_z^+ (2N + 2\Theta(s, s_d) - 1)} \right] . \quad (2.139)$$

and the linear rotation can be integrated into the terms:

$$h_z^+(s, N) = \tilde{h}_z(s, N) + \frac{A_\theta \beta(s_d)}{4 \sin(\pi Q_z^-)} e^{i[-2\pi N Q_z^- - \varphi_{s_d s} + \pi Q_z^- (2N + 2\Theta(s, s_d) - 1)]} - \frac{A_\theta \beta(s_d)}{4 \sin(\pi Q_z^+)} e^{i[2\pi N Q_z^+ - \varphi_{s_d s} - \pi Q_z^+ (2N + 2\Theta(s, s_d) - 1)]} . \quad (2.140)$$

Noting that

$$2\Theta(a) - 1 = \text{sgn}(a), \text{ if } a \neq 0 \quad , \quad (2.141)$$

Eq. (2.140) can be further simplified⁶:

$$h_z^+(s, N) = \tilde{h}_z(s, N) + \frac{A_\theta \beta(s_d)}{4 \sin(\pi Q_z^-)} e^{i[-2N\pi Q_z^- - \varphi_{s_d s} + \pi Q_z^- \text{sgn}(s-s_d)]} - \frac{A_\theta \beta(s_d)}{4 \sin(\pi Q_z^+)} e^{i[2N\pi Q_z^+ - \varphi_{s_d s} - \pi Q_z^+ \text{sgn}(s-s_d)]} . \quad (2.142)$$

The free motion of the beam is perturbed by two driving modes corresponding to the sum and difference of natural tune and driven tune. In most applications the ac-dipole strength is much greater than the free oscillation amplitude $A_\theta \beta(s_d) \gg |\tilde{h}_z(s, N)|$.

All derivations in this section have been made for h_z^+ . It shall be noted here that the nega-

⁶strictly speaking Eq. (2.142) is valid only for $s \neq s_d$ and one should carefully exclude this case in the following. But since a measurement at the exact position of the AC Dipole is not possible in the first place this fine detail will be ignored in this work.

tively turning coordinate h_z^- has the form

$$\begin{aligned}
h_z^-(s, N) = & \tilde{h}_z^-(s, N) \\
& + \frac{A_\theta \beta(s_d)}{4 \sin(\pi Q_z^-)} e^{i[2N\pi Q_z^- + \varphi_{s_d s} - \pi Q_z^- \text{sgn}(s-s_d)]} \\
& - \frac{A_\theta \beta(s_d)}{4 \sin(\pi Q_z^+)} e^{i[-2N\pi Q_z^+ + \varphi_{s_d s} + \pi Q_z^+ \text{sgn}(s-s_d)]} .
\end{aligned} \quad (2.143)$$

Subtracting the closed driven closed orbit \tilde{h}_z and with the definition

$$\lambda_z = \frac{\sin(\pi Q_z^-)}{\sin(\pi Q_z^+)} , \quad (2.144)$$

the driven motion can be rewritten in the form

$$\begin{aligned}
h_z^\pm(s, N) = & \frac{A_\theta \beta(s_d)}{4 \sin(\pi Q_z^\mp)} \left[e^{\pm i[-2N\pi Q_z^\mp - \varphi_{s_d s} + \pi Q_z^\mp \text{sgn}(s-s_d)]} \right. \\
& \left. - \lambda_z e^{\pm i[2N\pi Q_z^\mp - \varphi_{s_d s} - \pi Q_z^\mp \text{sgn}(s-s_d)]} \right] ,
\end{aligned} \quad (2.145)$$

which is used in other works [16, 17].

2.6.2 Compensation of linear parameters

This section briefly summarises the compensation of the driven motion for the optics parameters β , α and φ ⁷.

In an actual measurement the phase and amplitude are calculated from the Fourier analysis of the real signal.

$$\begin{aligned}
H(1, 0)^{\text{free}} &= \frac{1}{2} (H^+(1, 0)^{\text{free}} + H^-(1, 0)^{\text{free}}) \\
&= \sqrt{2J_z \beta} [e^{-i\varphi(s)} + e^{i\varphi(s)}]
\end{aligned} \quad (2.146)$$

for the free motion and

$$H(1, 0) = \frac{A_\theta \beta(s_d)}{4 \sin(\pi Q_z^-)} \left[e^{i[-\varphi_{s_d s} + \pi Q_z^- \text{sgn}(s_d s)]} - \lambda e^{i[\varphi_{s_d s} + \pi Q_z^+ \text{sgn}(s_d s)]} \right] \quad (2.147)$$

for the driven motion. For the next steps the following trigonometric reformulation is needed:

$$e^{i(\alpha+\beta)} - \lambda e^{i(\alpha-\beta)} = e^{i\alpha} (e^{i\beta} - \lambda e^{-i\beta}) . \quad (2.148)$$

The sum of two oscillations with the same frequency forms a single oscillation, so the

⁷[16] and Ryoichi Miyamoto, private communication, Feb. 2017

β term can be rewritten as

$$B = |B|e^{i\psi} \quad (2.149)$$

with

$$\begin{aligned} |B|^2 &= (e^{i\beta} - \lambda e^{-i\beta})(e^{-i\beta} - \lambda e^{i\beta}) = 1 + \lambda^2 - 2\lambda \cos 2\beta \\ \psi &= \text{atan} \frac{\text{Im}\{B\}}{\text{Re}\{B\}} = \text{atan} \left(\frac{1 + \lambda}{1 - \lambda} \tan \beta \right) . \end{aligned} \quad (2.150)$$

Now Eq. (2.147) can be put in this form by defining

$$\begin{aligned} \alpha &\equiv \pi Q_z^d \text{sgn}(s - s_d) \\ \beta &\equiv \pi Q_z \text{sgn}(s - s_d) - \varphi_{s_d s} \end{aligned} \quad (2.151)$$

This allows for $H(1, 0)$ to be rewritten

$$\begin{aligned} H(1, 0) &= \frac{A_0 \beta(s_d)}{4 \sin(\pi Q_z^-)} \sqrt{1 + \lambda^2 - 2\lambda \cos [2\varphi_{s_d s} - \pi Q_z \text{sgn}(s - s_d)]} \\ &\quad \times e^{i[\pi Q_z^d \text{sgn}(s - s_d) + \psi]} . \end{aligned} \quad (2.152)$$

Comparing to the free case, Eq. (2.146), the driven phase is defined as

$$\begin{aligned} \varphi_{s_d s}^d &= Q_z^d \text{sgn}(s - s_d) + \psi \\ &= Q_z^d \text{sgn}(s - s_d) + \text{atan} \left(\frac{1 + \lambda}{1 - \lambda} \tan (\varphi_{s_d s} - \pi Q_z \text{sgn}(s - s_d)) \right) \end{aligned} \quad (2.153)$$

which fullfils the symmetric property

$$(1 - \lambda) \tan (\varphi_{s_d s}^d - \pi Q_z^d \text{sgn}(s - s_d)) = (1 + \lambda) \tan (\varphi_{s_d s} - \pi Q_z \text{sgn}(s - s_d)) \quad (2.154)$$

In order to get the driven Twiss parameters α^d , β^d and γ^d , the same relation between them and the driven phase φ^d is imposed:

$$\frac{d\varphi^d}{ds} = \frac{1}{\beta^d} \quad (2.155)$$

Taking the derivative of Eq. (2.154) w.r.t. s yields

$$\frac{(1 - \lambda)\varphi'^d(s)}{\cos^2 [\varphi^d(s) - \pi Q_z^d \text{sgn}(s - s_d)]} = \frac{(1 + \lambda)\varphi'(s)}{\cos^2 [\varphi(s) - \pi Q_z \text{sgn}(s - s_d)]} , \quad (2.156)$$

where it is assumed that all phases are w.r.t. the position of the AC-dipole s_d and $f'(x)$ denotes the derivative of the function f with respect to x . Respectively, taking its square

yields

$$\frac{(1 - \lambda)}{\cos^2 [\varphi^d(s) - \pi Q_z^d \text{sgn}(s - s_d)]} + 2\lambda = \frac{(1 + \lambda)^2}{\cos^2 [\varphi(s) - \pi Q_z \text{sgn}(s - s_d)]} - 2\lambda \quad . \quad (2.157)$$

Both equations can be used to cancel $\cos [\varphi^d(s) - \pi Q_z^d \text{sgn}(s - s_d)]$:

$$\frac{1}{\varphi'^d(s)} = \frac{1 + \lambda^2 - 2\lambda \cos [2\varphi(s) - 2\pi Q_z \text{sgn}(s - s_d)]}{1 - \lambda^2} \frac{1}{\varphi'(s)} \quad (2.158)$$

which, finally, is the formula to compute the driven β function:

$$\beta^d(s) = \frac{1 + \lambda^2 - 2\lambda \cos [2\varphi(s) - 2\pi Q_z \text{sgn}(s - s_d)]}{1 - \lambda^2} \beta(s) \quad (2.159)$$

The driven α function follows from the definition of the free α function:

$$\begin{aligned} \alpha^d(s) &= \frac{1}{2} \frac{d\beta^d}{ds} \\ &= \frac{1 + \lambda^2 - 2\lambda \cos [2\varphi(s) - 2\pi Q_z \text{sgn}(s - s_d)]}{1 - \lambda^2} \alpha(s) \\ &\quad - 2\lambda \sin [2\varphi(s) - 2\pi Q_z \text{sgn}(s - s_d)] \end{aligned} \quad (2.160)$$

Comparing the amplitude of the driven motion Eq. (2.152) with the amplitude of Eq. (2.146) the driven action J_x^d can be deduced:

$$\begin{aligned} \sqrt{2J_z^d \beta_z^d(s)} &= \frac{A_\theta \sqrt{\beta(s_d) \beta(s)}}{4 \sin(\pi Q_z^-)} \sqrt{1 + \lambda^2 - 2\lambda \cos [2\varphi_{s_d s} - \pi Q_z \text{sgn}(s - s_d)]} \\ \Rightarrow J_z^d &= \frac{A_\theta^2 \beta(s_d) (1 - \lambda^2)}{32 \sin^2(\pi Q_z^-)} \quad . \end{aligned} \quad (2.161)$$

The expressions for the driven optics parameters β^d , α^d , φ^d and J^d derived in this section can be used to compensate for the effect of the driven motion on the measurement and enable an easy measurement leveraging the advantages of an AC-dipole for optics measurements in circular accelerators.

CHAPTER 3

THE ANALYTICAL N-BPM METHOD

One of the most important figures of merit of optics correction is the deviation of the real β function from the model values, the β beating. A deviation from the ideal values has a negative effect on machine performance. Too high β beating can even put machine components in danger and a threshold for operation with physics filling scheme has to be imposed for machine protection reasons.

Furthermore, large β beating deteriorates other linear and especially non-linear optics measurements and correction methods. Therefore a good control of the β beating can be essential for higher-order correction steps.

This chapter summarises classical β beating methods from turn-by-turn data in section 3.1 and describes in detail a new algorithm, the analytical N-BPM method, which improves speed and performance by calculating analytically the error propagation in sections 3.3 through 3.4. Accuracy and precision of the new method are assessed using simulations of current LHC optics and design optics for the High-Luminosity upgrade of the LHC in sections 3.5 and 3.6.

With the exception of the first two sections, which set the context of the present study and introduce the mathematical tools, this chapter represents original work.

The content of this chapter has been published in [39].

3.1 β function measurement from turn-by-turn data

3.1.1 Three BPM method

The classical method to measure the β function in hadron machines is the *Three BPM Method* introduced in section 2.5.1.

With this method one can use the phase advance between three BPMs i, j, k to calculate the β function of the probed BPM i . It is a model dependent approach, the greater the difference between the model and the real accelerator the less accurate will be the result. A good knowledge of the actual accelerator is crucial for this approach to work.

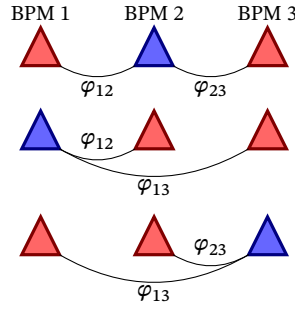


Figure 3.1: A sketch of the three BPM method. The probed BPM is shown in blue. For LHC arcs the combination with the probed BPM in the center is the most stable against phase measurement errors.

Equation (2.94) has been developed for LEP and it has been used for optics measurements in LEP and LHC during run I. But it has two shortcomings: it assumes that the actual β beating is very low and it diverges for phase advances close to $n\pi$, $n \in \mathbb{N}$. The latter makes measurements at exact $n\pi$ phase advances impossible and strongly enhances phase measurement errors near $n\pi$. Unfortunately, especially in the IR phase advances are very small and precise β function measurements are not feasible.

Figure 3.1 displays a sketch of the Three BPM Method. The probed BPM is shown in blue, BPMs j and k are shown in red. Classically the arithmetic mean of all three adjacent cases – as shown in the figure – were used.

In LHC arcs where the phase advance between adjacent BPMs is around 45° the combination with the probed BPM in the center yields almost optimal results since the perturbation from phase measurement errors is small for the occurring phase advances. The two other cases shown in Fig. 3.1 on the other hand include the phase advance $\varphi_{13} = 90^\circ$ which is less optimal.

In LHC interaction regions the phase advance between consecutive BPMs does not follow the same constraints as in the arc and values different from 45° may appear. In the final focus quadrupoles the β function peaks are very high to deliver a strong focusing of the beams in the interaction point¹. This yields a very small phase advance in this area, rendering a β measurement from phase impossible. At the same time a high precision of β beating is necessary to control β^* and to optimise the aperture.

3.1.2 Original N-BPM method

To avoid cases with unsuitable phase advances or to get the optimal phase advances, BPMs can be skipped. For an LHC arc a combination as shown in Fig. 3.2 can be used for the non-center cases of the Three BPM method in order to have the least uncertainties in all

¹cf. Fig. 2.3

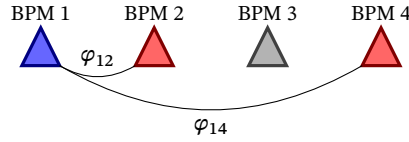


Figure 3.2: In the LHC arcs skipping one BPM for the non-center cases of the Three BPM Method is of advantage since the phase advance φ_{14} is more suitable regarding error propagation.

three combinations.

A second tool that can be applied to reduce uncertainty is averaging over more combinations which improves statistics and reduces statistical uncertainties. Unfortunately, systematic errors increase as more and more BPMs are skipped because of the presence of other elements with their imperfections in between the BPMs. In order to further improve the precision the information about statistical and systematic uncertainties can be used to calculate a weighted mean:

$$\beta(s_i) = \sum_l \beta_l(s_i) g_l \quad (3.1)$$

$$\beta_l(s_i) = \frac{\cot \varphi_{ij_l} - \cot \varphi_{ik_l}}{\cot \varphi_{ij_l}^m - \cot \varphi_{ik_l}^m} \beta(s_i)^m, \quad (3.2)$$

with the weights g_l satisfying

$$\sum_l g_l = 1, \quad (3.3)$$

and j_l, k_l pairs of BPMs around the probed BPM.

Furthermore the β function values calculated from different combinations are not statistically independent and correlation has to be taken into account when calculating the weights. The N-BPM method [40, 41] was developed to implement this feature. It was successfully used in the LHC during run II and for the re-analysis of run I data as well as in the storage rings of ALBA and ESRF.

The name originates in the fact that the BPMs i, j_l and k_l are taken in a range of N BPMs. This generates $n = (N - 2)(N - 1)/2$ combinations.

3.2 Generalised least squares

To get the correct estimate for the weights g_l the study of some statistics is in order. The weights can be determined using a least-squares optimisation. The weighted mean Eq. (3.1)

can be rewritten in vector notation:

$$\vec{\beta} = \mathbf{B}\vec{\gamma} \quad (3.4)$$

$$\vec{\beta} = \begin{pmatrix} \hat{\beta} \\ \vdots \\ \hat{\beta} \end{pmatrix}, \quad \vec{\gamma} = \begin{pmatrix} g_1 \\ \vdots \\ g_n \end{pmatrix}, \quad \mathbf{B} = \begin{pmatrix} \vec{\beta}^T \\ \vdots \\ \vec{\beta}^T \end{pmatrix}, \quad (3.5)$$

where each line of the equation system is just the same. The difference between measurement l and the mean value $\hat{\beta}$ is denoted by ϵ_l :

$$\vec{\epsilon} = \vec{\beta} - \vec{\beta} \quad (3.6)$$

The least square minimisation seeks a set of weights g_i for which the squared errors are minimal. Since the different β_i are correlated and have a covariance matrix $\mathbf{Cov}[\vec{\beta}] \neq \mathbf{diag}(\sigma_1^2, \dots, \sigma_n^2)$ the theory of generalised least-squares estimation [42] has to be applied.

The *covariance matrix* of a set of random variables Ω_i is defined as

$$\begin{aligned} \mathbf{Cov}[\vec{\Omega}] &= \mathbf{E}[(\vec{\Omega} - E[\vec{\Omega}])(\vec{\Omega} - E[\vec{\Omega}])^T] \\ &= \mathbf{E}[\vec{\Omega}\vec{\Omega}^T] - E[\vec{\Omega}]E[\vec{\Omega}]^T, \end{aligned} \quad (3.7)$$

where $E[\vec{\Omega}]$ is the *expected value* of the random variables $\vec{\Omega}$. And the notation is chosen such that the expected value of a vector is a vector of expected values of each component and similar for matrices.

Equation (3.7) can be expressed element-wise:

$$(\mathbf{Cov}[\vec{\Omega}])_{ij} = E[\Omega_i\Omega_j] - E[\Omega_i]E[\Omega_j] \quad (3.8)$$

3.2.1 Error Propagation

Consider a set of unperturbed phase measurements $\{\varphi_1, \dots, \varphi_n\}$ and non-observable parameters $\{K_{1,1}, \dots, K_{1,m}, s_1, \dots, s_\nu, x_1, \dots, x_\mu\}$ with corresponding errors $\Delta\varphi_\alpha, \Delta K_{1,\beta}, \Delta s_\gamma, \Delta x_\kappa$. Collecting all parameters into a vector

$$\vec{\Omega}_0 = \begin{pmatrix} \vec{\varphi} \\ \vec{K} \\ \vec{s} \\ \vec{x} \end{pmatrix}, \quad \Delta\vec{\Omega} = \begin{pmatrix} \Delta\varphi \\ \Delta\vec{K} \\ \Delta\vec{s} \\ \Delta\vec{x} \end{pmatrix}. \quad (3.9)$$

Using a Taylor expansion the errors in these parameters can be propagated

$$\beta_l(\vec{\Omega}) = \beta_l(\vec{\Omega}_0) + \partial^i \beta_l(\vec{\Omega}_0) \Delta \Omega_i + \partial^i \partial^j \beta_l(\vec{\Omega}_0) \Delta \Omega_i \Delta \Omega_j + O(\Delta \Omega^3), \quad (3.10)$$

where the Einstein summation convention is used and the derivatives are w.r.t. Ω_i : $\partial^i \beta_l \equiv \frac{\partial \beta_l}{\partial \Omega_i}$. The argument $(\vec{\Omega}_0)$ is omitted in the following for the β function and its derivatives at the unperturbed position $\vec{\Omega}_0$. For the calculation of the covariance matrix, Eq. (3.10) is truncated to second order and for convenience and readability, the two summands of Eq. (3.8) are derived separately.

$$E[\beta_l(\vec{\Omega})] \approx E[\beta_l + \partial^i \beta_l \Delta \Omega_i + \partial^i \partial^j \beta_l \Delta \Omega_i \Delta \Omega_j] = \beta_l + \partial^i \beta_l E[\Delta \Omega_i] + \partial^i \partial^j \beta_l E[\Delta \Omega_i \Delta \Omega_j]. \quad (3.11)$$

It is assumed that there are no systematic errors in the measurement instruments and so $E[\Delta \Omega_i] = 0$ and the middle term vanishes. One can conclude

$$E[\beta_l(\vec{\Omega})]E[\beta_m(\vec{\Omega})] \approx \beta_l \beta_m + (\beta_l \partial^i \partial^j \beta_m + \beta_m \partial^i \partial^j \beta_l) E[\Delta \Omega_i \Delta \Omega_j], \quad (3.12)$$

where terms proportional to the square of the variance go into the reminder $O(\Delta \Omega^3)$.

To calculate the term $E[\beta_l \beta_m]$ more steps are needed:

$$\begin{aligned} E[\beta_l(\vec{\Omega})\beta_m(\vec{\Omega})] &= E[(\beta_l + \partial^i \beta_l \Delta \Omega_i + \partial^i \partial^j \beta_l \Delta \Omega_i \Delta \Omega_j)(\beta_m + \partial^i \beta_m \Delta \Omega_i + \partial^i \partial^j \beta_m \Delta \Omega_i \Delta \Omega_j)] \\ &\approx E[\beta_l \beta_m + (\beta_l \partial^i \beta_m + \beta_m \partial^i \beta_l) \Delta \Omega_i + \partial^i \beta_l \partial^j \beta_m \Delta \Omega_i \Delta \Omega_j + \\ &\quad (\beta_l \partial^i \partial^j \beta_m + \beta_m \partial^i \partial^j \beta_l) \Delta \Omega_i \Delta \Omega_j] \\ &= \beta_l \beta_m + \partial^i \beta_l \partial^j \beta_m E[\Delta \Omega_i \Delta \Omega_j] + (\beta_l \partial^i \partial^j \beta_m + \beta_m \partial^i \partial^j \beta_l) E[\Delta \Omega_i \Delta \Omega_j]. \end{aligned} \quad (3.13)$$

Finally, subtracting Eq. (3.12) from Eq. (3.13), yields

$$(\text{Cov}[\vec{\beta}])_{lm} = \partial^i \beta_l \partial^j \beta_m E[\Delta \Omega_i \Delta \Omega_j] = \partial^i \beta_l \partial^j \beta_m \text{Cov}[\vec{\Delta \Omega}]_{ij}. \quad (3.14)$$

In the last step again the assumption $E(\Delta \Omega_i) = 0$ is made, implying

$$\text{Cov}[\vec{\Delta \Omega}]_{ij} = E[\Delta \Omega_i] E[\Delta \Omega_j] - E[\Delta \Omega_i \Delta \Omega_j] = E[\Delta \Omega_i \Delta \Omega_j]. \quad (3.15)$$

In matrix notation Eq. (3.14) reads

$$\mathbf{Cov}[\vec{\beta}] = \mathbf{T} \mathbf{Cov}[\vec{\Delta \Omega}] \mathbf{T}^T, \quad (3.16)$$

where

$$T_{ij} = \frac{\partial \beta_i}{\partial \Omega_j}. \quad (3.17)$$

If the parameters $\vec{\Omega}$ are uncorrelated, the covariance matrix of $\Delta\vec{\Omega}$ simplifies to

$$(\text{Cov}[\Delta\vec{\Omega}])_{ij} = 0 \quad \text{if } i \neq j, \quad (3.18)$$

$$(\text{Cov}[\Delta\vec{\Omega}])_{ii} = \sigma_i^2, \quad (3.19)$$

$$\Rightarrow E[\Delta\Omega_i \Delta\Omega_j] = E[\Delta\Omega_i] E[\Delta\Omega_j] \quad \text{if } i \neq j, \quad (3.20)$$

and Eq. (3.14) reads

$$(\text{Cov}[\vec{\beta}])_{lm} = \partial^l \beta_l \partial^m \beta_m E[\Delta\Omega_l^2] = \partial^l \beta_l \partial^m \beta_m \sigma_l^2, \quad (3.21)$$

with the variance being defined by

$$\sigma_i^2 = E[\Delta\Omega_i^2] \quad . \quad (3.22)$$

3.2.2 The generalised least-squares estimator

After computing the covariance matrix of β , the generalised least-squares estimator can be calculated by solving the translated system

$$\mathbf{X}^{-1} \vec{\beta} = \mathbf{X}^{-1} \mathbf{B} \vec{\gamma} + \mathbf{X}^{-1} \vec{\epsilon} \quad (3.23)$$

where the translation \mathbf{X} is such that $\mathbf{X}^T \mathbf{X} = \mathbf{V} = \mathbf{Cov}[\vec{\beta}]$. The least-squares estimation searches for a minimum of

$$\|\mathbf{X}^{-1} (\vec{\beta} - \mathbf{B} \vec{\gamma})\|^2 = (\vec{\beta} - \mathbf{B} \vec{\gamma})^T \mathbf{V}^{-1} (\vec{\beta} - \mathbf{B} \vec{\gamma}) \quad (3.24)$$

Eq. (3.24) can be solved in the index notation:

$$\begin{aligned} \frac{\partial}{\partial g_k} \sum_{i,j} \left(\beta_i - \sum_l \beta_l g_l \right) V_{ij}^{-1} \left(\beta_j - \sum_m \beta_m g_m \right) &= 2 \sum_{i,j} \beta_k V_{ij}^{-1} \left(\beta_j - \sum_m \beta_m g_m \right) = 0 \\ \Rightarrow \sum_{i,j} V_{ij}^{-1} \beta_j &= \sum_{i,j} V_{ij}^{-1} \sum_m \beta_m g_m \\ \Rightarrow \sum_m g_m \beta_m &= \frac{\sum_{i,j} V_{ij}^{-1} \beta_j}{\sum_{i,j} V_{ij}^{-1}} = \sum_m \frac{\sum_i V_{im}^{-1}}{\sum_{i,j} V_{ij}^{-1}} \beta_m \end{aligned} \quad (3.25)$$

where the summation index can be renamed in the numerator to highlight a solution of the system:

$$\mathbf{g}_i(\mathbf{V}) = \frac{\sum_k V_{ik}^{-1}}{\sum_{j,k} V_{jk}^{-1}} . \quad (3.26)$$

The uncertainty of the weighted average is then

$$\sigma^2(\mathbf{X}^{-1}\vec{\beta}) = \vec{g}^T \mathbf{V} \vec{g} = \sum_{i,j} g_i V_{ij} g_j . \quad (3.27)$$

3.2.3 Error matrix for N-BPM method

The error matrix \mathbf{V} can be obtained from the single variances by

$$\mathbf{V} = \mathbf{T} \mathbf{M} \mathbf{T}^{-1} , \quad (3.28)$$

where $\mathbf{M} = \text{diag}(\sigma_{\varphi_1}^2, \dots, \sigma_{\varphi_n}^2)$ is a diagonal matrix consisting of the variances of the phases and \mathbf{T} is the Jacobian matrix

$$T_{i\lambda}(s_i) = \left. \frac{\partial \beta_i(s_i)}{\partial \varphi_\lambda} \right|_{\delta\varphi=0} , \quad (3.29)$$

$\delta\varphi = 0$ meaning that the derivatives are evaluated with all phase advance errors set to zero. The correlation of statistical errors (coming from BPM noise) is

$$T_{i\lambda}^\varphi(s_i) = \left. \frac{\partial \beta_i(s_i)}{\partial \varphi_\lambda} \right|_{\delta\varphi=0} = \frac{(\delta_i^\lambda - \delta_{j_l}^\lambda) \sin^{-2} \varphi_{i j_l}^m - (\delta_i^\lambda - \delta_{k_l}^\lambda) \sin^{-2} \varphi_{i k_l}^m}{\cot \varphi_{i j_l}^m - \cot \varphi_{i k_l}^m} \beta^m(s_i) . \quad (3.30)$$

A superscript φ is placed here intentionally to highlight that the \mathbf{T} matrix only includes statistical errors coming from the uncertainty of the phase measurement. δ_β^α denotes the Kronecker δ . Including systematic errors, the total error matrix is

$$\mathbf{V} = \mathbf{V}_{\text{stat}} + \mathbf{V}_{\text{syst}} , \quad (3.31)$$

where $\mathbf{V}_{\text{stat}} = \mathbf{T}^\varphi \mathbf{M} \mathbf{T}^{\varphi^{-1}}$ and the total uncertainty of the averaged $\hat{\beta}$ is then given by

$$\sigma_\beta^2 = \sigma_{\text{stat}}^2 + \sigma_{\text{syst}}^2 . \quad (3.32)$$

3.2.4 Extension of the N-BPM method

In the existing numerical N-BPM method only the statistical errors are calculated analytically while \mathbf{V}_{sys} and hence σ_{sys}^2 are evaluated from Monte Carlo simulations of lattices with errors. For that the statistics over many simulations is gathered. Even with a highly parallelised code on a multicore machine this procedure takes about 1 hour for a “fast” set of 1000 simulations. Since the computation time scales linearly with the number of simulations, this can take up to 10 hours for 10^4 simulations which were used in the post processing of a measurement.

In this thesis a new method is introduced that calculates also the systematic errors analytically. On the same computer the analytical N-BPM method takes only 30 seconds to compute the β function for more than 500 BPMs whereas the N-BPM method takes about one hour. It provides a fully analytical calculation of the uncertainties while the precision of the original method depends on the number of simulations. Any source of uncertainties can be taken into account if its analytical expression is known. The method does not depend on the stability of the lattice whereas the Monte Carlo simulations fail if, for some combinations of errors, no closed orbit can be found. This is a limiting factor when the N-BPM method is used for pushed optics with very low β^* like the HL-LHC.

3.3 Corrected β from phase formula

Equation (2.94) assumes that no error is present in the region between the involved BPMs. A new formula has been developed in [34] that takes quadrupolar errors into account,

$$\beta(s_1) = \frac{\cot \varphi_{12} - \cot \varphi_{13}}{\cot \varphi_{12}^m - \cot \varphi_{13}^m + \bar{h}_{12} - \bar{h}_{13}} \beta^m(s_1) + O(\delta K_1^2) \quad , \quad (3.33)$$

with

$$\bar{h}_{ij} = \frac{\sum_{i < w < j} \beta_w^m \delta K_{w,1} \sin^2 \varphi_{wj}^m}{\sin^2 \varphi_{ij}^m} \quad . \quad (3.34)$$

The sum runs over all elements w between BPMs i and j . $\delta K_{w,1}$ is the integrated quadrupolar field error of element w . The definition of K_n follows the MAD [43] convention. Note that Eq. (3.34) is only defined for the case $s_1 < s_2 < s_3$ i.e. the β function is calculated at the position of the first BPM. Since we want to use as many BPM combinations as possible we will derive below a form of Eq. (3.33) without this constraint.

In [34] the quality of Eq. (3.33) has been assessed for the ESRF storage ring by simulating a lattice with errors and comparing the results of Eq. (3.33) to the beta beating of the simulated lattice. In this paper the same study is repeated for the LHC and its future upgrade

element	σ_K/K_1 [10^{-4}]	σ_s [mm]	σ_x [mm]
MQ	18	1.0	
MQM	12	1.0	-
MQY	11	1.0	-
MQX	4	6.0	-
MQW	15	1.0	-
MQT	75	1.0	-
MS	-	-	0.3
BPM	-	1.0	-

Table 3.1: Estimates for the LHC gradient and misalignment errors. MQ are focusing and defocusing quadrupoles, MS are sextupoles. The values of the magnet errors are derived from magnetic measurements of [44, 45].

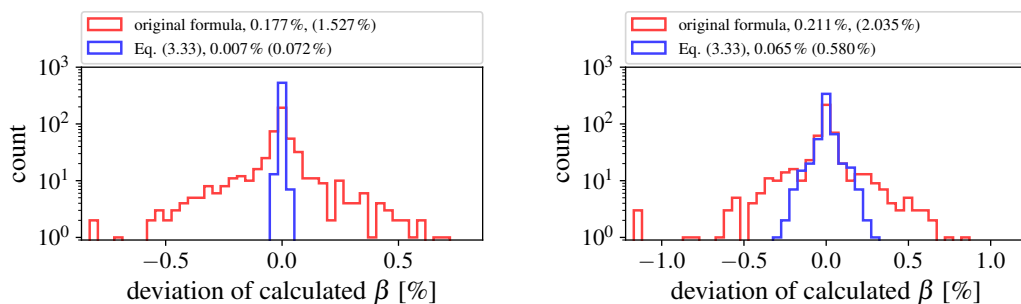


Figure 3.3: Left: Difference between the real (simulated) horizontal β -functions and the ones calculated by Eq. (2.94) in red and (3.33) in blue, respectively. Data are from MADX simulations of a lattice with quadrupolar errors only. Right: The same quantities are evaluated for the case with additional magnet misalignments. The numbers which figure after the legend label show the root mean square of the deviation and the the peak-to-peak derivation in parenthesis.

the HL-LHC. Table 3.1 summarises those uncertainty estimates for the LHC elements that are relevant for this study. In Figure 3.3 a comparison between Eqs. (2.94) and (3.33) is shown in the horizontal plane. The plot shows a histogram of the deviation of the two formulae from the real (i.e. simulated) β function values. The histogram contains the values of all the individual BPMs for one simulated lattice. The left plot shows the case with only quadrupolar field errors whereas in the right plot also misalignment errors were included in the lattice. The introduction of errors not taken into account in Eq. (3.34) deteriorates the result. However Eq. (3.33) still yields a clearly better estimate.

Moreover Eq. (3.33) may be easily modified for taking into account a more realistic set of errors – quadrupolar field errors as well as sextupole transverse misalignments, quadrupole longitudinal misalignments and BPM longitudinal displacements.

While the magnet misalignment errors can be approximated as *effective* quadrupolar field errors and integrated in Eq. (3.34) the BPM misalignments need a different approach as

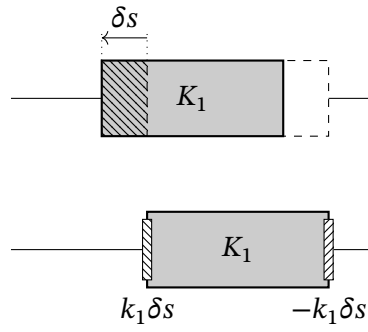


Figure 3.4: The top sketch shows the displaced quadrupole (solid gray) relative to the original position (dashed). In the bottom sketch one can see the quadrupole at its original position with thin magnets on both ends.

shown in the next paragraph.

3.3.1 Effect of transverse sextupole misalignments

The magnetic field of a sextupole displaced horizontally by Δx reads

$$B_y = \frac{B}{2}((x + \Delta x)^2 - y^2) \quad . \quad (3.35)$$

This induces a quadrupolar field error whose strength δK_1 is

$$\delta K_1 = \frac{1}{B_0 \rho_0} \left. \frac{\partial B_y}{\partial x} \right|_{x=y=0} = \frac{B}{B_0 \rho_0} \Delta x \quad . \quad (3.36)$$

This term can be used in Eq. (3.34) to include sextupole offsets in \bar{h}_{ij} .

3.3.2 Effect of longitudinal quadrupole misalignments

The effect of a longitudinal displacement δs of a quadrupole magnet can be approximated by leaving the magnet at its original position and introducing two thin magnets at its edges to mimic the displacement, as shown in Figure 3.4. The top part of the figure shows the actual situation: The quadrupole is moved to the left such that it covers now the hatched area in addition to the gray region. The bottom part illustrates the approximation method: In the direction of the displacement there is an additional element with integrated field strength $\delta K_1 = k_1 \delta s$ (k_1 being the non-integrated quadrupole strength), to simulate the part of the quadrupole that moved into this area whereas an error $-\delta K_1$ is placed at the opposite end to compensate the part of the quadrupole that moved out of this area.

3.3.3 Effect of BPM misalignments

An error, δs_i , in the longitudinal position of a BPM affects the evaluation of Eq. (3.33) and Eq. (3.34) which rely on the model values of β and φ at the nominal position of the BPM. Using Eq. (2.7) the phase error and the resulting β shift at the position $s_i + \delta s_i$ can be approximated as

$$\tilde{\varphi}_i \approx \varphi_i + \frac{1}{\beta_i} \delta s_i \quad , \quad (3.37)$$

$$\tilde{\beta}_i \approx \beta_i + \frac{\partial \beta_i}{\partial s} \delta s_i = \beta_i - 2\alpha_i \delta s_i \quad , \quad (3.38)$$

up to first order in δs_i .

3.3.4 Derivation of a corrected β from phase formula

An equation similar to Eq. (3.33) has to be re-derived by taking into account the considerations of the preceding sections.

First, focusing errors, Eq. (2.87), and BPM misalignments, Eq. (3.37), are incorporated in the phase advance φ_{ij} :

$$\begin{aligned} \varphi_{ij}^{\text{err}} &= \varphi_{ij}^m + \bar{h}_{ij} - 8 \sin^2 \varphi_{ij}^m \mathcal{R}e\{f_i\} - 8 \sin \varphi_{ij}^m \cos \varphi_{ij}^m \mathcal{I}m\{f_i\} + \frac{1}{\beta_j^m} \delta s_j - \frac{1}{\beta_i^m} \delta s_i \\ &= \varphi_{ij}^m + \Delta \varphi_{ij} \quad . \end{aligned} \quad (3.39)$$

Together with the β shift of Eq. (3.38), the β beating Eq. (2.77) and the α beating, the quotient of the first row elements of the transfer matrix, Eq. (2.92), reads

$$\frac{(m_{ij})_{11}}{(m_{ij})_{12}} = \frac{1}{(\beta_i^m - 2\alpha_i^m \delta s_i)(1 - 8\mathcal{I}m\{f_i\})} \left(\cot \varphi_{ij}^{\text{err}} + \alpha_i(1 - 8\mathcal{I}m\{f_i\} - 8\mathcal{R}e\{f_i\})^m \right) \quad . \quad (3.40)$$

The cotangent above can be expanded in a Taylor series around φ_{ij}^m :

$$\cot \varphi_{ij}^{\text{err}} = \cot \varphi_{ij}^m (1 - 8\mathcal{I}m\{f_i\}) + \frac{\bar{h}_{ij}}{\sin^2 \varphi_{ij}^m} - 8\mathcal{R}e\{f_i\} + \frac{\frac{1}{\beta_i^m} \delta s_i + \frac{1}{\beta_j^m} \delta s_j}{\sin^2 \varphi_{ij}^m} \quad (3.41)$$

and Eq. (3.40) can be simplified:

$$\frac{(m_{ij})_{11}}{(m_{ij})_{12}} = \frac{1}{\beta_i^m - 2\alpha_i^m \delta s_i} \left(\cot \varphi_{ij}^{\text{err}} + \alpha_i^m + \bar{g}_{ij} \right) \quad (3.42)$$

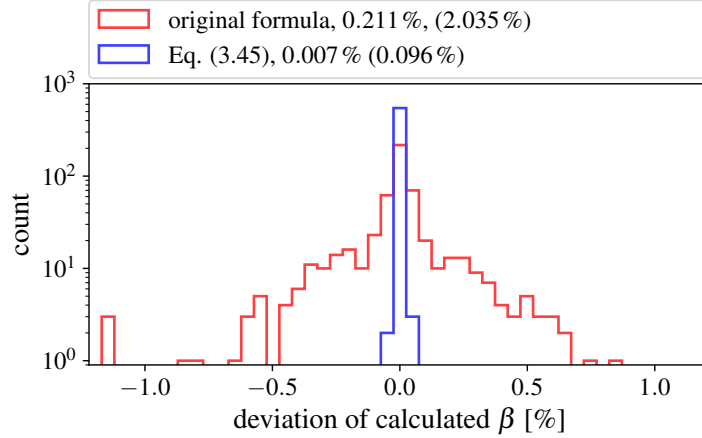


Figure 3.5: Accuracy of the horizontal β -function evaluated via Eq. (2.94) and Eq. (3.45) with the effect of magnets and BPM misalignments taken into account. The accuracy of Eq. (3.45) is similar to the one of Eq. (3.33) with quadrupolar field errors only (Figure 3.3).

with

$$\bar{g}_{ij} = \text{sgn}(i - j) \frac{\frac{1}{\beta^m(s_j)} \delta s_j - \frac{1}{\beta^m(s_i)} \delta s_i + \sum_{w \in I} \beta_w^m \delta K_{w,1} \sin^2 \varphi_{wj}^m}{\sin^2 \varphi_{ij}^m}, \quad (3.43)$$

To get the corrected β from phase formula one has to follow the same steps as in section 2.5.1:

$$\frac{(m_{ij})_{11}}{(m_{ij})_{12}} - \frac{(m_{ik})_{11}}{(m_{ik})_{12}} = \frac{1}{\beta_i} (\cot \varphi_{ij} - \cot \varphi_{ik}) - \frac{1}{(\beta_i^m - 2\alpha_i^m)} \times [\cot \varphi_{ij}^m + \bar{g}_{ij} - \cot \varphi_{ik}^m - \bar{g}_{ik}] \quad (3.44)$$

and the final expression for the β function at position s_i from the combination l reads

$$\beta_l(s_i) \approx \frac{\cot \varphi_{ij_l} - \cot \varphi_{ik_l}}{\cot \varphi_{ij_l}^m - \cot \varphi_{ik_l}^m + \bar{g}_{ij_l} - \bar{g}_{ik_l}} [\beta^m(s_i) - 2\alpha^m(s_i) \delta s_i] \quad (3.45)$$

In order to account for sextupole misalignments and quadrupole longitudinal misalignments, it suffices to add the corresponding effective δK_1 to the sum in \bar{g}_{ij} , as described in the previous sections. The set I is defined in Eq. (2.82), so that an element with index $w \in I$ lies between elements i and j and Eqs (3.45) and (3.43) hold for every BPM combination i, j, k . By doing so, we do not need to distinguish the three cases where the probed BPM is in the middle, left or right.

All these considerations can be put into Eq. (3.45) and used to get a more accurate β function. To verify the validity of Eq. (3.45), its horizontal β -functions are compared to the ones simulated by MADX along with the ones inferred from Eq. (2.94), this time including

sextupole radial offsets and BPMs longitudinal shifts.

The result is shown in Figure 3.5. The accuracy is now as good as the one of Eq. (3.33) when only quadrupolar field errors were introduced in the lattice, which in turn is much greater than the old formula, Eq. (2.94).

3.4 Calculation of the correlation matrix

The Jacobian \mathbf{T} of Eq. (3.29) can be split into blocks

$$\mathbf{T} = (\mathbf{T}^\varphi \quad \mathbf{T}^K \quad \mathbf{T}^s), \quad (3.46)$$

for the uncertainties of phase \mathbf{T}^φ , quadrupole field \mathbf{T}^K and BPM misalignment \mathbf{T}^s . \mathbf{T}^φ is the same of Eq. (3.30). For the quadrupolar field errors we get

$$T_{i\lambda}^K(s_i) = \left. \frac{\partial \beta_l(s_i)}{\partial K_{1,\lambda}} \right|_{\delta K=0} = \mp \frac{\beta^m(s_i)\beta^m(s_\lambda)}{\cot \varphi_{ij_l}^m - \cot \varphi_{ik_l}^m} \left(\frac{\sin^2 \varphi_{\lambda j_l}^m}{\sin^2 \varphi_{ij_l}^m} A_{ij_l}(\lambda) - \frac{\sin^2 \varphi_{\lambda k_l}^m}{\sin^2 \varphi_{ik_l}^m} A_{jk_l}(\lambda) \right), \quad (3.47)$$

with

$$A_{ij}(\lambda) = \begin{cases} 1 & \text{if } i < \lambda < j \\ -1 & \text{if } j < \lambda < i \\ 0 & \text{else} \end{cases}. \quad (3.48)$$

The contribution from the BPM misalignment is calculated analogously:

$$\begin{aligned} T_{i\lambda}^s(s_i) &= \left. \frac{\partial \beta_l(s_i)}{\partial s_\lambda} \right|_{\delta s=0} \\ &= -2\alpha^m(s_i)\delta_i^\lambda \mp \frac{\frac{\text{sgn}(i-j)}{\sin^2 \varphi_{ij_l}^m} \left(\frac{\beta^m(s_i)}{\beta^m(s_{j_l})} \delta_\lambda^{j_l} - \delta_\lambda^i \right) - \frac{\text{sgn}(i-k_l)}{\sin^2 \varphi_{ik_l}^m} \left(\frac{\beta^m(s_i)}{\beta^m(s_{k_l})} \delta_\lambda^{k_l} - \delta_\lambda^i \right)}{\cot \varphi_{ij_l}^m - \cot \varphi_{ik_l}^m}. \end{aligned} \quad (3.49)$$

In Eq. (3.47) and Eq. (3.49) the minus and plus signs refer to the horizontal and vertical case, respectively.

3.5 Removal of bad BPM combinations

Since a phase advance $\varphi_{ij} \approx n\pi$ results in an enhancement of phase measurement errors and in the extreme case numerically unstable values, a filtering was introduced. Instead of keeping a constant number of combinations as in [40] we set a threshold for *bad* phase

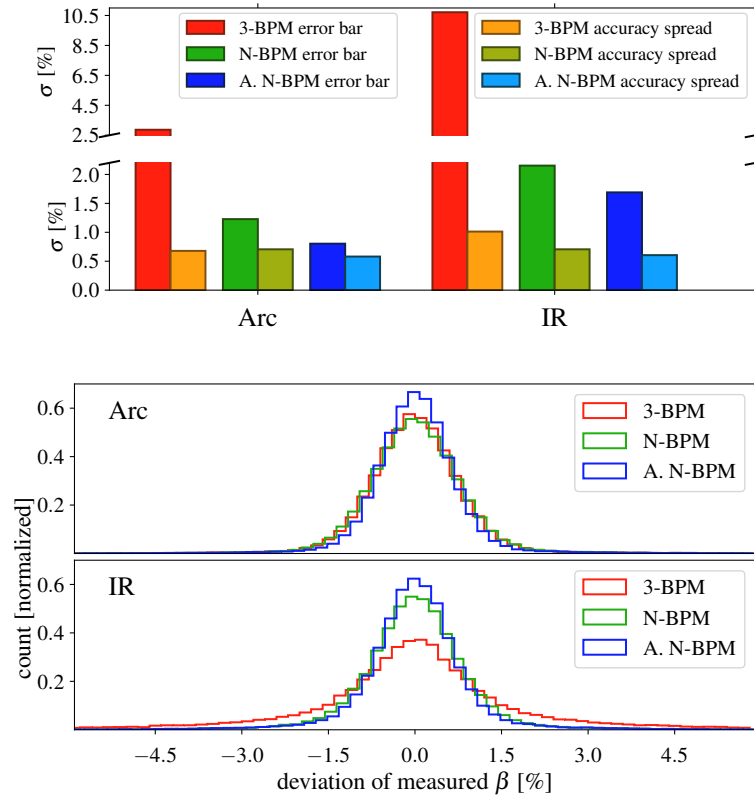


Figure 3.6: Comparison of the 3-BPM method, the original N-BPM method and the analytical N-BPM method (denoted as A.N-BPM) for the nominal LHC lattice at collision, with $\beta^* = 40$ cm. BOTTOM: histogram of the difference to the real β -function in percent. TOP: the average of the error bars and the accuracy spread (width of a standard distribution fit to the distribution in the bottom plot) in percent. The analytical N-BPM method has the best accuracy both in the arcs and in the IRs. Data have been cleaned of outliers.

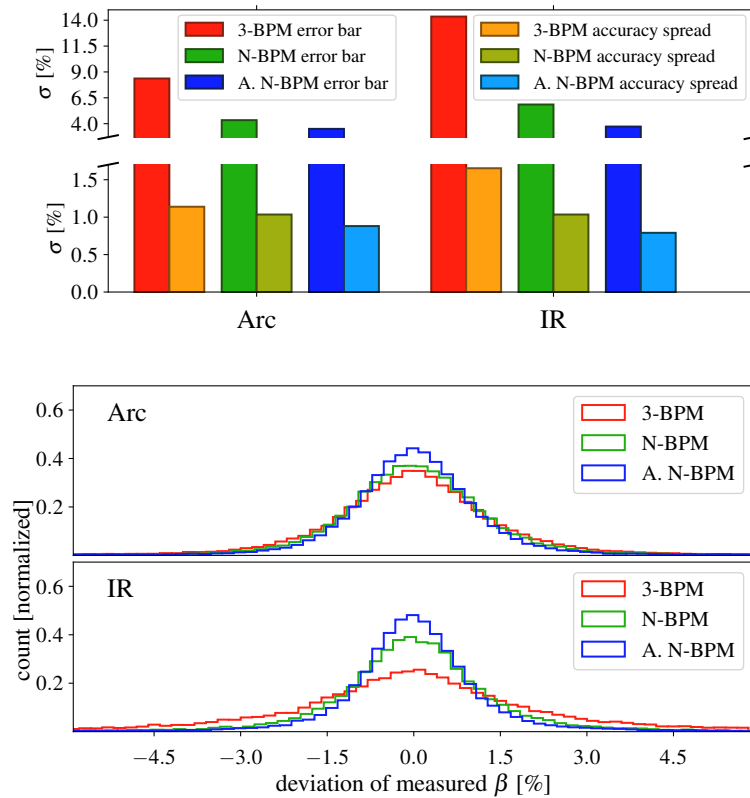


Figure 3.7: Same comparison of Figure 3.6 between the three methods for the HL-LHC $\beta^* = 15$ cm ATS optics. The analytical N-BPM method yields clearly better results, both in the IRs and in the arcs. Compared to the $\beta^* = 40$ cm optics shown in Figure 3.6, the β function reconstruction is less accurate: This was also demonstrated for the $\beta^* = 20$ cm optics in [40].

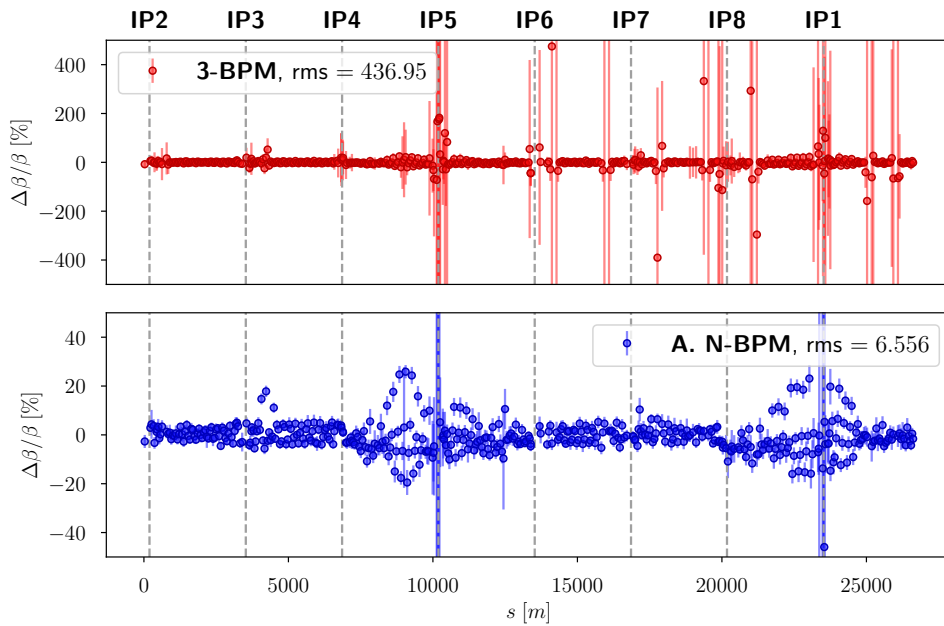


Figure 3.8: Horizontal β beating of beam 1 at $\beta^* = 10$ cm during the ATS MD 2016. TOP: 3-BPM method. BOTTOM: analytical N-BPM method. The 3-BPM method suffers from bad phase advances and has many outliers. The regions of high β beating at around 8000 m and 23 000 m lie in the telescopic arcs.

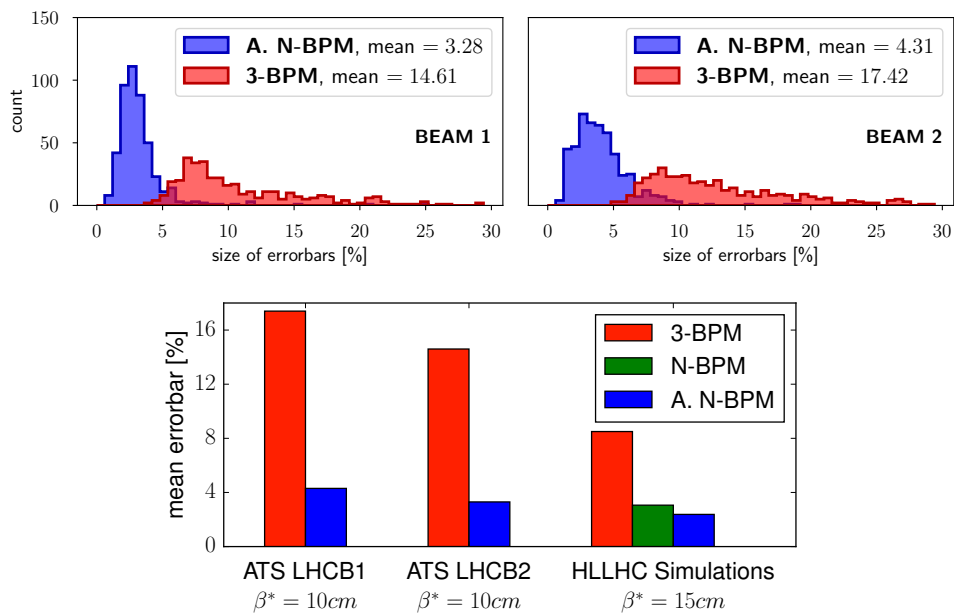


Figure 3.9: A comparison of the error bars of the $\beta^* = 10$ cm optics of the October 2016 MD. TOP LEFT: histogram of the error bars of beam 1. TOP RIGHT: histogram of the error bars of beam 2. BOTTOM: mean of the size the error bars. The mean of the analytical N-BPM method is a factor 4 more accurate than the 3 BPM method. The third set of values shows the mean of the error bars of the simulations as shown in Figure 3.7 but for the whole ring.

advances. A phase advance $\Delta\varphi$ is considered *bad* if $\Delta\varphi \in [n\pi - \delta, n\pi + \delta]$ for $n \in \mathbb{N}$ and a given threshold δ . If any of the four phase advances $\varphi_{ij_l}, \varphi_{ik_l}, \varphi_{ij_l}^m, \varphi_{ik_l}^m$ in Eq. (2.94) is bad, the corresponding BPM combination is disregarded in the calculation of the weighted mean. This allows us to still use several combinations but skipping those which are numerically unstable. The current value for the threshold is $\delta = 2\pi \cdot 10^{-2}$. The use of fewer combinations results in a lower computation time.

To test the analytical N-BPM method and compare it to the original 3-BPM and the Monte Carlo N-BPM method, a large set of LHC lattices with $\beta^* = 40$ cm with randomly distributed errors is generated and a measurement is simulated by tracking a single particle via polymorphic tracking code (PTC) [46]. The random errors are created from table 3.1 and a Gaussian noise of $\sigma_x = 0.1$ mm is applied to the BPM signal. No singular value decomposition cleaning is applied since it would clean the artificial noise too efficiently [47]. The excitation amplitude is 0.8 mm at a β function of about 120 m. The tracked particle positions are then analyzed by the three methods (3-BPM, N-BPM and analytical N-BPM) and the respective deviation from the real horizontal β function is shown in the bottom plot of Figure 3.6. The analytical N-BPM method includes the filtering of phase advances. Especially in the IR, where neighbouring BPMs have often unsuitable phase advances, the N-BPM and analytical N-BPM method yield more accurate values.

The top diagram of Figure 3.6 shows that the error of the 3-BPM method is considerable larger, whereas the N-BPM and analytical N-BPM method are very accurate with similar accuracies in the IR and arcs.

3.6 HL-LHC

The ATS optics [48] is the baseline choice for the HL-LHC and our optics measurement tools have to be prepared for the challenges imposed by such an optics. In Figure 3.7 the three methods are compared in the same way as in Figure 3.6. The excitation amplitude was 0.8 mm at a β function of 127 m. For the current HL-LHC collision optics ($\beta^* = 15$ cm) the performance of N-BPM and analytical N-BPM method is again better than the 3-BPM method, especially in the IRs. All three methods are, however, about a factor two more inaccurate than for the $\beta^* = 40$ cm optics of LHC, in agreement with Figure 7 of [40].

In the post-processing of the data taken during the LHC Machine Development measurement (MD) [49] for testing the ATS principle with a $\beta^* = 10$ cm optics, the analytical N-BPM method was used for the first time with filtering of bad phase advances. Figure 7 demonstrates that the analytical N-BPM method deals well with the ATS MD optics. Monte Carlo simulations were not possible for this optics.

Figure 3.9 shows the precision of the final results for the $\beta^* = 10$ cm optics of both beams

compared to the simulations of the HL-LHC lattice with $\beta^* = 15$ cm. To ease the comparison the error bars are shown in the bottom plot. They are slightly larger for the real measurement than those in simulations. We believe that the use of lower beam excitation to ensure machine protection is behind these larger error bars. Figure 3.8 shows also that the 3-BPM method has many outliers and error bars up to several kilometers caused by bad phase advances. Large error bars have been excluded for the mean shown in Fig. 3.9.

The Monte Carlo simulations failed for low β^* optics and so we were not able to use the original N-BPM method during ATS MDs. This is another advantage of the analytical N-BPM method that it is able to evaluate the systematic errors independently of the success of particle tracking.

3.7 Conclusion

A new method for the measurement of β and α functions has been developed based on the existing N-BPM method. A fully analytical calculation of the covariance matrix provides a faster and more accurate measurement of β and α functions. The analytical N-BPM method also avoids the complications from failing to find closed optics that occur in the Monte Carlo simulations needed by the existing N-BPM method. This stability with respect to the choice of optics model makes it more suitable for low β^* optics. Simulations show that, together with a filtering of BPM combinations according to the phase advances, the method is optimal for the HL-LHC upgrade.

In the last years, the analytical N-BPM method has been used as standard method to measure the β function in LHC beam commissioning and machine development studies where it has been producing a high quality analysis and contributed to the remarkable performance of the LHC in run II. The method also has been used in collaborative efforts with accelerators from several external institutes like SuperKEKB (KEK) and PETRA III (DESY).

A LOCAL OBSERVABLE FOR LINEAR LATTICE IMPERFECTIONS

Finding a truly local observable for perturbations of the linear beam dynamics is a nontrivial task, contrary to the nonlinear regime, where local resonance driving terms already exist. The phase beating between two locations depends on errors outside of this region. However, phase advances between four nearby locations can be arranged in a way to cancel the contributions from errors outside of this region up to first order. The resulting local observable contains valuable information about quadrupolar lattice imperfections. This chapter seeks to explore this local phase beating observable and to test its usefulness for gaining insight in the linear optics imperfections of a circular accelerator.

This chapter is entirely based on original work of the author. Section 4.1 gives a brief introduction and motivation for the presented work. Section 4.2 presents the main part with a rather technical derivation of the local observable. A thorough verification of the validity and possible use cases are presented in section 4.3, using the LHC as example. In section 4.4 actual measurement data, acquired during LHC beam commissioning, conducted by the OMC team, is compared to the simulated results.

The content of this chapter has been published in [50].

4.1 Introduction

Special accelerator segments like the interaction regions of colliders need a precise control of local optics which becomes a challenging task if the optics are pushed to more extreme settings. New methods and more precise hardware are required to measure and correct machine imperfections such as quadrupole errors. In the case of a collider the exact measurement and control of the β function at the interaction point is important for operation of the machine and to optimise luminosity [51].

In contrast to a global correction of the phase advance, which is only valid for a certain

optics configuration, the identification and correction of a distinct local error source would cancel this error source for all optics configurations.

In order to locate error sources we are interested in local observables, i.e. terms that only depend on lattice parameters and error sources in a localised region. Such a local observable does not exist for linear lattice imperfections. For the non-linear ones one has been found so far [31, 35]:

$$\chi(N) = \frac{\hat{x}_1(N)}{\cos\left(\varphi_{x,12} - \frac{\pi}{2}\right)} + \frac{\hat{x}_3(N)}{\cos\left(\varphi_{x,23} - \frac{\pi}{2}\right)} + \hat{x}_2(N) \left(\tan\left(\varphi_{x,12} - \frac{\pi}{2}\right) + \tan\left(\varphi_{x,23} - \frac{\pi}{2}\right) \right) . \quad (4.1)$$

$\chi(N)$ is built with the signal of three beam position monitors at positions s_1, s_2, s_3 .

An extension of $\chi(N)$ into the linear regime does not seem possible since measured amplitude and phase are used in a way to remove information on the linear beam dynamics.

Certain optics parameters (e.g. the β function or coupling) can be calculated from the phase advances between two or three BPMs [52, 17, 38] independently from BPM calibration errors [53]. The phase advance measured from a Fourier Transform [54] turn-by-turn data is independent of the amplitude of the signal and, thus, not affected by calibration errors.

The phase advance between two elements of an accelerator depends, in general, on all the elements in the ring. Focusing errors are of particular interest with their first order influence on the β function. The impact they cause on RDTs can be seen in Eq. (2.72), explicitly for a single error source located at position s_1 :

$$f_{2000,j} = \delta K \beta_x(s_1) e^{2i[\varphi(s_j) - \varphi(s_1)]} \quad (4.2)$$

The top plot of Figure 4.1 illustrates the effect of a single focusing error on the RDT. In the case of a model phase advance of π or a multiple of it, the effect is identical on both BPMs, if the error does not occur in between them. In the other case both BPMs experience different effects on their RDTs as shown in the bottom plot.

From Eq. (2.83) one can see that the effect on the phase advance depends, up to first order, on global terms only in the form of $\mathcal{R}e\{f_j - f_i\}$.

Under the assumption that coupling and higher order imperfections are negligible we study the effect of quadrupolar field errors on the phase advance up to first order and construct an observable for linear lattice imperfections that is local. For second order considerations we find a formula for phase beating but global contributions cannot be eliminated.

The focus of this work lies on circular machines where phase advance can be measured accurately by exciting an oscillation of the beam. Excitation methods include single kicks

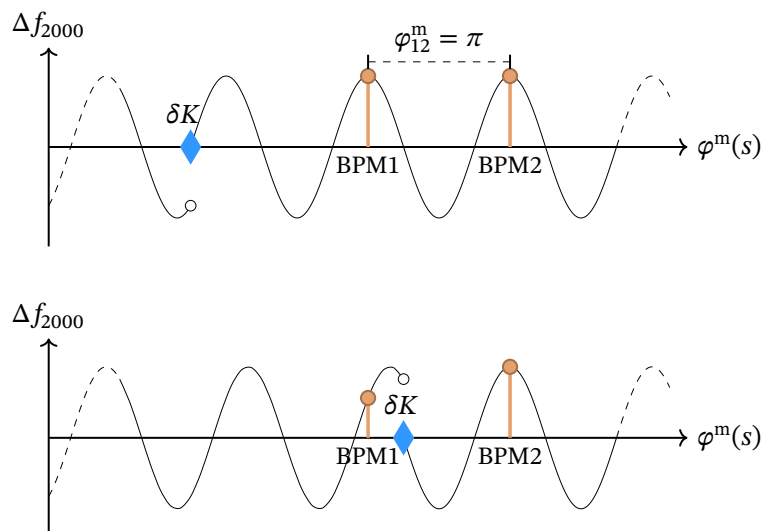


Figure 4.1: Sketch of the effect of a focus error ΔK on f_{2000} . The error creates a phase advance beating $\propto e^{2i\varphi^m}$. The discontinuity at the position of the source is caused by the propagation of the phase beating around the ring. TOP: If the error lies outside the interval from BPM1 to BPM2 and the model phase advance between the two BPMs is exactly π , the effect is the same and the phase advance beating is unaffected by this error. BOTTOM: If the error lies in between the two BPMs no cancellation is possible.

and driven oscillation by an AC-dipole [16] which generate a stable coherent motion of the beam. Conceptually the local observable described in this work applies also to linear machines¹ but accurate measurements of phase advances remain challenging in this kind of accelerator and the application of the proposed technique might not be practical. Instead model-based fitting methods [55] might be more suited to retrieve optics parameters directly.

4.2 Local observable

The effect of linear lattice imperfections on the resonance driving terms (RDTs) and their impact on the betatron phase is studied. We express the betatron motion in the language of normal form and Courant-Snyder coordinates [30].

The phase beating due to quadrupolar field errors is given by Eq. (2.87) which is repeated here for convenience:

$$\Delta\varphi_{ij} = \bar{h}_{ij} - 8 \sin^2 \varphi_{ij}^m \mathcal{R}e\{f_i\} - 8 \sin \varphi_{ij}^m \cos \varphi_{ij}^m \mathcal{I}m\{f_i\} + O(f^2) \quad . \quad (4.3)$$

\bar{h}_{ij} only depends on quadrupole errors inside the range $[i, j]$ and is therefore a local term. The RDTs f_i in Eq. (2.87), on the other hand, contain global contributions.

¹Here, *linear* refers to a straight beam line as opposed to a lattice of linear magnets

The following subsections describe the derivation of an expression for local phase beating in two distinct cases: The first is the general case with arbitrary phase advances between the BPMs. A combination of four BPMs is necessary to calculate a pure local term. The second case considers only two BPMs with a phase advance of π .

4.2.1 The general case – phase advances different from $n\pi$

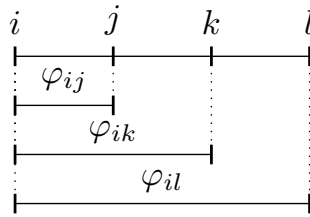


Figure 4.2: The interval of BPMs with corresponding phase advances.

Equation (2.87) still carries a dependence on the global error distribution in the form of the terms f_i . We can eliminate those terms by carefully summing up phase advances between different pairs of BPMs.

The goal of this section is to eliminate global contributions to Eq. (2.87). This can be achieved a careful resummation of phase advances between four BPMs.

The global term $\mathcal{R}e\{f_i\}$ can be eliminated by taking a third BPM k and divide by the respective factor:

$$\frac{\Delta\varphi_{ij}}{\sin^2 \varphi_{ij}^m} - \frac{\Delta\varphi_{ik}}{\sin^2 \varphi_{ik}^m} = \frac{\bar{h}_{ij}}{\sin^2 \varphi_{ij}^m} - \frac{\bar{h}_{ik}}{\sin^2 \varphi_{ik}^m} - 8(\cot \varphi_{ij}^m - \cot \varphi_{ik}^m) \mathcal{I}m\{f_i\} \quad . \quad (4.4)$$

Proceeding similarly with the factor in front of $\mathcal{I}m\{f_i\}$:

$$\frac{\frac{\Delta\varphi_{ij}}{\sin^2 \varphi_{ij}^m} - \frac{\Delta\varphi_{ik}}{\sin^2 \varphi_{ik}^m}}{\cot \varphi_{ij}^m - \cot \varphi_{ik}^m} = \frac{\frac{\bar{h}_{ij}}{\sin^2 \varphi_{ij}^m} - \frac{\bar{h}_{ik}}{\sin^2 \varphi_{ik}^m}}{\cot \varphi_{ij}^m - \cot \varphi_{ik}^m} - 8 \mathcal{I}m\{f_i\} \quad . \quad (4.5)$$

We can simplify the left-hand side to:

$$\begin{aligned}
\frac{\frac{\Delta\varphi_{ij}}{\sin^2\varphi_{ij}^m} - \frac{\Delta\varphi_{ik}}{\sin^2\varphi_{ik}^m}}{\cot\varphi_{ij}^m - \cot\varphi_{ik}^m} &= \frac{\Delta\varphi_{ij}}{\sin^2\varphi_{ij}^m(\cot\varphi_{ij}^m - \cot\varphi_{ik}^m)} - \frac{\Delta\varphi_{ik}}{\sin^2\varphi_{ik}^m(\cot\varphi_{ij}^m - \cot\varphi_{ik}^m)} \\
&= \frac{\Delta\varphi_{ij}\sin\varphi_{ij}^m\sin\varphi_{ik}^m}{\sin^2\varphi_{ij}^m(\cos\varphi_{ij}^m\sin\varphi_{ik}^m - \cos\varphi_{ik}^m\sin\varphi_{ij}^m)} \\
&\quad - \frac{\Delta\varphi_{ik}\sin\varphi_{ij}^m\sin\varphi_{ik}^m}{\sin^2\varphi_{ik}^m(\cos\varphi_{ij}^m\sin\varphi_{ik}^m - \cos\varphi_{ik}^m\sin\varphi_{ij}^m)} \\
&= \frac{\Delta\varphi_{ij}(\sin\varphi_{ij}^m\cos\varphi_{jk}^m + \cos\varphi_{ij}^m\sin\varphi_{jk}^m)}{\sin\varphi_{ij}^m\sin\varphi_{jk}^m} \\
&\quad - \frac{\Delta\varphi_{ik}(\sin\varphi_{ik}^m\cos\varphi_{jk}^m - \cos\varphi_{ik}^m\sin\varphi_{jk}^m)}{\sin\varphi_{ik}^m\sin\varphi_{jk}^m} \\
&= \Delta\varphi_{ij}(\cot\varphi_{ij}^m + \cot\varphi_{jk}^m) - \Delta\varphi_{ik}(\cot\varphi_{jk}^m - \cot\varphi_{ik}^m) \quad . \quad (4.6)
\end{aligned}$$

The rhs of Eq. (4.5) can be simplified analogously and we can rewrite it to

$$\begin{aligned}
&\Delta\varphi_{ij}(\cot\varphi_{ij}^m + \cot\varphi_{jk}^m) - \Delta\varphi_{jk}(\cot\varphi_{jk}^m - \cot\varphi_{ik}^m) \\
&= \bar{h}_{ij}(\cot\varphi_{ij}^m + \cot\varphi_{jk}^m) - \bar{h}_{jk}(\cot\varphi_{jk}^m - \cot\varphi_{ik}^m) - \mathcal{I}m\{f_i\} \quad . \quad (4.7)
\end{aligned}$$

To finally eliminate $\mathcal{I}m\{f_i\}$ we take a fourth BPM, l , and subtract

$$\Delta\varphi_{ij}(\cot\varphi_{ij}^m + \cot\varphi_{jl}^m) - \Delta\varphi_{jl}(\cot\varphi_{jl}^m - \cot\varphi_{il}^m)$$

from Eq. (4.7) and end up with

$$\begin{aligned}
&\cot\varphi_{jl}^m(\Delta\varphi_{il} - \Delta\varphi_{ij}) + \cot\varphi_{jk}^m(\Delta\varphi_{ij} - \Delta\varphi_{ik}) - \cot\varphi_{ki}^m\Delta\varphi_{ik} + \cot\varphi_{li}^m\Delta\varphi_{il} \\
&= \cot\varphi_{jl}^m(\bar{h}_{il} - \bar{h}_{ij}) + \cot\varphi_{jk}^m(\bar{h}_{ij} - \bar{h}_{ik}) - \cot\varphi_{ki}^m\Delta\varphi_{ik} + \cot\varphi_{li}^m\bar{h}_{il} \quad . \quad (4.8)
\end{aligned}$$

Figure 4.3 illustrates the collection of four BPMs used to construct Eq. (4.8). The left hand side of Eq. (4.8) can be further simplified to

$$\begin{aligned}
&\cot\varphi_{jl}^m(\Delta\varphi_{il} - \Delta\varphi_{ij}) + \cot\varphi_{jk}^m(\Delta\varphi_{ij} - \Delta\varphi_{ik}) - \cot\varphi_{ki}^m\Delta\varphi_{ik} + \cot\varphi_{li}^m\Delta\varphi_{il} \\
&= \cot\varphi_{jl}^m\Delta\varphi_{jl} - \cot\varphi_{jk}^m\Delta\varphi_{jk} + \cot\varphi_{ik}^m\Delta\varphi_{ik} - \cot\varphi_{il}^m\Delta\varphi_{il} \quad . \quad (4.9)
\end{aligned}$$

Now we can rewrite Eq. (4.8) as

$$\Phi_{ijkl}^{\text{meas}} = \Phi_{ijkl}^{\text{model}} \quad (4.10)$$

by defining

$$\Phi_{ijkl}^{\text{meas}} \equiv \cot\varphi_{jl}^m\Delta\varphi_{jl} - \cot\varphi_{jk}^m\Delta\varphi_{jk} + \cot\varphi_{ik}^m\Delta\varphi_{ik} - \cot\varphi_{il}^m\Delta\varphi_{il} \quad (4.11)$$

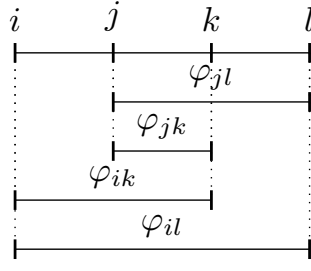


Figure 4.3: The phase advances appearing in Eqs. (4.13) and (4.14). The phase advances φ_{ij} and φ_{kl} do not appear in the final form of the local observable.

and

$$\Phi_{ijkl}^{\text{model}} \equiv \cot \varphi_{jl}^m (\bar{h}_{il} - \bar{h}_{ij}) - \cot \varphi_{jk}^m (\bar{h}_{ij} - \bar{h}_{ik}) + \cot \varphi_{ik}^m \bar{h}_{ik} - \cot \varphi_{il}^m \bar{h}_{il} \quad . \quad (4.12)$$

Those terms are truly local to the region in between the four BPMs.

The resummation yields an observable

$$\begin{aligned} \Phi_{ijkl}^{\text{meas}} &= \cot \varphi_{jl}^m \Delta \varphi_{jl} - \cot \varphi_{jk}^m \Delta \varphi_{jk} \\ &\quad + \cot \varphi_{ik}^m \Delta \varphi_{ik} - \cot \varphi_{il}^m \Delta \varphi_{il} \end{aligned} \quad (4.13)$$

which only depends on measured phase advances between the four BPMs i , j , k and l . Up to first order it is equal to an analytic expression

$$\begin{aligned} \Phi_{ijkl}^{\text{model}} &= \cot \varphi_{jl}^m (\bar{h}_{il} - \bar{h}_{ij}) - \cot \varphi_{jk}^m (\bar{h}_{ij} - \bar{h}_{ik}) \\ &\quad + \cot \varphi_{ik}^m \bar{h}_{ik} - \cot \varphi_{il}^m \bar{h}_{il} \end{aligned} \quad (4.14)$$

which depends only on local error sources. There are no global contributions left and the two quantities defined in Eqs. (4.13) and (4.14) are truly local up to first order. The measurement uncertainty can be propagated to $\Phi_{ijkl}^{\text{meas}}$:

$$\begin{aligned} \sigma_{\Phi}^2 &= \cot^2 \varphi_{jl}^m \sigma_{\varphi_{jl}}^2 + \cot^2 \varphi_{jk}^m \sigma_{\varphi_{jk}}^2 \\ &\quad + \cot^2 \varphi_{ik}^m \sigma_{\varphi_{ik}}^2 + \cot^2 \varphi_{il}^m \sigma_{\varphi_{il}}^2 \quad . \end{aligned} \quad (4.15)$$

Equation (4.15) is used to calculate the size of the error bars in local observable plots.

A consideration of degrees of freedom suggests that three BPMs should suffice to reconstruct the local linear optics errors. However, this reconstruction would depend on the amplitude which, in turn, may suffer from calibration errors. The local observable presented here is independent of BPM calibration errors. Figure 4.4 illustrates the impact of a quadrupole error on the local observable. The plot shows an LHC arc with 90° FODO cells. Two BPMs are placed in one FODO cell, directly in front of the focusing or defocus-

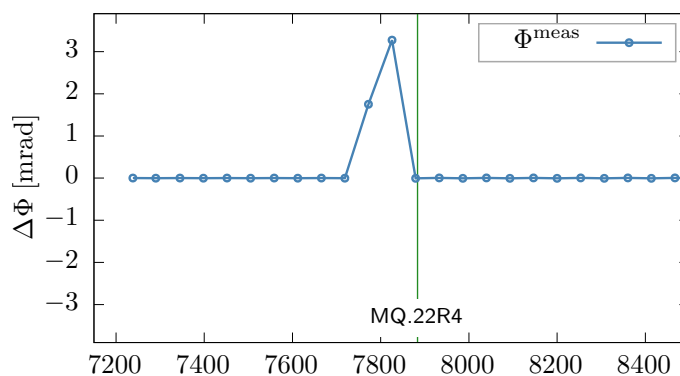


Figure 4.4: The impact of a focusing error on the local observable. The plot shows an LHC arc with a relative error of 0.1 % of the magnetic field of focusing quadrupole MQ.22R4 which is marked by a vertical line.

ing quadrupoles, respectively. The BPMS i , j , k and l are chosen to be consecutive ones. A relative field error of 0.1 % was introduced at magnet MQ.22R4. Since the points corresponding to a value of $\Phi_{ijkl}^{\text{meas}}$ are placed at the position s_i , only the three points that precede the introduced error are affected, for which the introduced error lies in the interval $[s_i, s_l]$. The first of the three affected points has a very small value because of the proximity of the quadrupole to the BPM.

4.2.2 Exact multiples of π

If the model phase advance is $\varphi_{ij}^m = n\pi$, the phase advance beating between two positions, Eq. (2.87) reduces to

$$\Delta\varphi_{ij} = \bar{h}_{ij} \quad , \quad (4.16)$$

which implies that $\Delta\varphi_{ij}$ is directly a local observable when $\varphi_{ij}^m = n\pi$. In this case the number of BPMs is reduced to two at positions i and j . In general, phase advances that are sufficiently close to multiples of π might not be present in standard operation of an accelerator – an exception is for example the ATS optics [48] that is now used in LHC and which is the proposed baseline for its high luminosity upgrade –, but it would be conceivable to prepare special optics settings for a corresponding measurement in any accelerator, given that it allows freely changing the optics parameters. The error of the local observable in this case,

$$\sigma_{\Delta\varphi_{ij}} = \sigma_{\varphi_{ij}} \quad , \quad (4.17)$$

is smaller than for the general local observable.

4.2.3 Exploring the second order

The detuning Hamiltonian term $h_{1100,ij}$ as well as the RDT f_i have to be extended to second order:

$$h_{1100,ij} \rightarrow h_{1100,ij}^{(1)} + h_{1100,ij}^{(2)} \quad (4.18)$$

$$f_i \rightarrow f_i^{(1)} + f_i^{(2)} \quad . \quad (4.19)$$

The total phase advance beating is, then,

$$\begin{aligned} \Delta\varphi_{ij} = & -2h_{1100,ij}^{(1)} - 2h_{1100,ij}^{(2)} + 4\mathcal{R}e\{f_j^{(1)} - f_i^{(1)}\} \\ & + 4\mathcal{R}e\{f_j^{(2)} - f_i^{(2)}\} \\ & + 16\left(\mathcal{R}e\{f_j^{(1)}\}\mathcal{I}m\{f_j^{(1)}\} - \mathcal{R}e\{f_i^{(1)}\}\mathcal{I}m\{f_i^{(1)}\}\right) \\ & + O(K^3) \quad . \end{aligned} \quad (4.20)$$

The same resummation techniques as for the first order will not suffice to eliminate global RDTs f_i and f_j . If we reformulate the third line of Eq. (4.20) as

$$\begin{aligned} \mathcal{R}e\{f_j\}\mathcal{I}m\{f_j\} - \mathcal{R}e\{f_i\}\mathcal{I}m\{f_i\} &= \frac{1}{2}\mathcal{I}m\{f_j^2\} - \frac{1}{2}\mathcal{I}m\{f_i^2\} \\ &= \frac{1}{2}\mathcal{I}m\{A_{ij}^2 + 2A_{ij}f_i e^{2i\varphi_{ij}^m} + (e^{4i\varphi_{ij}^m} - 1)f_i^2\} \end{aligned} \quad (4.21)$$

we see that it is not possible to separate the global f_i from the local term A_{ij} . This separation was the key to be able to eliminate the global terms in the first order approximation.

For $\varphi_{ij}^m = n\pi$ a second order term can be derived analogously:

$$\begin{aligned} \Delta\varphi_{ij} = & \bar{h}_{ij} - 2h_{1100,ij}^{(2)} \\ & + 4\mathcal{R}e\{f_j^{(2)} - f_i^{(2)}\} + 8\mathcal{I}m\{A_{ij}^2 + 2A_{ij}f_i\} \quad . \end{aligned} \quad (4.22)$$

This term also contains the global f_1 and f_2 and there are no common factors that can be exploited to eliminate them.

Therefore in this work purely local observable cannot be extracted from the second order phase beating.

Element	$\sigma_{K_1}/K [10^{-4}]$
MQ	12
MQT	75
MQM	12
MQY	11
MQW	15
MQX	1
MB	4

Table 4.1: Error distribution for the design LHC lattice at 6.5 TeV with weak errors in the final triplet in order to avoid higher order effects. K denotes the main field component (quadrupolar field for quadrupoles, etc).

4.3 Simulating Errors and Noise

4.3.1 General simulation setup

In order to assess the usability of the local observable we perform a series of simulations with different quadrupole error distributions and compare the prediction of the analytical calculations with simulated results. We base our simulations on the nominal LHC lattice at the end of run II in 2018 with ATS optics and $\beta^* = 30$ cm.

Figure 4.5 shows a sketch of a typical LHC arc section. BPMs are placed directly in front of the quadrupoles of FODO cells. Additional trim quadrupoles (e.g. MQT) may be present. Four cases will be studied: the first one is a set of expected LHC errors from magnetic

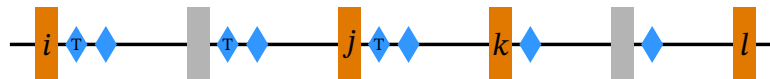


Figure 4.5: The probed interval I_p for a typical section inside an LHC arc. BPMs are represented by rectangles. The phase advance between consecutive BPMs is approximately 45° . Used BPMs are shown in orange, unused in gray. Blue diamonds indicate quadrupoles and trim quadrupoles. Only BPMs and quadrupoles are shown, other elements such as corrector spool pieces and the bending dipoles are omitted.

measurements [44, 45], shown in Tab. 4.1, in the absence of phase noise. This setup will let us verify the equality of Eqs. (4.13) and (4.14). Then Gaussian noise of $0.7 \times 10^{-3} \times 2\pi$ rad is added to the simulated phase advances to illustrate the behaviour in the presence of noise. A third simulation includes an additional strong error source in one of the quadrupoles, c.f. Tab. 4.2 to demonstrate the impact of single strong error sources and the locality of the local observable. A last simulation setup demonstrates the visibility of quadrupolar errors originating from feed-down of sextupoles via orbit offsets.

There are many different possible combinations of BPMs. In the following comparison plots we will only show two of them: one that has a phase advance of 180° in one of the phase advances appearing in Fig. 4.6 and one that avoids such a term and, additionally, the

Element	$\delta K_1/K [10^{-4}]$	$\sigma_{K_1}/K [10^{-4}]$
MQ.22R4.B1	100	-
MQ	-	12
MQT	-	75
MQM	-	12
MQY	-	11
MQW	-	15
MQX	-	1
MB	-	4

Table 4.2: In addition to the error distribution of Table 4.1 we introduced a single strong error source in arc45.

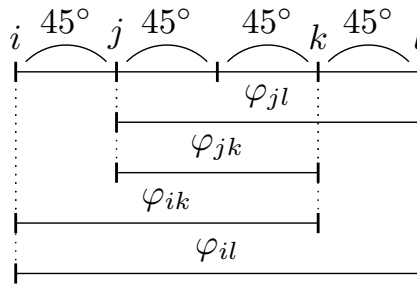


Figure 4.6: The phase advances of the combination $\varphi_{ij} = 45^\circ$, $\varphi_{jk} = 90^\circ$, $\varphi_{kl} = 45^\circ$. The phase advance $\varphi_{il} = 180^\circ$ causes $\cot \varphi_{ij}^m$ to diverge.

2-BPM combination with $\varphi_{ij} = 180^\circ$.

In a real measurement we would consider only the combinations of closest BPMs to avoid the accumulation of systematic errors coming from other lattice elements and therefore we limit our study to only those combinations. The phase advance over two FODO cells in telescopic arcs of the ATS optics is tightly matched to π . On the one hand this provides a continuous set of combinations with similar phase advances and thus we can more easily compare the values of $\Phi_{ijkl}^{\text{model}}$ and $\Phi_{ijkl}^{\text{meas}}$ at different positions. On the other hand this gives rise to model phase advances close to multiples of π for several combinations which gives the possibility to explore these cases. Table 4.3 shows the closest combinations with all occurring model phase advances. Reflected combinations are omitted. Model phase advances close to $n\pi$ cause the cotangent terms to diverge. They are therefore highlighted in red. Since we still want to study these cases and avoid divergences and the resulting numerical instabilities we impose a filter on the phase advances. Those which are closer to $n\pi$ than $10^{-6} \times 2\pi$ are excluded. The case $45^\circ - 90^\circ - 45^\circ$ is sketched in Fig. 4.6.

Model and measurement values are shown for the combinations $45^\circ - 45^\circ - 45^\circ$ and $90^\circ - 45^\circ - 45^\circ$ and $\varphi_{ij}^m = 180^\circ$ in Figures 4.7 to 4.9. Since we get the phase advances of Table 4.3 only for telescopic arcs and for the sake of readability we limit the plot region to just one telescopic arc, the one between IR4 and IR5. For simplicity we show only results for the horizontal plane.

sketch of combination	$\varphi_{jl} - \varphi_{jk} - \varphi_{ik} - \varphi_{il}$
	$90^\circ - 45^\circ - 90^\circ - 135^\circ$
	$90^\circ - 45^\circ - 135^\circ - 180^\circ$
	$135^\circ - 90^\circ - 135^\circ - 180^\circ$
	$135^\circ - 45^\circ - 135^\circ - 225^\circ$

Table 4.3: Indices i, j, k, l and phases appearing model phase advances for the closest combinations. The actual model phase advances depend on the respective model settings and differ slightly from the exact values above.

4.3.2 LHC with known field errors

The first case, Fig. 4.7, is free of noise with the quad error distribution of Tab. 4.1, with a distribution of known LHC magnet errors as measured in [44, 45]. The agreement between analytical and measurement values is excellent, showing the validity of Eqs. (4.13), (4.14) and (4.16).

To examine the behaviour of the local observable in the vicinity of $n\pi$ we have to scan the accelerator for available model phase advances. For each BPM i we are looking for a second one – BPM j – that is placed at $\Delta\varphi_{ij} = \pi \pm \delta\varphi$ downstream. $\delta\varphi$ is a threshold parameter controlling how many local observable pairs are accepted. We chose $\delta\varphi = 1 \times 10^{-3} \times 2\pi$. The telescopic arcs of the ATS optics provide the needed model phase advances.

The agreement is, as for the general case, very good in the absence of errors.

4.3.3 Phase noise

The noise to signal ratio decreases with increasing oscillation amplitude and thus with increasing β function at the BPM. In the LHC FODO cells BPMs are installed close to the focusing and defocusing quadrupoles and those lie at β function maxima and minima, respectively. Therefore we can divide the arc BPMs in two categories, those with low β function and those with high β function. The β function minima are usually around 30 m and the maxima at 180 m. The phase advance uncertainties $\sigma_{\varphi_{ij}}$ fall into three categories: both BPMs have high β function, only one of them has high β and both have low β .

For this set of simulations we introduce phase noise which corresponds to noise values of the LHC signal that we typically achieve taking five data acquisitions and after cleaning [56] and harmonic analysis. We group BPMs into the before mentioned categories and apply a Gaussian error distribution to the phase values according to measurement statistics.

With the introduced phase noise the agreement decreases significantly (cf. Fig. 4.8). The noise is of the same order of magnitude as $\Phi_{ijkl}^{\text{meas}}$ itself. Therefore the LHC arc quadrupolar errors cannot be identified with this phase advance resolution. The combination $45^\circ -$

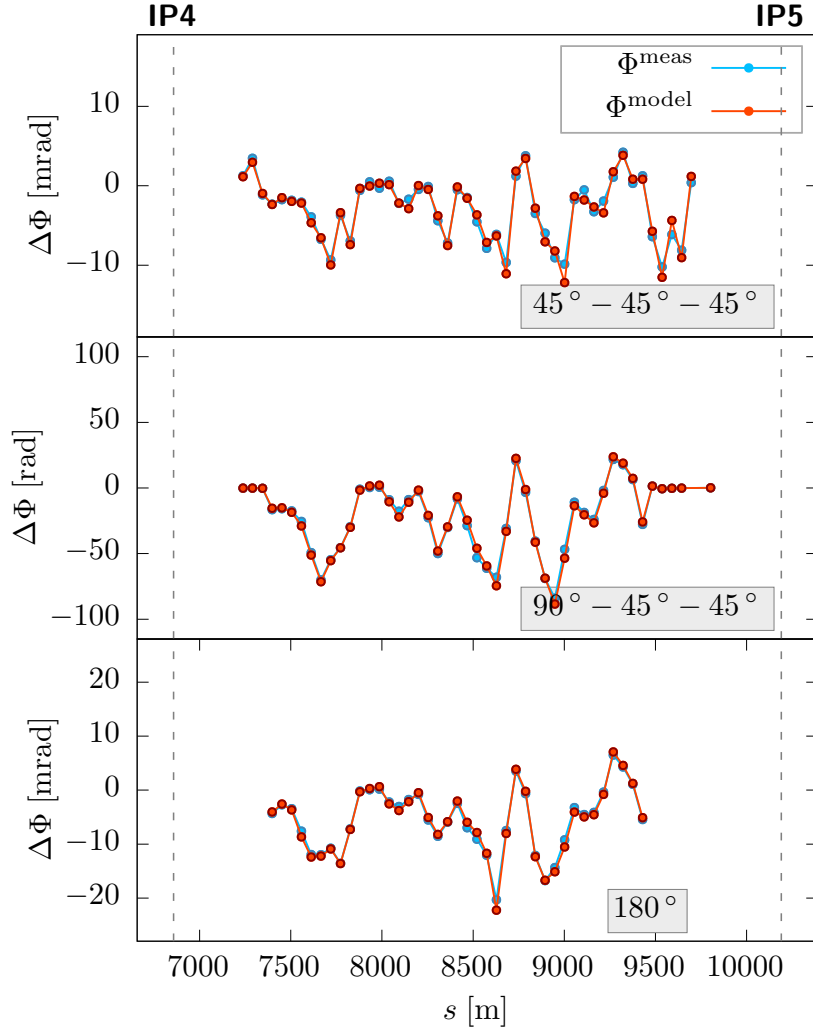


Figure 4.7: This figure shows the first two combinations of Tab. 4.3 and the case $\varphi_{ij}^m = \pi$ from simulations. Top: the combination $45^\circ - 45^\circ - 45^\circ$. Center: the combination $90^\circ - 45^\circ - 45^\circ$. The absolute value of the local observable in the telescopic arc (right of IP4) is four orders of magnitude higher than in the top plot. The plots only show values where the phase advances do not differ more than 1° from the target values displayed in Tab. 4.3 in order to ensure comparability between the values. Additionally values with a model phase advance in $n\pi \pm 10^{-6}$ are excluded to avoid numerical instabilities. This causes the IR to be empty of local phase advances. Note that in the middle plot the values are four orders of magnitude higher than in the other two. This originates from the $\cot \varphi_{il}^m$ terms which are high because of $\varphi_{il}^m \approx \pi$. The bottom plot shows the local observable for model phase advances of 180° . In all three plots the agreement between model and simulation is excellent.

$45^\circ - 45^\circ$ shows the worst behaviour under noise because the β function alternates between high and low values from BPM to BPM and so within the four neighbouring BPMs there are always two with low β function. The case of exact π phase advances shows the smallest errors as only one phase advance error enters in the error propagation.

4.3.4 Single strong error source

For the next simulation, we assume that there is a single strong error in one of the quadrupoles. We assign 1% of relative error to MQ.22R4 to show the effect of a strong error source. Figure 4.9 shows that this error creates a visible peak in the local observable. The peak in the local observable is situated immediately in front of the location of the error source because the plot shows the local observable at the position of BPM i but the errors of the interval (s_i, s_l) enter in the calculation of the observable.

In the presence of model phase advances close to $n\pi$ the values of the local observable in the telescopic arcs are clearly enhanced (c.f. bottom plot of Fig. 4.7 and Fig. 4.8).

The simulations above show that strong quadrupolar error sources ($\geq 1\%$) can be detected with the local observables under the studied phase resolution. For the detection of smaller errors a higher precision of the phase measurement would be needed. More precise BPMs like DOROS-BPMs [57] currently installed in the LHC interaction region and a higher excitation amplitude as well as the acquisition of a higher number of turns can increase the resolution of the phase measurement.

4.3.5 Feed-down from sextupoles

As final test case we introduce orbit offset into the machine around the IPs by activating dedicated dispersion bumps. These are used in the ATS optics to compensate dispersion created by the crossing angles at the IPs. The transverse displacement of the beam creates quadrupolar-like errors inside sextupoles via feed-down:

$$\Delta K_{1,\text{sext}} = \delta x K_2 \quad (4.23)$$

where δx denotes horizontal offset and K_2 is the strength of the sextupole. $K_{1,\text{sext}}$ can now be used for the calculation of the local observable.

Figure 4.10 shows the local observable in this case. Regular bumps created by the feed-down appear which are consistent in all three cases but less pronounced in the nearest neighbors case. With the given noise level those bumps can be measured. The local observable is not affected by feed-down in the center of the arc because sextupoles at places with high orbit offset are turned off. In comparison to the previous examples, Figs. 4.8 and

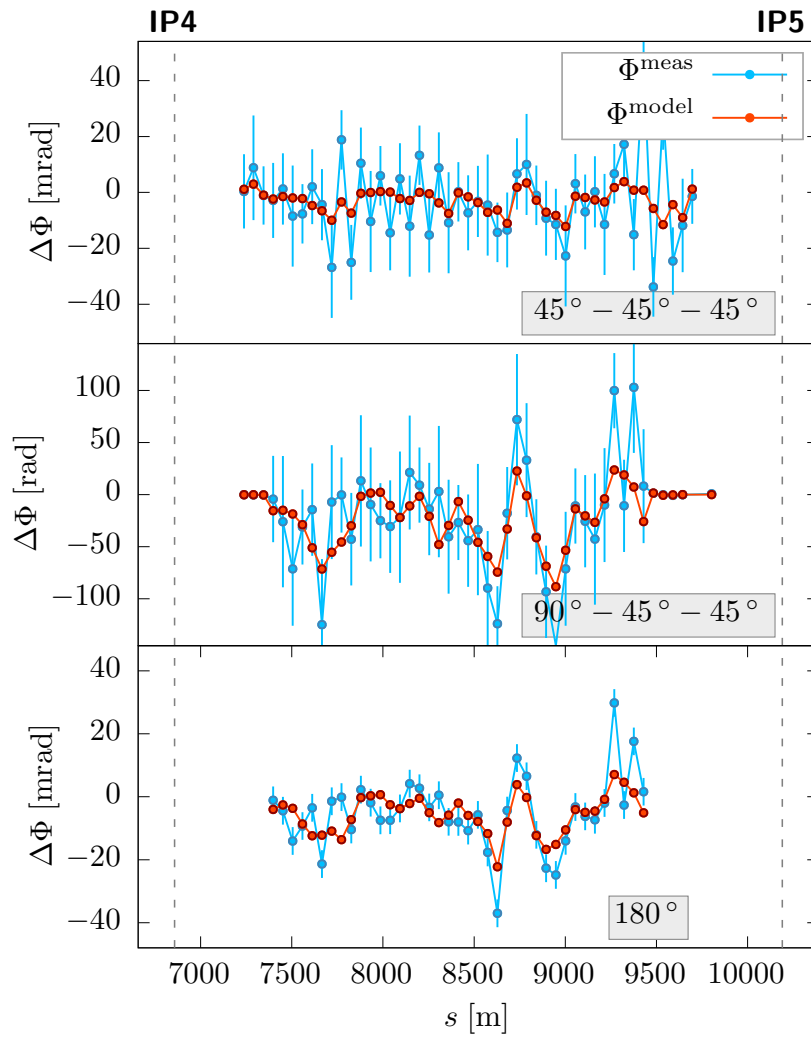


Figure 4.8: Similar plots as in Fig. 4.7 but including a phase error of $0.7 \times 10^{-3} \times 2\pi$ rad for high β function values and $1.8 \times 10^{-3} \times 2\pi$ rad for low β s. The agreement between model and simulation and measurement is highly deteriorated. The error bars have been calculated using Eqs. (4.15) and (4.17). The case $\varphi_{ij}^m = \pi$ is affected less by the error since only one phase advance error is propagated.

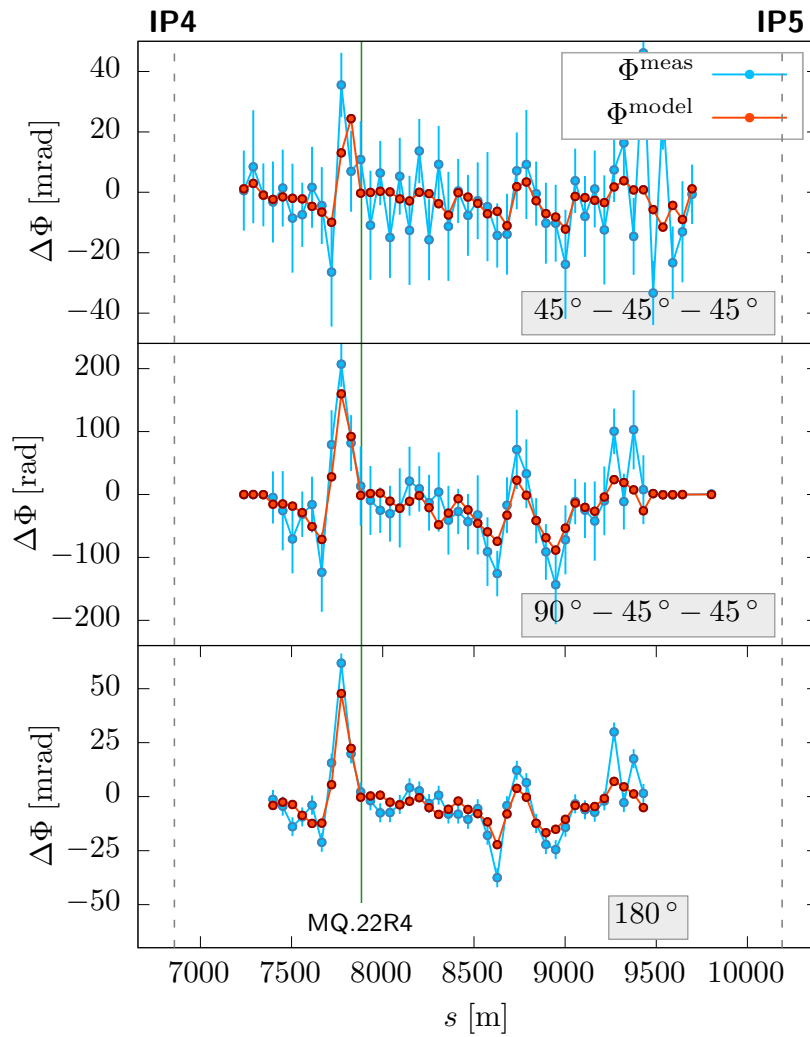


Figure 4.9: The local observable with the error distribution of Tab. 4.2, including a strong error source at MQ.22R4.B1 and phase noise of $0.7 \times 10^{-3} \times 2\pi$ rad. The position of the strong error source is marked by a green line.

4.9, the values of the local observable did not change in this region.

The bottom plot of Fig. 4.10 shows the changed orbit for reference. The peaks of the local observable can be identified with the peaks in the orbit. Again the local observable is in advance of the error source.

4.4 Experimental verification

We calculate the local observable from a measurement taken during the LHC beam commissioning in 2018.

The measurement can be seen in Fig. 4.11 for the combinations $45^\circ - 45^\circ - 45^\circ$ (top plot) and $90^\circ - 45^\circ - 45^\circ$ (bottom plot).

We take a model lattice where dispersion bumps are turned off in order to see the impact on the local observable. As discussed in section 4.3, the feed-down of sextupole fields due to the orbit offset of those bumps changes the local observable. Figure 4.11 shows in blue the measured local observable which features similar spikes as the simulation (cf. Fig. 4.10). In red the effect of feed-down from sextupoles via the orbit offset on the local observable is shown. The feed down has been calculated by introducing the dispersion bump knob into the model that was turned on during the measurement and calculating $\delta K_{1,\text{sext}}$ from Eq. (4.23). The pattern of the model values is also present in the measurement which confirms that their origin is indeed the feed-down. Since the $\Phi_{ijkl}^{\text{model}}$ contains only the expected feed-down from sextupoles and no other error sources (like normal quadrupole imperfections) the difference between model and measurement is then the actual local observable created by those error sources. The center region of the arc is free of a high peak because, as in the simulation, no sextupole is active at high orbit offsets.

4.5 Conclusion and Outlook

We showed the existence of a local observable for linear lattice imperfections in circular accelerators. The locality of the observable holds up to first order in the quadrupole error δK_1 .

Phase measurement noise is an issue with the current precision of turn-by-turn measurements and a higher resolution in the measurement would be of advantage. For certain use cases, new techniques are needed to improve the control of the machine and hardware upgrades are a justified solution. Simulations show that strong error sources can be identified even with current precision of LHC measurements as they generate distinguishable peaks.

The calculated local observable of an actual measurement shows a picture that is compati-

ble with simulations. Feed-down of orbit offsets via sextupoles can be seen in measurement data and be reproduced in simulations.

A future application of the observable to find strong local sources and to guide local error corrections is foreseen for run III of the LHC.

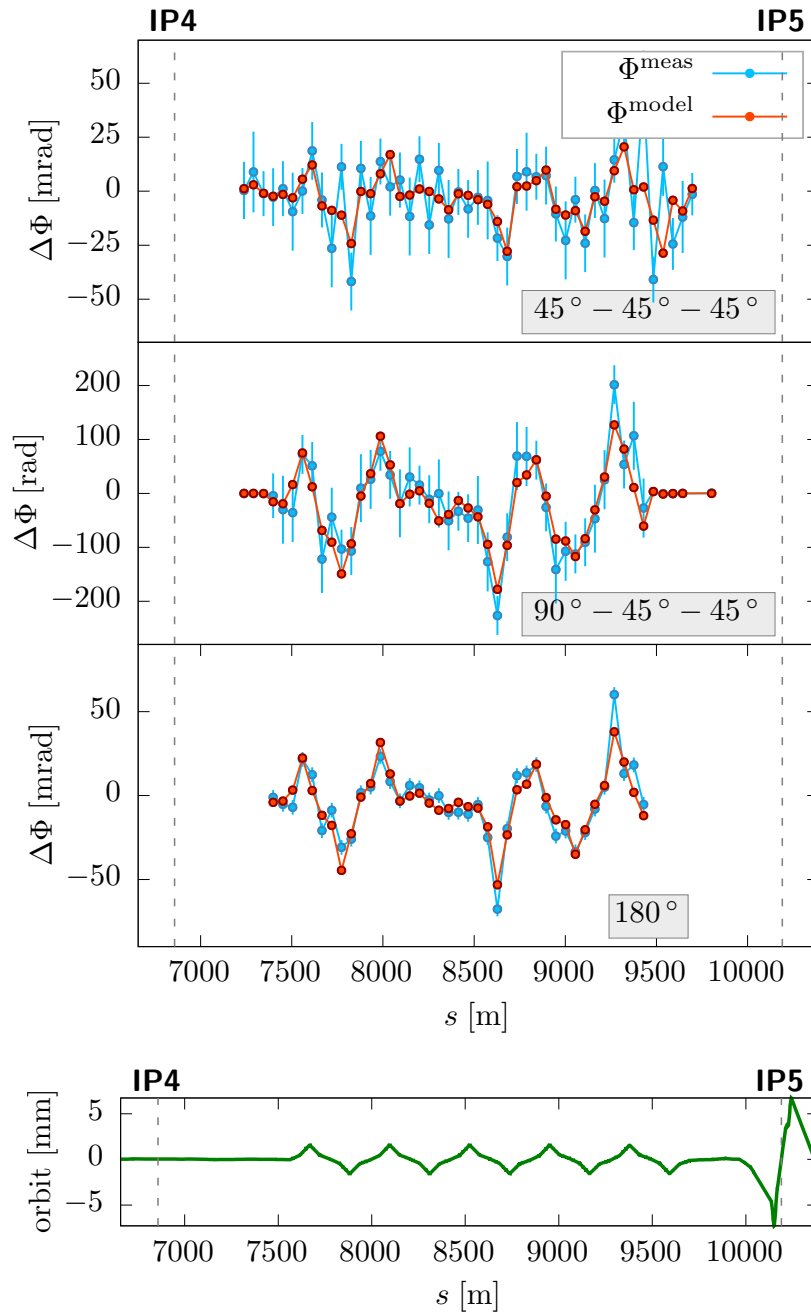


Figure 4.10: The local observable with the error distribution of Tab. 4.1 and phase noise of $0.7 \times 10^{-3} \times 2\pi$ rad. Additionally the orbit has been changed by dispersion bumps. The orbit offset creates feed-down from sextupoles.

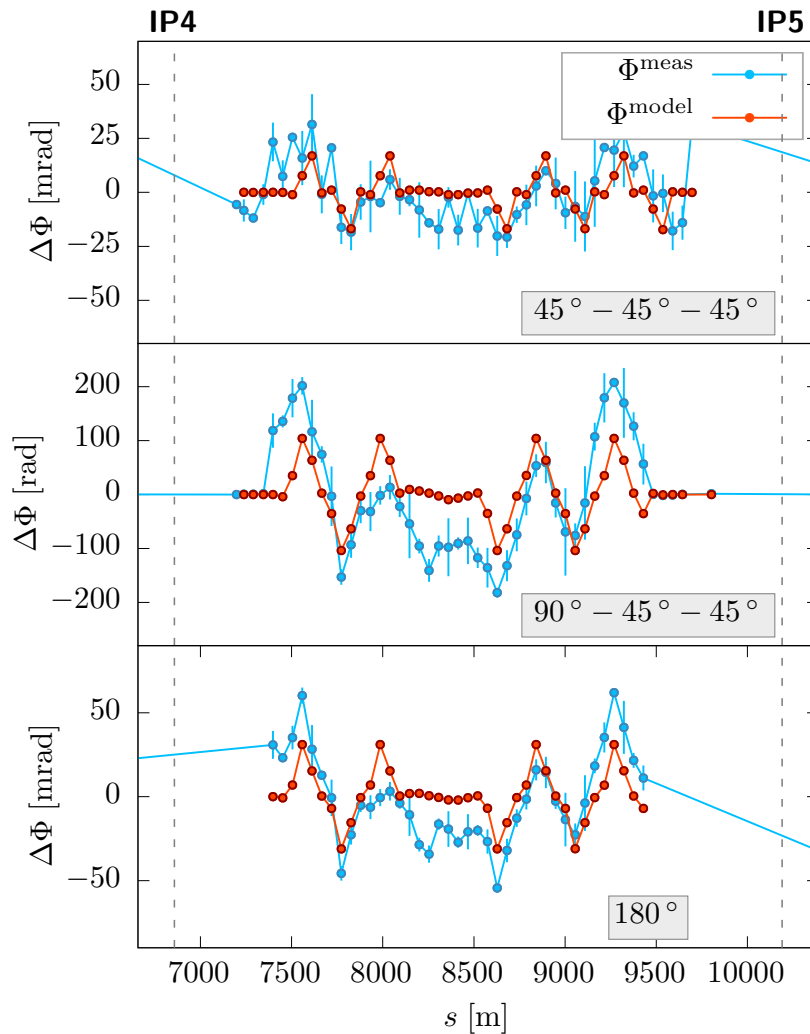


Figure 4.11: Plot of measurement data of the LHC commissioning 2018 at $\beta^* = 30$ cm. The error bars include statistical errors obtained from the phase measurement of the FFT. The effect of dispersion bumps on the local observable is clearly visible and matches well the prediction. The center region shows only a small effect from sextupoles.

FORCED COUPLING RESONANCE DRIVING TERMS

The goal of this chapter is the study of of resonance driving terms when measured from driven motion. The driving of the particle motion by an AC-dipole changes measured quantities like the optics functions β , α and the phase, as discussed in section 2.6.2, and also has an impact on resonance driving terms. Recent findings suggest that the current models describing the forced RDTs are neglecting a local effect of the AC-dipole, creating a jump of the amplitude of the RDTs f_{jklm} . The case of sextupolar RDTs has been studied. In this work, coupling RDTs are calculated for the first time in view of the new findings.

Original work is presented in form of the derivation of the driven RDT f_{1001} and the simulation study of the new formula, including comparisons to existing descriptions. Sections 5.1.1 and 5.1.3 review existing work.

5.1 Driven coupled motion

Resonance driving terms are calculated from the spectral lines of the turn-by-turn data as shown in section 2.5.2 for the coupling RDTs. Since the particle's motion is affected by the driving of forced oscillation by the AC-dipole, the spectrum also undergoes a change and the measured RDTs are not equal to the free ones.

In the past, two methods were used to model the effect of the driven motion, the first is a simple rescaling of the tune dependent denominators of the RDTs, this method will therefore be called the *rescaling* method.

The second one [17] applies the findings of a detailed study of the driven particle motion using the equations of motion of the particle in the accelerator with an AC-dipole. This method provides reconstruction and compensation formulae for all optics parameters, including those that enter into the coupling terms. This method will be called *formula method*

in the following.

Recent findings [58] show that the AC-dipole locally affects RDTs and introduces a jump in amplitude of the RDTs at its location. Even the detailed considerations of the formula method lack such an effect. In view of the suggestions of [58] this work presents calculations of the terms f_{1001} and f_{1010} , building upon the techniques introduced in 2.6.1. A comparison between rescaling method, formula method and the newly calculated coupling terms is shown.

5.1.1 AC-dipole as skew quadrupole

To consider beam motion that is driven *and* coupled, we illustrate the effect of an AC-dipole as coupling source by stating the analogy between their impact on the particles motion.

Throughout this chapter the following convention is used:

$$\begin{aligned} f_+ &\equiv f_{0101} \text{ and} \\ f_- &\equiv f_{0110} \quad . \end{aligned} \quad (5.1)$$

The RDTs in Eq. (2.91) can be reformulated:

$$f_{\pm} = \frac{\sum J_{1,w} \sqrt{\beta_{x,w} \beta_{y,w}} e^{i[\varphi_{wj,x} \pm \varphi_{wj,y}] - i\pi[Q_x \pm Q_y]}}{8i \sin[\pi(Q_x \pm Q_y)]} \quad . \quad (5.2)$$

The coupled motion for a single coupling source now reads

$$\begin{aligned} h_x(s_j, N) &= \zeta_x^+(s_j, N) \\ &+ 2i \frac{J_{1,w} \sqrt{\beta_{x,w} \beta_{y,w}}}{8i \sin[\pi(Q_x + Q_y)]} \zeta_y^+(s_j, N) e^{i[\Delta\varphi_x^+ + 2\pi(Q_x + Q_y)\Theta(s_j, s_w)] - i\pi[Q_x + Q_y]} \\ &+ 2i \frac{J_{1,w} \sqrt{\beta_{x,w} \beta_{y,w}}}{8i \sin[\pi(Q_x - Q_y)]} \zeta_y^-(s_j, N) e^{i[\Delta\varphi_x^- + 2\pi(Q_x - Q_y)\Theta(s_j, s_w)] - i\pi[Q_x - Q_y]} \quad , \end{aligned} \quad (5.3)$$

with

$$\Delta\varphi_x^{\pm} = \varphi_x(s_j) - \varphi_x(s_w) \pm (\varphi_y(s_j) - \varphi_y(s_w)) \quad . \quad (5.4)$$

The $\Theta(s_j, s_w)$ terms come from the wrapping around of the phase advance. Noting that

$\zeta_y^+(s_j, N) = \sqrt{2I_y} e^{2\pi i N Q_y + \varphi(s_j)}$ one can bring this in a form similar to Eq. (2.142)

$$\begin{aligned}
h_x(s_j, N) = & \zeta_x^+(s_j, N) \\
& + \frac{J_{1,w} \sqrt{\beta_{x,w} \beta_{y,w}}}{4 \sin[\pi(Q_x + Q_y)]} \sqrt{2I_y} e^{2\pi i N Q_y + \varphi(s_j) + i[\Delta\varphi_x^+ + 2\pi(Q_x + Q_y)\text{sgn}(s_w - s_j)]} \\
& + \frac{J_{1,w} \sqrt{\beta_{x,w} \beta_{y,w}}}{4 \sin[\pi(Q_x - Q_y)]} \sqrt{2I_y} e^{-2\pi i N Q_y + \varphi(s_j) + i[\Delta\varphi_x^- + 2\pi(Q_x - Q_y)\text{sgn}(s_w - s_j)]} \quad . \quad (5.5)
\end{aligned}$$

The following table summarises which quantities are analogous

AC dipole	coupling
A_θ	$J_{1,w} \sqrt{I_y \beta_y}$
$\varphi_x(s_d)$	$\varphi_y(s_j) - \varphi_y(s_w) \mp \varphi_x(s_w)$
Q_x^d	Q_y

Thus, the AC dipole couples the beam's motion to its oscillation, similar to a skew quadrupole which couples horizontal and vertical motion.

5.1.2 Derivation of the coupled driven motion

The derivation of the coupled driven motion presented in this section follows a similar path to the derivation of the coupled free motion, leveraging the normal form approach as in section 2.4.2. The major difference is the presence of AC-dipole kicks, Eq. (2.122) that appear in each turn. These kicks have to be interleaved with the particles turn-by-turn motion in the normal form space. Figure 5.1 illustrates the procedure. The coordinates are propagated in normal form space and transformed to physical space at $s_d - \epsilon$, directly in front of the AC-dipole. Then an AC-dipole kick $\Delta h_x(N)$ is performed and the physical coordinate is transformed back to normal form space where it is rotated around the ring. This process is repeated for each turn.

In the first turn, before the beam experiences the AC-dipole kick, the coordinates are those from Eq. (2.90):

$$\begin{aligned}
h_x^+(s_d - \epsilon, 0) &= e^{:F:} \zeta_x^+(s_d - \epsilon, 0) \\
&= \zeta^+(s_d - \epsilon, 0) + 2i f_{1001}^* \zeta_y^+(s_d - \epsilon, 0) + 2i f_{1010}^* \zeta_y^-(s_d - \epsilon, 0) \quad (5.6)
\end{aligned}$$

Then the particle is kicked in p direction:

$$\begin{aligned}
h_x^\pm(s_d + \epsilon, 0) &= h_x^\pm(s_d - \epsilon, 0) + \Delta h_x^\pm(0) \\
h_y^\pm(s_d + \epsilon, 0) &= h_y^\pm(s_d - \epsilon, 0) + \Delta h_y^\pm(0) \quad (5.7)
\end{aligned}$$

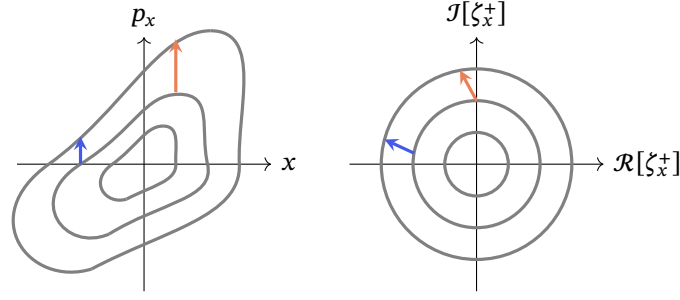


Figure 5.1: Two AC-dipole kicks in p_x at different positions in phase space can have completely different appearance in normal form coordinates. The transformation is not restricted to the two dimensions depicted in this figure but can happen in all four normal form coordinates ζ_x^+ , ζ_x^- , ζ_y^+ , ζ_y^- .

where the superscript \pm of $\Delta h_z^\pm(N)$ denotes which of h_z^+ or h_z^- is experiencing the kick. The following holds:

$$\Delta h_z^- = (\Delta h_z^+)^* = -\Delta h_z^+ \quad . \quad (5.8)$$

For the transformation back to normal form space Eq. (2.59) has to be applied:

$$\zeta = e^{-F}: h = h + [-F, h] + O(h^3) \quad (5.9)$$

with

$$F = \sum f_{jklm} (h_x^+)^j (h_x^-)^k (h_y^+)^l (h_y^-)^m \quad (5.10)$$

when applied to h_z^\pm . The normal form of the kicked particle motion now reads

$$\begin{aligned} \zeta_x^+(s_d + \epsilon, 0) &= h_x^+(s_d + \epsilon) - 2if_{1001}^*(s_d)h_y^+(s_d + \epsilon, 0) - 2if_{1010}^*(s_d)h_y^-(s_d + \epsilon, 0) \\ &= \tilde{h}_x^+(s_d + \epsilon, 0) + \Delta h_x(0) \\ &\quad - 2if_{1001}^*(s_d)(\tilde{h}_y^+(s_d + \epsilon, 0) + \Delta h_y^+(0)) \\ &\quad - 2if_{1010}^*(s_d)(\tilde{h}_y^-(s_d + \epsilon, 0) + \Delta h_y^-(0)) \\ &= \tilde{\zeta}_x^+(s_d + \epsilon, 0) + \Delta h_x(0) - 2if_{1001}^*(s_d)\Delta h_y^+(0) - 2if_{1010}^*(s_d)\Delta h_y^-(0) \end{aligned} \quad (5.11)$$

where the tilde denotes undriven coordinates. Propagation to the next turn is just a simple application of the transformation R_x , turning the coordinate $\tilde{\zeta}_z^+(s, 0)$ into $\tilde{\zeta}_z^+(s, 1)$. The operator in front of Δh_z is written out explicitly for now to avoid confusion. Its effect will be calculated later. At turn 1, just in front of the AC-dipole, the particle's coordinate reads

$$\begin{aligned} \zeta_x^+(s_d - \epsilon, 1) &= R_x \zeta_x^+(s_d + \epsilon, 0) \\ &= \tilde{\zeta}_x^+(s_d - \epsilon, 1) + R_x \Delta h_x(0) - 2if_{1001}^*(s_d)R_x \Delta h_y^+(0) - 2if_{1010}^*(s_d)R_x \Delta h_y^-(0) \quad . \end{aligned} \quad (5.12)$$

Before applying the AC-dipole kick it is again transformed to CS space:

$$\begin{aligned}
h_x^+(s_d - \epsilon, 1) &= R_x \zeta_x^+(s_d + \epsilon, 0) \\
&= \tilde{\zeta}_x^+(s_d - \epsilon, 1) + R_x \Delta h_x(0) - 2i f_{1001}^*(s_d) R_x \Delta h_y^+(0) - 2i f_{1010}^*(s_d) R_x \Delta h_y^-(0) \\
&\quad + 2i f_{1001}^*(s_d) \left(\tilde{\zeta}_y^+(s_d - \epsilon, 1) + \frac{1}{2} R_x \Delta h_y^+(0) \right) \\
&\quad + 2i f_{1010}^*(s_d) \left(\tilde{\zeta}_y^-(s_d - \epsilon, 1) + \frac{1}{2} R_x \Delta h_y^-(0) \right) \\
&\quad + O(f^2) \quad , \tag{5.13}
\end{aligned}$$

where $O(f^2)$ denotes quadratic and cross terms of f_{1001} and f_{1010} and the factor $\frac{1}{2}$ in front of the kick terms comes from second order calculations of the Poisson bracket. A kick $\Delta h_x(1)$ is applied and this procedure can be continued to arbitrary order N . To avoid lengthy expressions, the driven uncoupled coordinates $h_z^{d\pm}$ are defined as

$$\begin{aligned}
h_z^{d\pm} &= \tilde{h}_z^{\pm} + \frac{A_\theta \beta(s_d)}{4 \sin(\pi Q_z)} \left\{ e^{\pm i[-2N\pi Q_z^d - \varphi_{s_d s} + \pi Q_z^- \text{sgn}(s-s_d)]} \right. \\
&\quad \left. - \lambda_z e^{\pm i[2N\pi Q_z^d - \varphi_{s_d s} - \pi Q_z^+ \text{sgn}(s-s_d)]} \right\} \tag{5.14}
\end{aligned}$$

where the sum up to turn N has already been carried out as in section 2.6.1. Note that the transformation from CS space to normal form space is carried out directly after the kick, thus fixing f_{1001} and f_{1010} acting on Δh_y^{\pm} to this position, i.e. s_d . When calculating the CS coordinates at arbitrary position s , on the other hand, the RDTs acting on ζ_y^{\pm} are evaluated at the position s . Therefore the coordinate, at position $s < s_d$ reads

$$\begin{aligned}
h_x^+(s < s_d, N) &= h_x^{d+}(s, N) + 2i f_{1001}^*(s) h_y^{d+}(s, N) + 2i f_{1010}^*(s) h_y^{d-}(s, N) \\
&\quad - 2i f_{1001}^*(s_d) \frac{1}{2} \sum_{T=1}^N R_{s-s_d} R_x^T \Delta h_y^+(N-T) \\
&\quad - 2i f_{1010}^*(s_d) \frac{1}{2} \sum_{T=1}^N R_{s-s_d} R_x^T \Delta h_y^-(N-T) \quad , \tag{5.15}
\end{aligned}$$

and, after the AC-dipole,

$$\begin{aligned}
h_x^+(s > s_d, N) &= h_x^{d+}(s, N) + 2i f_{1001}^* h_y^{d+}(s, N) + 2i f_{1010}^* h_y^{d-}(s, N) \\
&\quad - 2i f_{1001}^*(s_d) \frac{1}{2} \sum_{T=0}^N R_{x, s-s_d} R_x^T \Delta h_y^+(N-T) \\
&\quad - 2i f_{1010}^*(s_d) \frac{1}{2} \sum_{T=0}^N R_{x, s-s_d} R_x^T \Delta h_y^-(N-T) \quad . \tag{5.16}
\end{aligned}$$

The rotation $R_{x,s-s_d}$ is caused by the transfer of ζ_z^\pm to the position s , before transformation into Courant-Snyder space is performed. The term $\sum_{T=0}^N R_x^T \Delta h_y^+(N-T)$ can be simplified as in section 2.6.1:

$$\begin{aligned} \sum_{T=0}^N R_x^T \Delta h_y^+(N-T) &= i \frac{A_\theta \beta(s_d)}{2} \left\{ \sum_{T=0}^N R_x \delta_{y+}^{N-T} + \sum_{T=0}^N R_x \delta_{y-}^{N-T} \right\} \\ &= i \frac{A_\theta \beta(s_d)}{2} \left\{ R_x^N \frac{1 - (R_x^{-1} \delta_{y+})}{1 - R^{-1} \delta_{y+}} + R_x^N \frac{1 - (R_x^{-1} \delta_{y-})}{1 - R^{-1} \delta_{y-}} \right\} \\ &= \frac{A_\theta \beta(s_d)}{4} \left\{ \frac{1 - e^{2\pi i N [Q_x + Q_y^d]}}{e^{i\pi [Q_x + Q_y^d]} \sin [\pi (Q_x + Q_y^d)]} - \frac{1 - e^{-2\pi i N [Q_y^d - Q_x]}}{e^{i\pi [Q_y^d - Q_x]} \sin [\pi (Q_y^d - Q_x)]} \right\}. \end{aligned} \quad (5.17)$$

For the term $\sum_{T=0}^N R_x^T \Delta h_y^-(N-T)$ a similar process is performed, noting that the action of R_x^N now is

$$R^N \Delta h_y^- = e^{-2i\pi N Q_x} \Delta h_y^- \quad . \quad (5.18)$$

Combining the above, the expression for the coupled driven motion becomes

$$\begin{aligned} h_x^\pm(s, N) &= h_x^{d\pm}(s, N) + 2i f_{1001}^* h_y^{d+}(s, N) + 2i f_{1010}^* h_y^{d-}(s, N) \\ &\quad - 2i f_{1001}^*(s_d) h_{y,x}^+(s, N) - 2i f_{1010}^*(s_d) h_{y,x}^-(s, N) \quad , \end{aligned} \quad (5.19)$$

with the definition

$$\begin{aligned} h_{y,x}^\pm(s, N) &= \frac{A_\theta \beta(s_d)}{8} \left\{ \frac{e^{\pm i [-2N\pi Q_y^d + \pi(Q_y^d - Q_x) \text{sgn}(s-s_d) - \varphi_{s_d}^x]}}{\sin [\pi(Q_y^d - Q_x)]} \right. \\ &\quad \left. - \frac{e^{\pm i [2N\pi Q_y^d - \pi(Q_y^d + Q_x) \text{sgn}(s-s_d) - \varphi_{s_d}^x]}}{\sin [\pi(Q_y^d + Q_x)]} \right\} \quad . \end{aligned} \quad (5.20)$$

In section 2.5.2 a way to measure coupling in realistic conditions is introduced. In order to get the new driven RDT, f_{1001}^{drv} , one can look at the result of a theoretical measurement without calibration errors and with perfect knowledge of the complex signal. Under these conditions one can get f_{1001} from the free motion by (cf. Eq. (2.96))

$$f_{1001,x}^* = \frac{H^+(0, 1)}{2iV^+(0, 1)} \quad (5.21)$$

$$f_{1001,y} = \frac{V^+(1, 0)}{2iH^+(1, 0)} \quad . \quad (5.22)$$

In the driven case, on the other hand, the coordinates change $h_z^\pm \rightarrow h_z^{d\pm}$, which causes also the generating terms to change $f_{jklm} \rightarrow f_{jklm}^d$ and, finally, the kick cross-terms pollute the

driven motion. The easy term to calculate in Eq. (5.21) is $V^+(0, 1)$

$$\begin{aligned} V^+(0, 1) &= \mathcal{F}\{h_y^+\}(Q_y^d) = \mathcal{F}\{h_y^{d+}\}(Q_y^d) \\ &= \frac{A_\theta \beta(s_d)}{4 \sin(\pi Q_y^-)} e^{i[-\varphi_{s_d}^y + \pi Q_y \text{sgn}(s-s_d)]} \end{aligned} \quad (5.23)$$

$H^+(0, 1)$, however, includes many terms proportional to $e^{-i\pi N Q_y^d}$:

$$\begin{aligned} H^+(0, 1) &= 2i f_{1001}^* \mathcal{F}\{h_y^{d+}\}(Q_y^d) + 2i f_{1010}^* \mathcal{F}\{h_y^{d-}\}(Q_y^d) \\ &\quad - 2i f_{1001}^*(s_d) \mathcal{F}\{h_{y,x}^+\}(Q_y^d) - 2i f_{1010}^*(s_d) \mathcal{F}\{h_{y,x}^-\}(Q_y^d) \end{aligned} \quad (5.24)$$

For readability the fourier transforms are listed separately:

$$\begin{aligned} \mathcal{F}\{h_y^{d+}\}(Q_y^d) &= \frac{A_\theta \beta(s_d)}{4 \sin \pi Q_y^-} e^{i[-\varphi_{s_d}^y + \pi Q_y^- \text{sgn}(s-s_d)]} \quad , \\ \mathcal{F}\{h_y^{d-}\}(Q_y^d) &= \frac{\lambda_y A_\theta \beta(s_d)}{4 \sin \pi Q_y^-} e^{i[\varphi_{s_d}^y + \pi Q_y^+ \text{sgn}(s-s_d)]} \quad , \\ \mathcal{F}\{h_{y,x}^+\}(Q_y^d) &= \frac{A_\theta \beta(s_d)}{8 \sin [\pi(Q_y^d - Q_x)]} e^{i[-\varphi_{s_d}^x + \pi(Q_y^d - Q_x) \text{sgn}(s-s_d)]} \quad , \\ \mathcal{F}\{h_{y,x}^-\}(Q_y^d) &= \frac{A_\theta \beta(s_d)}{8 \sin [\pi(Q_y^d + Q_x)]} e^{i[\varphi_{s_d}^x + \pi(Q_y^d + Q_x) \text{sgn}(s-s_d)]} \quad . \end{aligned} \quad (5.25)$$

From this it is easy to calculate the driven coupling term, as obtained from a measurement of the horizontal signal

$$\begin{aligned} f_{1001,x}^{\text{drv}*} &= f_{1001}^* + f_{1001}^*(s_d) \frac{\sin \pi Q_y^-}{2 \sin [\pi(Q_y^d - Q_x)]} e^{i[\varphi_{s_d}^x - \varphi_{s_d}^y + \pi(Q_y - Q_x) \text{sgn}(s-s_d)]} \\ &\quad + \lambda_y f_{1010}^* e^{2i[\varphi_{s_d}^y + \pi Q_y]} + f_{1010}^*(s_d) \frac{\sin \pi Q_y^-}{2 \sin [\pi(Q_y^d + Q_x)]} e^{i[\varphi_{s_d}^x + \varphi_{s_d}^y + \pi(Q_y + Q_x) \text{sgn}(s-s_d)]} \quad . \end{aligned} \quad (5.26)$$

From Eq. (5.26) it is apparent that the AC-dipole adds two effects to the difference RDT f_{1001} the first one,

$$f_{1001}^*(s_d) \frac{\sin \pi Q_y^-}{2 \sin [\pi(Q_y^d - Q_x)]} e^{i[\varphi_{s_d}^x - \varphi_{s_d}^y + \pi(Q_y - Q_x) \text{sgn}(s-s_d)]} \quad (5.27)$$

is creating an additional source at the position of the AC-dipole, proportional to f_{1001} at this position and the second one,

$$\lambda_y f_{1010}^* e^{2i[\varphi_{s_d}^y + \pi Q_y]} + f_{1010}^*(s_d) \frac{\sin \pi Q_y^-}{2 \sin [\pi(Q_y^d + Q_x)]} e^{i[\varphi_{s_d}^x + \varphi_{s_d}^y + \pi(Q_y + Q_x) \text{sgn}(s-s_d)]} \quad (5.28)$$

mixes the difference term with the sum term f_{1010} (as well as a second contribution pro-

portional to f_{1001}). The mixing-in of those terms is suppressed by the factors λ_y and the denominator $\sin[\pi(Q_y^d + Q_x)]$, respectively.

5.1.3 Rescaling and Formula methods

For the sake of completeness, rescaling and formula methods will be stated here. The detailed derivation can be looked up in the respective publications [59, 16].

The rescaling method simply rescales the coupling terms f_{1001} and f_{1010} by their expected denominators:

$$\begin{aligned} f_{\pm,x}^{\text{drv}} &= \frac{\sin(Q_x \pm Q_y)}{\sin(Q_x^d \pm Q_y)} f_{\pm} \\ f_{\pm,y}^{\text{drv}} &= \frac{\sin(Q_x \pm Q_y)}{\sin(Q_x \pm Q_y^d)} f_{\pm} \end{aligned} \quad (5.29)$$

The index x/y refers to the plane in which the f term is measured. For the formula method, a complete expression for the driven RDTs can be derived:

$$\begin{aligned} f_{\pm,x} = \frac{1}{\sqrt{1 - \lambda_x^2}} \frac{\sin[\pi(Q_x \mp Q_y)]}{\sin[\pi(Q_x^d \mp Q_y)]} \left\{ e^{i(\varphi_{s_d^s}^{d,x} - \varphi_{s_d^s}^x)} f_{\mp} + \lambda_x \lambda_c e^{i(\varphi_{s_d^s}^{d,x} - \varphi_{s_d^s}^x)} f_{\pm}^* \right. \\ \left. + 2i \sin(\pi(Q_x^-)) e^{i(\varphi_{s_d^s}^{d,x} - \varphi_{s_d^s}^x)} f_{\pm}(s; s, s_d) \right. \\ \left. + 2i \lambda_c^{-1} \sin(\pi(Q_x^-)) e^{i(\varphi_{s_d^s}^{d,x} + \varphi_{s_d^s}^x)} f_{\mp}(s; s, s_d) \right\} \quad , \quad (5.30) \end{aligned}$$

for the f terms as measured from the signal in the horizontal plane, and

$$\begin{aligned} f_{\pm,y} = \frac{1}{\sqrt{1 - \lambda_y^2}} \frac{\sin[\pi(Q_x \mp Q_y)]}{\sin[\pi(Q_x \mp Q_y^d)]} \left\{ e^{i(\varphi_{s_d^s}^{d,x} - \varphi_{s_d^s}^x)} f_{\mp} + \lambda_x \lambda_c e^{i(\varphi_{s_d^s}^{d,x} - \varphi_{s_d^s}^x)} f_{\pm}^* \right. \\ \left. + 2i \sin(\pi(Q_x^-)) e^{i(\varphi_{s_d^s}^{d,x} - \varphi_{s_d^s}^x)} f_{\pm}(s; s, s_d) \right. \\ \left. + 2i \lambda_c^{-1} \sin(\pi(Q_x^-)) e^{i(\varphi_{s_d^s}^{d,x} + \varphi_{s_d^s}^x)} f_{\mp}(s; s, s_d) \right\} \quad , \quad (5.31) \end{aligned}$$

from measurements in the vertical plane. In order to simplify the expression, some extra

definitions were introduced:

$$\lambda_c = \frac{\sin[\pi(Q_x - Q_y)]}{\sin[\pi(Q_x + Q_y)]},$$

$$f_{\mp}(s_j; s_a, s_b) = \frac{\sum_{w \in I(s_a, s_b)} h_{w, \mp} e^{i[\varphi_{w_j}^x \mp \varphi_{w_j}^y]}}{1 - e^{2\pi i[Q_x \mp Q_y]}}, \quad (5.32)$$

where the interval $I(s_a, s_b)$ contains all elements between s_a and s_b ,

$$I(s_a, s_b) = \{w : s_a < s_w < s_b\}, \quad (5.33)$$

and for $h_{w, \mp}$ the same convention applies as for f_{\mp} . Measurements can only be performed on the real signal. The complex signal needed for the calculation of RDTs has to be reconstructed. This reconstruction mixes the RDTs f_+ and f_- , given by the following equation. Under the assumption that adjacent BPMs are used for the reconstruction, the combined f terms read

$$f_{\mp, x, y} = \frac{1}{\sqrt{1 - \lambda_y^2}} \left\{ e^{\pm i[\varphi_{s_d^x}^{d,x} - \varphi_{s_d^x}^x]} f_{\mp, x} - \lambda_y e^{\pm i[\varphi_{s_d^y}^{d,y} - \varphi_{s_d^y}^y]} f_{\pm, x} \right\}. \quad (5.34)$$

It is important to take into account this fact when finally reconstructing the driven f terms from the measured ones.

5.2 Comparison of the methods for typical LHC machine configurations

In this section the effect of the driven motion on the measured RDTs is studied using an LHC optics with no other perturbations than the additional coupling sources and no higher order multipoles active, in order to avoid feed down polluting the results. From Eq. (5.26) one can see that the effect of the AC-dipole jump is proportional to the strength of the RDTs at the position of the AC-dipole. This means, given a weak initial coupling around the AC-dipole or a sufficient correction of the local coupling, the effect is expected to be low and further coupling measurements are not impacted by it.

Given that the effect is only a minor one in the first place, repeated measurement and correction of coupling will iteratively improve the precision of the coupling measurement. In Figure 5.2 the case of a coupling bump in the lattice is shown. The AC-dipole is located at $s = 9846$ m in a region with low coupling.

The right plot shows no effect of the AC-dipole. The formula method and the new method

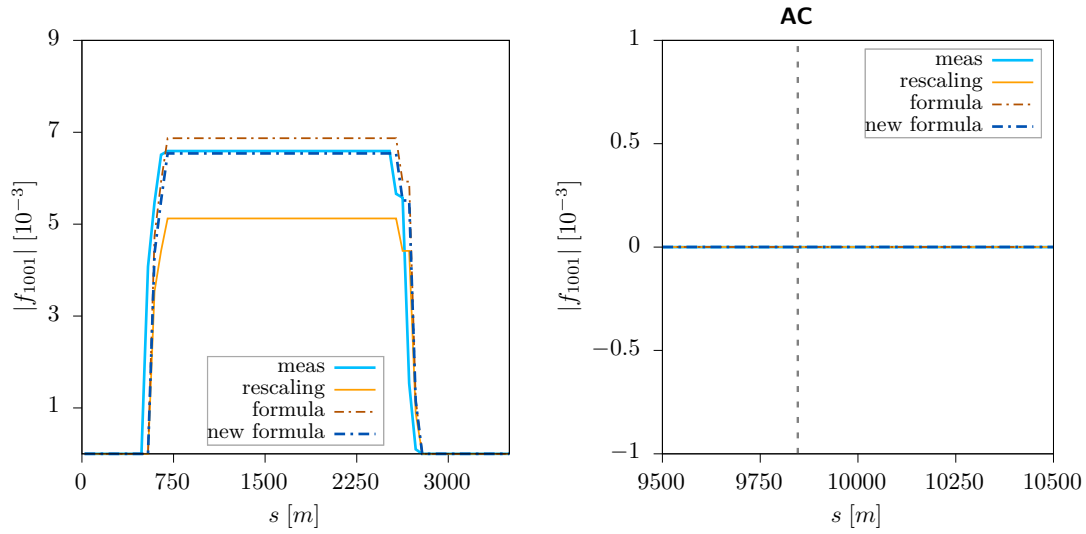


Figure 5.2: Comparison of the three methods with a coupling bump in the lattice. The absolute value of coupling term f_{1001} is shown. The formula method and new method (called *new formula*) manage to reproduce well the f_{1001} . The naive rescaling method underestimates the f term in the bump. The offset between *meas* and the reconstructed values is due to the reconstruction of the complex signal. The right plot shows the region in which the AC-dipole is located. There is no jump at the location of the AC-dipole.

show a good agreement with the measured values. The rescaling method underestimates the f term inside the bump but outside its accuracy is also excellent. All three methods correctly predict zero coupling outside of the closed bump. The measured values show an offset which is due to the reconstruction of the complex signal from the momentum Eq. (2.114) which picks up coupling sources from in between s_a and s_b .

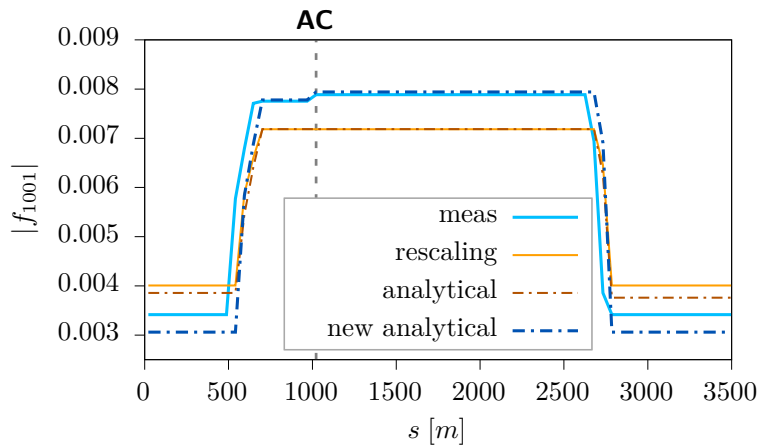


Figure 5.3: Comparison of the three methods with the AC-dipole surrounded by a coupling bump. The AC-dipole is creating a jump in the coupling term f_{1001} at its location. Only the new formula is able to reproduce this jump. The position of the AC-dipole is marked by a vertical line.

Figure 5.3 now shows the picture when the AC-dipole is placed *inside* the bump and, thus, being in a region with strong coupling. In this case a visible bump is expected and the

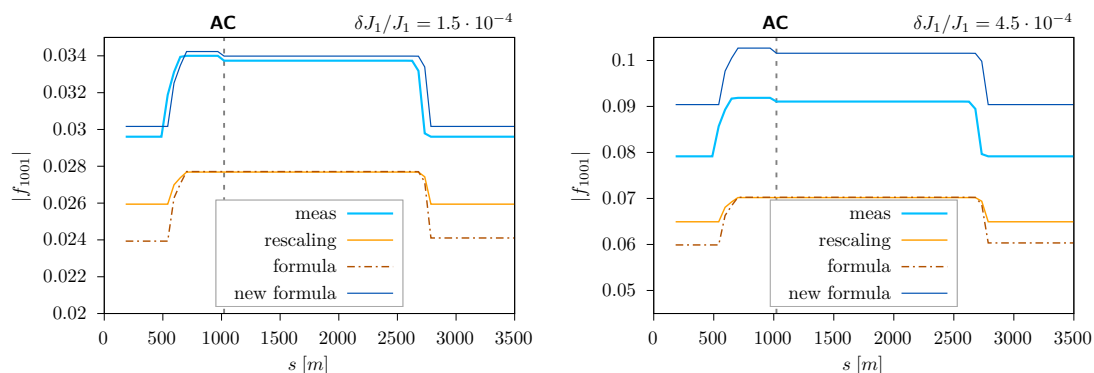


Figure 5.4: These plots show the same comparison as Fig. 5.3 but for the HL-LHC lattice at $\beta^* = 15$ cm with varying strengths of the skew quadrupoles which form the coupling bump. A degradation of the performance of the new formula is observed.

agreement with the conventional methods should decrease because they do not consider the additional source. Indeed, the new formula yields overall a better accuracy, especially inside of the coupling bump. The jump at the position of the AC-dipole is well reproduced, as expected from Eq. (5.26).

5.2.1 HL-LHC and stronger coupling

The HL-LHC has more challenging optics and a similar coupling source as for the LHC simulations in the previous section creates considerably larger coupling.

Figure 5.4 shows slightly stronger coupling in the HL-LHC lattice at $\beta^* = 15$ cm. Two coupling strengths are tested. For reference, the initial setting for the first magnet in the bump is printed in the top right corner of each plot¹. The left plot shows the same initial strength as for the LHC simulations in the previous section. The matching of the closed coupling branch failed which resulted in non-zero coupling outside of the designated region.

Although still better than the conventional methods, the new formula does not achieve the same performance as before and starts to lose its performance w.r.t. the other methods.

5.3 Conclusion

Current methods to calculate the coupling terms f_{1001} and f_{1010} in the LHC have been revised and brought into context of recent findings. The AC-dipole creates a jump in the RDTs at its location and this jump can be demonstrated for the coupling RDTs in simulations. A study of sextupolar RDTs is presented in [58]. The calculation of a corrected coupling RDT has been performed and its accuracy in the case of small coupling has been

¹The final value depends on the matching but is still of the same order of magnitude.

demonstrated in simulations.

CONCLUSION AND OUTLOOK

The development and enhancement of three distinct optics measurement methods have been presented in this work. These developments improve the precision and accuracy of optics measurements and extend our understanding of the imperfections in an accelerator.

The first method, called the *Analytical N-BPM method* is a more precise and faster measurement of the β function. It is based on the method previously developed and used for LHC measurements during run 1, called the N-BPM method, that combines measurements from a set of N neighbouring BPMs to remove statistical uncertainties. Systematic uncertainties were taken into account through computationally expensive Monte-Carlo simulations. The N-BPM method required a careful preparation for each individual optics setting before the actual measurement. The analytical N-BPM method performs error propagation purely from analytic calculations and can therefore be applied during the measurement without the need of precomputing the covariance matrix. It also avoids the complications from failing simulations, which can happen for extreme optics settings, like low β^* optics for example. A filtering of BPM combinations with unsuitable phase advances was also introduced in this method, which makes it even more independent from the exact optics. The analytical N-BPM method is now routinely used in various optics measurement and machine development studies of various of CERN's main accelerators, including the LHC. It has also been used in collaborative efforts in accelerators from several external institutes like SuperKEKB and PETRA III.

The second method is a new local observable for linear lattice imperfections. Although such observables already exist for non-linear imperfections, in the linear case there was none. This work presents a local observable for the linear imperfections for the first time. This locality holds up to first order in the quadrupole error δK_1 . The phase advance beating, which depends on all errors in the lattice, can be rearranged in a way that eliminates global

contributions, yielding two kinds of local observables: if the unperturbed phase advance is a multiple of π , the phase advance beating is directly a local observable, in the general case a combination of four nearby phase measurements has to be used to construct a local term. The existence of this observable has been shown in this work. Strong error sources can be detected using the local observable, which can be used to guide local error corrections. Such a usage is planned for the upcoming run 3 of the LHC.

The last method describes the impact of forced particle motion on the measurement of transverse coupling. The AC-dipole, which is used to create the forced motion for measurements, creates a jump in the amplitude of the coupling RDTs. This jump does not appear in any of the current methods to calculate forced coupling and correct for the forced motion. In this work, forced coupling RDTs are calculated using a new framework that has recently been developed and which accounts for this jump. The agreement for small coupling is excellent. A future usage to compensate for the driven motion using an iterative approach is conceivable.

The introduction of next generation light sources and the design and construction of new colliders and future projects create the demand for more advanced or novel measurement and correction methods. More challenging optics designs require more precise measurements and large lattices call for efficient algorithms and according implementation. This work presents developments in the domain of linear optics measurements for circular accelerators, improving existing methods and introducing new ones in order to prepare for future operation of the LHC and other accelerators.

BIBLIOGRAPHY

- [1] R. Tomás, M. Aiba, A. Franchi, and U. Iriso, *Review of linear optics measurement and correction for charged particle accelerators*, Phys. Rev. Accel. Beams, **20**, 5, p. 054801, (2017) [↗](#) .
- [2] R. Tomás, T. Bach, R. Calaga, A. Langner, Y. I. Levinsen, E. H. MacLean, T. H. Persson, P. K. Skowronski, M. Strzelczyk, G. Vanbavinckhove, and R. Miyamoto, *Record low β beating in the LHC*, Physical Review Special Topics - Accelerators and Beams, **15**, 9, (2012) [↗](#) .
- [3] T. Persson, F. Carlier, J. C. De Portugal, A. G. T. Valdivieso, A. Langner, E. H. Maclean, L. Malina, P. Skowronski, B. Salvant, R. Tomás, and A. C. Bonilla, *LHC optics commissioning: A journey towards 1% optics control*, Physical Review Accelerators and Beams, **20**, 6, pp. 1–9, (2017) [↗](#) .
- [4] M. Aiba, M. Böge, J. Chrin, N. Milas, T. Schilcher, and A. Streun, *Comparison of linear optics measurement and correction methods at the Swiss Light Source*, Phys. Rev. ST Accel. Beams, **16**, p. 012802, Jan 2013 [↗](#) .
- [5] D. Sagan, R. Meller, R. Littauer, and D. Rubin, *Betatron phase and coupling measurements at the Cornell Electron/Positron Storage Ring*, Phys. Rev. ST Accel. Beams, **3**, p. 092801, Sep 2000 [↗](#) .
- [6] J. Borer, A. Hofmann, J. Koutchouk, T. Risselada, and B. Zotter, *Measurements of Betatron Phase Advance and Beta Function in the ISR*, IEEE Transactions on Nuclear Science, **30**, pp. 2406–2408, Aug 1983 [↗](#) .
- [7] A. Langner, G. Benedetti, M. Carlà, J. M. Coello de Portugal, U. Iriso, Z. Martí, and R. Tomás, *Optics Measurement using the N-BPM Method for the ALBA Synchrotron*, in *Proceedings, 6th International Particle Accelerator Conference (IPAC 2015): Richmond*,

- Virginia, USA, May 3-8, 2015, p. MOPJE057, (2015). [↗](#) .
- [8] W. Herr and B. Muratori, *Concept of luminosity*, (2006) [↗](#) .
- [9] ATLAS Collaboration, *Observation of a new particle in the search for the Standard Model Higgs boson with the ATLAS detector at the LHC*, Physics Letters B, **716**, 1, pp. 1 – 29, (2012) [↗](#) .
- [10] CMS Collaboration, *Observation of a new boson at a mass of 125 GeV with the CMS experiment at the LHC*, Physics Letters B, **716**, 1, pp. 30 – 61, (2012) [↗](#) .
- [11] K. Schindl, *The injector chain for the LHC*, in *9th LEP Performance Workshop*, pp. 47–52, 3 1999. [↗](#) .
- [12] E. Mobs, *The CERN accelerator complex - 2019. Complexe des accélérateurs du CERN - 2019*, Jul 2019 [↗](#) . General Photo.
- [13] K. Hanke *et al.*, *The LHC Injectors Upgrade (LIU) Project at CERN: Proton Injector Chain*, in *8th International Particle Accelerator Conference*, p. WEPVA036, (2017). [↗](#) .
- [14] H. Bartosik *et al.*, *The LHC Injectors Upgrade (LIU) Project at CERN: Ion Injector Chain*, in *8th International Particle Accelerator Conference*, p. TUPVA020, (2017). [↗](#) .
- [15] S. Peggs and T. C., *Nonlinear diagnostics using an AC Dipole*, Tech. Rep. RHIC/AP/159, BNL, (1998). [↗](#) .
- [16] R. Miyamoto, S. E. Kopp, A. Jansson, and M. J. Syphers, *Parametrization of the driven betatron oscillation*, Phys. Rev. ST Accel. Beams, **11**, p. 084002, Aug 2008 [↗](#) .
- [17] R. Miyamoto, *Measurement of Coupling Resonance Driving Terms with the AC Dipole*, tech. rep., BNL, (2010). [↗](#) .
- [18] R. Tomás, *Adiabaticity of the ramping process of an ac dipole*, Phys. Rev. ST Accel. Beams, **8**, p. 024401, (2005) [↗](#) .
- [19] J.-P. Koutchouk, *Measurement of the beam position in the LHC main rings*, tech. rep., CERN, Geneva, (2002). [↗](#) .
- [20] R. Tomás, *BPM noise in different accelerators*, June 2021. [↗](#) .
- [21] L. Malina and R. Tomás, *BPMs in turn-by-turn mode: LHC experience and HL-LHC requirements*, September 2019. [↗](#) .
- [22] CERN, *CAS - CERN Accelerator School: Intermediate Accelerator Physics: Zeuthen, Germany 15 - 26 Sep 2003. CAS - CERN Accelerator School: Intermediate Course on Accelerator Physics*, (Geneva), CERN, (2006). [↗](#) .
- [23] H. Wiedemann, *Particle Accelerator Physics*. Graduate Texts in Physics, Berlin, Ger-

- many: Springer (2015).
- [24] A. Wolski, *Beam Dynamics in High Energy Particle Accelerators*. IMPERIAL COLLEGE PRESS (2014).
- [25] E. Courant and H. Snyder, *Theory of the alternating gradient synchrotron*, *Annals Phys.*, **3**, pp. 1–48, (1958) [↗](#) .
- [26] A. Bazzani, E. Todesco, G. Turchetti, and G. Servizi, *A normal form approach to the theory of nonlinear betatronic motion*, (1994). [↗](#) .
- [27] H. Georgi, *LIE ALGEBRAS IN PARTICLE PHYSICS. FROM ISOSPIN TO UNIFIED THEORIES*, **vol.** 54 (1982).
- [28] W. Herr and E. Forest, *Non-linear Dynamics in Accelerators*, pp. 51–104, (2020) [↗](#) .
- [29] L. Landau, E. Lifshitz, J. Sykes, and J. Bell, *Mechanics: Volume 1*. Butterworth-Heinemann, Elsevier Science (1976).
- [30] R. Bartolini and F. Schmidt, *Normal Form via Tracking or Beam Data*, *Part. Accel.*, **59**, pp. 93–106. 10 p, (1997) [↗](#) .
- [31] R. Tomas, M. Bai, R. Calaga, W. Fischer, A. Franchi, and G. Rumolo, *Measurement of global and local resonance terms*, *Phys. Rev. ST Accel. Beams*, **8**, p. 024001, (2005) [↗](#) .
- [32] W. Herr, ed., *CAS - CERN Accelerator School: Advanced Accelerator Physics: Trondheim, Norway 18 - 29 Aug 2013. CAS - CERN Accelerator School: Advanced Accelerator Physics Course*, (Geneva), CERN, CERN, Jan 2016. Organisers: Dr. Roger Bailey (Head of CAS); Barbara Strasser (CAS Assistant), [↗](#) .
- [33] A. Franchi, L. Farvacque, F. Ewald, G. Le Bec, and K. B. Scheidt, *First simultaneous measurement of sextupolar and octupolar resonance driving terms in a circular accelerator from turn-by-turn beam position monitor data*, *Phys. Rev. ST Accel. Beams*, **17**, 7, p. 074001, (2014) [↗](#) .
- [34] A. Franchi, *Error analysis of linear optics measurements via turn-by-turn beam position data in circular accelerators*, (2016) [↗](#) .
- [35] A. Franchi, R. Tomás, and F. Schmidt, *Magnet strength measurement in circular accelerators from beam position monitor data*, *Phys. Rev. ST Accel. Beams*, **10**, p. 074001, (2007) [↗](#) .
- [36] L. D. Landau, *On the vibrations of the electronic plasma*, *J. Phys. (USSR)*, **10**, pp. 25–34, (1946) [↗](#) .
- [37] J. Rees and A. Chao, *Landau Damping Revisited*, 12 2008 .
- [38] P. Castro, *Luminosity and beta function measurement at the electron-positron collider*

- ring LEP. PhD thesis, (1996). Presented on 25 Nov 1996, [↗](#) .
- [39] A. Wegscheider, A. Langner, R. Tomás, and A. Franchi, *Analytical N beam position monitor method*, Phys. Rev. Accel. Beams, **20**, p. 111002, Nov 2017 [↗](#) .
- [40] A. Langner and R. Tomás, *Optics measurement algorithms and error analysis for the proton energy frontier*, Phys. Rev. ST Accel. Beams, **18**, 3, p. 031002, (2015) [↗](#) .
- [41] A. S. Langner, *A Novel Method and Error Analysis for Beam Optics Measurements and Corrections at the Large Hadron Collider*. PhD thesis, Feb 2017. Presented 2017, [↗](#) .
- [42] T. Kariya and H. Kurata, *Generalized Least Squares*. Wiley Series in Probability and Statistics, Wiley (2004).
- [43] <http://mad.web.cern.ch/mad>. .
- [44] P. Hagen, M. Giovannozzi, J. P. Koutchouk, T. Risselada, S. Sanfilippo, E. Todesco, and E. Wildner, *WISE: An adaptative simulation of the LHC optics*, Conf. Proc., **C060626**, pp. 2248–2250, (2006) [↗](#) .
- [45] P. Hagen, M. Giovannozzi, J. P. Koutchouk, T. Risselada, F. Schmidt, E. Todesco, and E. Y. Wildner, *WISE: a Simulation of the LHC Optics Including Magnet Geometrical Data*, Conf. Proc., **C0806233**, p. TUPP091, (2008) [↗](#) .
- [46] F. Schmidt, E. Forest, and E. McIntosh, *Introduction to the polymorphic tracking code: Fibre bundles, polymorphic Taylor types and "Exact tracking"*, Tech. Rep. CERN-SL-2002-044-AP. KEK-REPORT-2002-3, CERN, Geneva, Jul 2002. [↗](#) .
- [47] A. Langner, G. Benedetti, M. Carlà, U. Iriso, Z. Martí, J. C. de Portugal, and R. Tomás, *Utilizing the N beam position monitor method for turn-by-turn optics measurements*, Phys. Rev. Accel. Beams, **19**, 9, p. 092803, (2016) [↗](#) .
- [48] S. Fartoukh, *Achromatic telescopic squeezing scheme and application to the LHC and its luminosity upgrade*, Phys. Rev. ST Accel. Beams, **16**, 11, p. 111002, (2013) [↗](#) .
- [49] S. Fartoukh, R. Bruce, F. Carlier, J. Coello De Portugal, A. Garcia-Tabares, E. Maclean, L. Malina, A. Mereghetti, D. Mirarchi, T. Persson, M. Pojer, L. Ponce, S. Redaelli, B. Salvachua, P. Skowronski, M. Solfaroli, R. Tomas, D. Valuch, A. Wegscheider, and J. Wenninger, *Experimental Validation of the Achromatic Telescopic Squeezing Scheme at the LHC*, [↗](#) .
- [50] A. Wegscheider and R. Tomás, *Local observable for linear lattice imperfections in circular accelerators*, Phys. Rev. Accel. Beams, **23**, p. 054002, May 2020 [↗](#) .
- [51] J. Coello de Portugal, R. Tomás, and M. Hofer, *New local optics measurements and correction techniques for the LHC and its luminosity upgrade*, Phys. Rev. Accel. Beams, **23**, p. 041001, Apr 2020 [↗](#) .

- [52] A. Franchi and R. Tomás, *Computation of the Coupling Resonance Driving term f_{1001} and the coupling coefficient C from turn-by-turn single-BPM data*, (2010) [↗](#) .
- [53] R. Calaga, R. Tomás, and F. Zimmermann, *BPM Calibration Independent LHC Optics Correction*, Conf. Proc., **C070625**, p. 3693, (2007) [↗](#) .
- [54] W. Guo, S. L. Kramer, F. Willeke, X. Yang, and L. Yu, *A Lattice Correction Approach through Betatron Phase Advance*, in *Proceedings, 7th International Particle Accelerator Conference (IPAC 2016): Busan, Korea, May 8-13, 2016*, p. MOOCB02, (2016). [↗](#) .
- [55] T. Zhang, X. Huang, and T. Maxwell, *Linear optics correction for linacs and free electron lasers*, Phys. Rev. Accel. Beams, **21**, p. 092801, Sep 2018 [↗](#) .
- [56] R. Calaga and R. Tomás, *Statistical analysis of RHIC beam position monitors performance*, Phys. Rev. ST Accel. Beams, **7**, p. 042801, (2004) [↗](#) .
- [57] M. Gasior, J. Olexa, and R. J. Steinhagen, *A High-resolution Diode-Based Orbit Measurement System - Prototype Results from the LHC*, Conf. Proc., **C11-05-16.4**, p. MOPD24. 3 p, May 2011 [↗](#) .
- [58] F. S. Carlier, *A Nonlinear Future - Measurements and corrections of nonlinear beam dynamics using forced transverse oscillations*. PhD thesis, (2020). Presented 08 May 2020, [↗](#) .
- [59] R. Tomás, *Normal form of particle motion under the influence of an AC dipole*, Phys. Rev. ST Accel. Beams, **5**, p. 054001, (2002) [↗](#) .